Earth-Science Reviews 224 (2022) 103885

Contents lists available at ScienceDirect

Earth-Science Reviews

journal homepage: www.elsevier.com/locate/earscirev

A review of methods used to test periodicity of natural processes with a special focus on harmonic periodicities found in global U—Pb detrital zircon age distributions

Stephen J. Puetz [a,*], Kent C. Condie [b]

[a] Progressive Science Institute, Honolulu, HI 96814, USA
[b] New Mexico Institute of Mining and Technology, Socorro, NM, 87801, USA

ARTICLE INFO

Keywords:
Periodicity
Causality
Zircon
Periodogram
Correlogram
U-Pb analysis

ABSTRACT

The multitude of periodicities reported from detrital zircon and related geochemical time-series leads to questions about which cycles should be considered valid, which are byproducts of random noise, and the degree of uncertainty associated with the detected periodicities. To enhance understanding of detrital zircon periodicities, we review existing estimates by assessing both methodological reliability and reproducibility of results. Methods commonly employed include scalograms from wavelet analysis, periodograms from spectral analysis, and correlograms from cross-correlation analysis. This study analyzes possible zircon periodicities ranging from less than 1 million to 1 billion years. We systematically evaluate the capabilities of each approach, and then refine estimates in terms of their reproducibility using seven completely independent to partially independent U—Pb detrital zircon databases. Periodicities that are consistently found at high confidence levels are considered statistically significant, whereas those that cannot be replicated are considered as spurious. The comparative studies of detrital zircon ages reveal a dominant set of eight period-tripling cycles of ~0.373, 1.12, 3.35, 10.1, 30.2, 90.5, 272, and 815 myr (rounded to three digits). Additionally, a multitude of subordinate cycles are harmonically linked to the main period-tripling sequence. The detected periodicities often correspond to cycles found in large igneous province occurrence, seafloor spreading rates, million-year climatic cycles, mass extinctions, and other natural variation seemingly unrelated to geological processes. The commonality suggests a persistent episodic link between zircon production and other geological and non-geological processes throughout Earth's entire history. As a final step, we review a variety of hypotheses being explored to explain primary, secondary, and tertiary causes of cycles, and then propose tests that should soon be possible to either validate or falsify these diverse ideas.

1. Introduction

Repeated studies of U—Pb age distributions from preserved detrital zircon show obvious episodes. The research community widely acknowledges the episodes but still debate their cause. Some interpret zircon age peaks as episodes of enhanced crustal production (Stein and Hofmann, 1994; Condie, 1998; Arndt and Davaille, 2013; Parman, 2015; Rollinson, 2017; Walzer and Hendel, 2017; Condie et al., 2018), whereas others hypothesize that collisional phases of the supercontinent cycle cause variation in crustal preservation potential which in turn produces artificial episodes recorded in detrital zircon histograms (Hawkesworth et al., 2009; Dhuime et al., 2011; Cawood et al., 2013). Recent research (Puetz and Condie, 2021) discusses problems related to testing these hypotheses. Here, rather than definitively identifying a cause, we consider a wide variety of hypothesis and treat them with tolerant skepticism (Lakatos, 1970, 1978). A primary goal is to use deductive reasoning to define the implications for each of the competing hypotheses, and devise tests aimed to disprove the falsifiable hypothesis (Popper, 1963; Puetz and Condie, 2021). Another key goal is to rigorously define the multitude of periodicities detected from global detrital zircon time-series. This is critical because a detailed understanding of how Earth has evolved should generally precede an attempt to explain its causality.

An extensive review of research related to periodicity in geologic,

* Corresponding author.
E-mail address: puetz.steve@gmail.com (S.J. Puetz).

https://doi.org/10.1016/j.earscirev.2021.103885
Received 10 August 2021; Received in revised form 30 November 2021; Accepted 30 November 2021
Available online 4 December 2021

climatic, and related processes highlight a key problem confronting both episodic crustal production proponents and selective preservation hypothesis supporters. These studies show a multitude of cycles ranging from as short as a few thousand years to more than a billion years, which of course, includes many periodicities that have no apparent link to supercontinent amalgamation. Generally working from the longest reported periodicities to the shortest, subsequent paragraphs summarize a small subset of the voluminous history of reported cycles.

Mitchell et al. (2019) analyzed an eHf(t) time-series developed by Roberts and Spencer (2014) and postulate a harmonic hierarchy of mantle and lithospheric convective cycles. They refer to the periodicities as a 1200-myr super-ocean cycle, a 600-myr supercontinent cycle, a 200–350 myr Wilson cycle, a 150–250-myr whole mantle cycle, a 60–80 myr upper mantle cycle, a 20-myr magmatic cycle, and a 6-myr magmatic cycle. This range comes close to spanning the entire gamut from 300-kyr to 999-myr investigated here.

Periodicities in the 800–820 myr range are found in mafic and ultramafic rock production (Isley and Abbott, 2002), the supercontinent cycle (Korenaga, 2006), a detrended detrital zircon time-series (Puetz et al., 2018), and an $^{87}Sr/^{86}Sr$ time-series (Prokoph and Puetz, 2015). An analysis of eHf(t) data (Lancaster et al., 2011) indicates 600 myr periodicity between the formation of new crust and its reworking in later magmatic events, essentially the same as the 600-myr supercontinent cycle of Mitchell et al. (2019).

Chen and Cheng (2018) use spectral analysis with singularity sequences for both U—Pb detrital zircon ages and a $\delta^{18}O$ time-series and found consistent harmonic (1/f) scaling, with dominant periodicities of ~210, 420, and 760-myr. Rolf et al. (2014) mentions a 640-myr supercontinent cycle – essentially the same as the missing 630-myr harmonic in the Chen and Cheng (2018) sequence. Ratcheting down a scale, harmonic depositional cycles of 180-myr and transgressions and regressions with periods of 90-myr are found in the sedimentary cover of the West Siberian Plate (Belozerov and Ivanov, 2003).

Mitchell et al. (2019) refers to a 275 ± 75-myr Wilson cycle, which is nearly identical to the 273-myr cycle found in the detrital zircon age-distribution (Puetz et al., 2017; Puetz et al., 2018; Puetz and Condie, 2019), the 273-myr periodicity in mafic rock production (Isley and Abbott, 2002), and the 250–300-myr periodicity in Phanerozoic sea-level (Boulila et al., 2018).

Periodicities of 130–150, 60–70, 28–35-myr are found in marine genera abundance, $^{87}Sr/^{86}Sr$ time-series, and large igneous province formations (Prokoph et al., 2013), while the detrital zircon age distribution exhibits similar 135–140-myr periodicity (Puetz and Condie, 2019). Archean crustal production in the Pilbara Craton exhibits a cycle of ~100-myr (Wiemer et al., 2018), whereas the detrital zircon age-distribution shows periodicity of 91–94 myr (Condie et al., 2018; Puetz et al., 2018; Puetz and Condie, 2019). Boulila et al. (2018) also found a 91-myr cycle in Phanerozoic sea-level flux as well as periodicities of 9.3 and 36-myr.

The types of data analyzed for cyclicity go well beyond the preceding summaries. For instance, during the Phanerozoic, North American sedimentation rates show a cycle of 56-myr (Meyers and Peters, 2011). As another example, a study of periodicity in geomagnetic reversal rates since 570 Ma indicates cycles of ~285, 114, 71–64, 47 and 34–32 myr (Negi and Tiwari, 1983), and Rampino and Caldeira (2020) report a 32-myr cycle in sea level variation.

Tiwari and Rao (1998) report correlated 30-myr cycles in asteroid impacts, global CO_2 variation, biological mass extinctions, mantle convection variation, geomagnetic reversals, volcanism, and geotectonic processes. They hypothesize these seemingly divergent processes are intricately linked. The ~30-myr cycle has been recognized for several decades in geological events (Holmes, 1927; Grabau, 1940) and climatic variation (Dorman, 1968). Just below the 30-myr threshold, Müller and Dutkiewicz (2018) found a 26-myr cycle in oceanic crustal carbon, while Rampino and Caldeira (2015) report a 25.8-myr cycle in asteroid impacts and a 27-myr cycle in marine extinction events since 260 *Ma*, and Rampino et al. (2021) found cycles of 27.5 and ~ 9–10-myr from a time-series of 89 major geological events.

Moving down the spectrum, Ikeda et al. (2020) found a 10-myr monsoon cycle during the Mesozoic. The power spectrum from an early Mesozoic $\delta^{13}C$ time-series show periodicities of 2, 3.5, 10, and 30-myr exceeding 90% confidence (Ikeda and Tada, 2020). Lake level variation and biogenic silica burial flux exhibit cycles of 2.2-myr at 227 *Ma*, which transform to 1.1 to 1.4-myr from 225 to 218 *Ma*, and then to 1.8-myr and 3.5-myr cycles from 219 to 205 *Ma* (Ikeda and Tada, 2020).

As already noted, several investigators suggest that geological and/or climatic cycles are both correlated and harmonic (Belozerov and Ivanov, 2003; Puetz et al., 2014; Prokoph and Puetz, 2015; Boulila et al., 2018; Chen and Cheng, 2018; Mitchell et al., 2019; Puetz and Condie, 2019). This summary just touches on the reported cycles, which can become so overwhelming that it might easily lead to confusion and complete distrust of spectral analysis results and assessments of periodicity in general. At a minimum, the divergent range of cycles leads to questions such as: How reliable are the reported periodicities? Can geological, biological, and climatic processes really fluctuate in a multitude of cycles ranging from 1-myr to 1-gyr? How can one confidently determine if the cycles are harmonic, as some claim? And if the divergent processes exhibit correlated periodicities, how can one assess if the cycles are real or spurious? And if real, how can one determine the cause(s)?

We initially address these questions by focusing on problems related to accurately estimating periodicity in U—Pb detrital zircon age distributions, and then treat detailed analyses of potential causes of the cycles as a secondary goal. Because of infinite regress (Popper, 1963), it is logically impossible to definitively prove a cause. Nonetheless, even though causality can never be proven, theoretical predictions from the associated empirical formulation can be falsified (Popper, 1963). Correlations are often used when postulating cause; however, proper application of correlations is seldom straightforward. When two time-series A and B are correlated, one of five possibilities explain the correlation: (i) A and B are spuriously correlated by coincidence, (ii) A causes B, (iii) B causes A, (iv) an unidentified factor C causes both A and B, or (v) A causes B and B causes A. Even though some consider this final possibility as valid, most considered this as circular reasoning, and thus invalid and dismissed. A 95% confidence band generally eliminates correlation by coincidence. However, a 95% confidence level will be erroneous 1 in 20 times! Whether A causes B, or B causes A can something be obvious (especially if a lead/lag relationship is firmly established). In some instances, a logical cause-effect relationship will remain elusive, which means any one of A, B, and unknown-C remain viable as potential causes. Even when an A → B or B → A causal relationship might currently seem obvious, it is always possible that when an unidentified process C is finally discovered, process C will explain the A-B correlation far better than an A → B or B → A hypothesis alone.

A few examples of hypotheses developed to explain volcanic-climatic correlations underscore the complexity of determining cause from correlations. Precambrian researchers have postulated cause and effect relationships among: (a) mantle plume activity, continental magma production at convergent margins, and crustal deformation (Condie and Puetz, 2019); (b) magmatic episodes developing from rapid subduction, which cools the mantle, followed by pulses of mantle heating that accompany magmatic events (Johnson and Van Kranendonk, 2019); and (c) magmatic episodes as a consequence of conductive heating of lower crust directly preceded mantle exhumation and crustal excision, suggesting that thermal weakening of the lithosphere promotes focusing of extensional strain (Smye et al., 2019). Nance (2021) suggests climate is affected, postulating that the supercontinent cycle controls Earth's long-term climatic variation. Additionally, Edmond (1992) and Fang et al. (2019) postulate that chemical weathering of uplifted rock modulates atmospheric carbon dioxide levels, which in turn contributes to global climate cycles.

While still a minority view, as well as being based on a sparse set of

terrestrial asteroid impact samples, Rampino (2015) postulates the passage of Earth through dense clumps of dark matter in the Galactic plane causes episodic heating in Earth's core, which might explain a correlated 30-myr periodicity observed in terrestrial geologic activity. In a slightly different twist, Tiwari and Rao (1998) propose a chain reaction of episodic asteroid impacts, global CO_2 variation, biological mass extinctions, mantle convection variation, geomagnetic reversals, volcanism, and geotectonic processes.

Based on a 1-myr time-series of cyclic sequences from Pacific Rim tephra layers and an apparent correlation with $\delta^{18}O$ variation, Kutterolf et al. (2013) suspect a causal link between variations in ice age climate, continental stress field, and volcanism. They propose that redistribution of water/ice concentrations associated with ice-ages causes crustal stress fractures that lead to variable volcanism. However, a recent study by Sternai et al. (2020) casts some doubt on this interpretation because climate variation from 60 to 50 *Ma* was unusually erratic without evidence of polar ice caps. In summary, divergent and often contradictory ideas are hypothesized to explain correlations among magmatic activity, global climate variation, and other related processes – a common problem with many if not most hypotheses of cause-and-effect relationships.

This review of divergent ideas about episodic natural processes and their causes motivated us to advance future studies of periodic processes from multiple perspectives. Accordingly, the remainder of this study investigates analyses of periodic processes from the perspectives of: (a) the capability of spectral analysis to accurately estimate periodicities; (b) considerations for achieving a globally representative time-series when the goal is to estimate global variation over time; (c) the accuracy and reliability of data; (d) testing if reported cycles are harmonic; (e) testing if a cycle has persisted throughout Earth's existence or if the cycle developed well after Earth formed; (f) validating cycles based on reproducibility of results; (g) reviewing existing correlations among natural processes; (h) attempting to falsify conjectures with data completely independent from a hypothesis; and (i) designing tests capable of rigorously testing the variety of hypothesis aimed at explaining terrestrial magmatic episodes. That is, we attempt to devise tests to legitimately disprove each hypothesis, including those that we consider to be viable, those considered by the majority as accepted viewpoints, and minority hypotheses generally not considered as viable possibilities.

As explained in the remainder of this work, if the primary geological cycles are found to be harmonic, then it suggests either a single common cause or a small number of causes exist. This contrasts with the prevailing view that each cycle has an independent cause. Thus, if the geological/climatic cycles are indeed harmonic, then it should greatly simplify the ongoing search for causes.

2. Data

All time-series in this study are available from previously published sources. We enhanced two detrital zircon databases (Voice et al., 2011; Roberts and Spencer, 2014) by adding the country from which the samples were taken, and then simulating sample locations by random assignments of GPS coordinates within a box surrounding the sampled country. Two other detrital zircon databases are also analyzed (Puetz and Condie, 2019; Puetz et al., 2021) which already include GPS coordinates. Additionally, the databases of Puetz and Condie (2019) and Puetz et al. (2021) are combined to construct are more complete global database with nearly one million records. Then we segregate the combined database into two depositional subsets, one for records with depositional ages $\leq$200 *Ma* and another for depositional ages >200 *Ma*. We subsequently refer to these seven databases as Voice-DB, Roberts-DB, Puetz-2019-dB, Puetz-2021-dB, Combined-DB, Dep-Modern-DB, Dep-200 *Ma*-DB.

The primary analyses are limited to time-series constructed from these seven databases consisting of ages from analyses of detrital zircon cores. After analyzing each time-series with periodograms and correlograms, we then construct six empirical models from the detected periodicities and their phases. Each model is designed to simulate periodicity within specific frequency bands. We then use the models for further analyses, which compare cyclical variation from the detrital zircon models with variation in ages of igneous zircon cores (Puetz and Condie, 2019); plate velocities (Condie et al., 2021); variation in ages of zircon rims (Puetz and Condie, 2019; Puetz et al., 2021); periods of glaciation (Geboy et al., 2013; Young, 2018; Alvarenga et al., 2019; Chen et al., 2019); variation in $\delta^{18}O$ and $\delta^{13}C$ time-series (Zachos et al., 2001).

3. Methods

For the seven detrital zircon databases in this study, we use standard time-series methods (Priestley, 1988; Percival and Walden, 1993; Scheel and Scholtes, 2000; Chatfield, 2004; Stoica and Moses, 2005; Box et al., 2016) and apply bandpass filters to transform the sequences into stationary time-series (Scheel and Scholtes, 2000; Box et al., 2016). Then, spectral analysis is performed using REDFIT software version 3.5 (Schulz and Mudelsee, 2002), and cyclicity is further analyzed by cross-correlating (Box et al., 2016) the seven time-series. The analyses exclude scalograms from wavelet analysis, which is a commonly used method for evaluating the persistence of a given cycle. This is because scalograms generally require subjective interpretations and do not produce hard numbers like periodograms.

When interpreting the scalogram's color coded heat map, analysts sometimes tilt a periodogram 90° and place it next to the scalogram to illustrate periodicity. Others use periodograms to find the period of a cycle and then manually draw a horizontal line on the scalogram to depict it (which is not derived from the scalogram). The main advantage of a scalogram is its color-coded portrayal of spectral density as a function of time. However, as shown in Section 4.1, segmented correlograms can also reveal spectral power persistence as well as measuring spectral power consistency. Thus, for the present studies, we find no advantage for using continuous wavelet analysis.

Three examples illustrate shortcomings with Wavelet analyses (Fig. 1) by using from the 'wt' function in the biwavelet package of R with detrital zircon age distributions binned at 30-myr intervals from 4350 to 0 *Ma*. The 'wt' scalogram from the Voice-DB time-series (Fig. 1a) uses the default white noise setting (Fig. 2, white), with the horizontal line manually drawn from the corresponding periodogram. However, the upward sloping red noise model (Fig. 2, red) and pink noise model (Fig. 2, pink) are generally considered to be appropriate for geological time-series, and Schulz and Mudelsee (2002) have implemented a red noise model into their REDFIT spectral analysis software. Thus, for geological time-series, the 'wt' function should be configured to the red-noise option. This is done for the scalogram from the Roberts-DB time-series (Fig. 1b). This simple setting transforms much of the blue in the 256–512-myr range (Fig. 1a) to red (Fig. 1b). The 'wt' scalogram also contains an option 95% confidence bands with the red-noise option (Fig. 1c). Still, none of these configurable options produce hard numbers about periodicity. Furthermore, the three scalograms (Figs. 1a-1c) given misleading information about the persistence of two cycles with periodicities of ~815-myr and ~ 272-myr. The last two scalograms (Fig. 1b, c) show several deep-red blotches near 272-myr, and a single large blotch near 815-myr. However, neither scalogram indicates these cycles are persistent. This distinctly contrasts with cross correlation analyses (Section 4.1) which demonstrate both cycles have persisted at least since 4 *Ga*. Equally important, neither scalogram identifies the periodicities as 272 and 815-myr. As shown in Section 4.2, a combination of correlograms and periodograms are required to constrain the periodicities.

Previously, our research focused on dominant low frequency detrital zircon cycles, generally with periods greater than 90-myr. The approach here differs because we assess zircon-age periodicity for the entire spectrum from 300-kyr to 1-gyr and include both highly and marginally

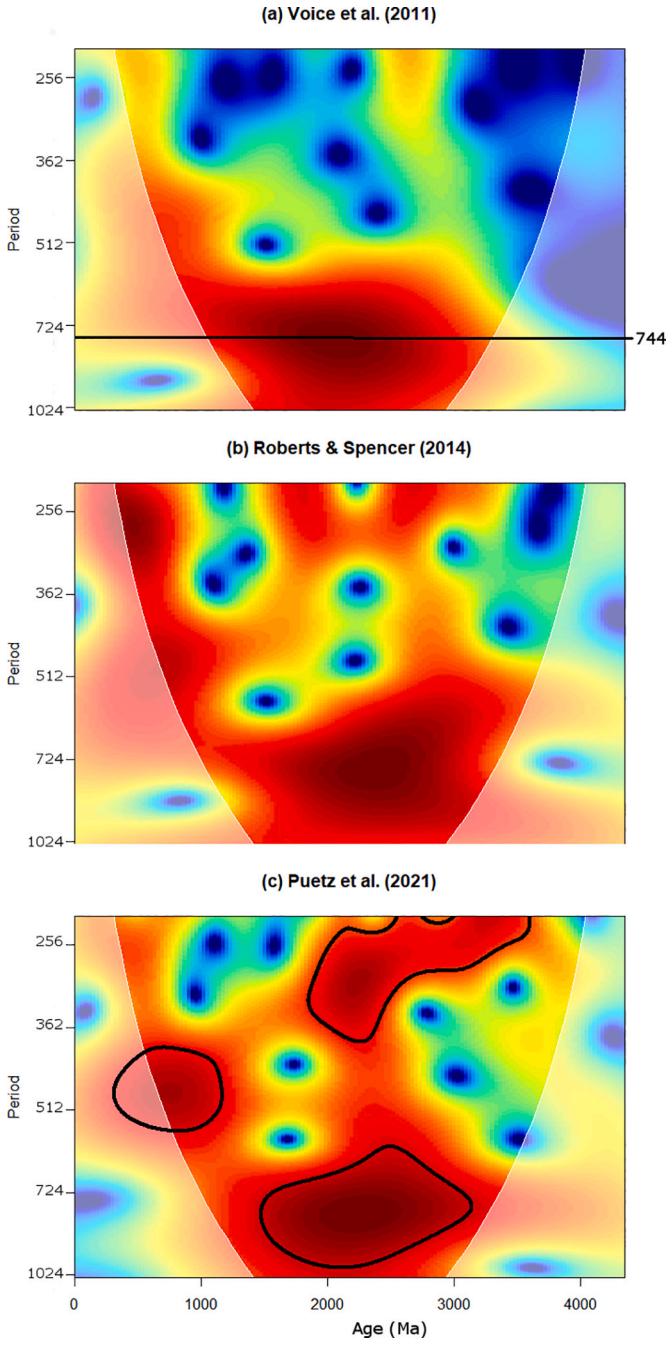

Fig. 1. Wavelet analysis. Scalograms from continuous wavelet transforms using the 'wt' function in the biwavelet package of R. Scalograms are derived from bandpass filtered time-series spanning 4350–0 *Ma*, binned at 30-myr intervals for: (a) Voice-DB using the default white noise option, (b) Roberts-DB using the red noise option, and (c) Puetz-2021-dB using the options for red noise with 95% confidence bands. (For interpretation of the references to color in this figure legend, the reader is referred to the web version of this article.)

significant periodicities. Then we assess reproducibility of results by testing if bandpass filtered time-series from the seven detrital zircon databases produce the same cycles. Rigorous assessments of reproducibility require scrutiny of at least 11 statistical properties, some of which are often overlooked, misinterpreted, or misapplied when evaluating the periodicity of geological processes. Accordingly, the remainder of this section reviews and discusses 11 critical statistical considerations: (a) repeated analyses of different datasets completely independent from each other and completely independent from of the model, (b)

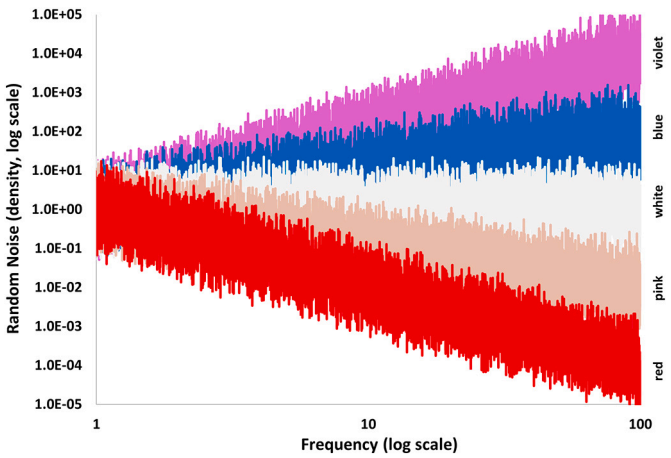

Fig. 2. Colors of noise. In signal processing, five colors designate the primary types of noise, which vary proportionally to frequency (f). From top to bottom, the types of noise are violet ($\propto f^2$); blue ($\propto f$); white ($\propto$constant); pink ($\propto 1/f$); and red ($\propto 1/f^2$). (For interpretation of the references to color in this figure legend, the reader is referred to the web version of this article.)

weighting non-random samples collected by convenience so they simulate random samples, (c) requiring global sampling when a property is globally heterogeneous, (d) weighting sedimentary rock samples for depositional age bias, (e) requiring an adequate number of samples per time-series bin, (f) avoiding outliers potentially produced by endpoint bias, (g) analyzing a high-quality time-series with sufficient cyclic repetitions, (h) using 3-point interpolation to increase the accuracy spectral analysis peaks by one digit, (i) deciding when and how to smooth a periodogram, (j) determining the best age from U—Pb detrital zircon analyses, and (k) deciding when to reject discordant U—Pb analyses.

3.1. Independent data

The vast array of cycles being reported can lead to confusion and distrust of models purporting periodicity. Aber (1997) addresses the general distrust of modeling projects and modeling papers, which he attributes to authors generally not being held accountable to a consistent, rigorous set of standards of full disclosure during peer-review. A key step to overcoming skepticism is achievable with increased understanding of the difference between "calibration" and "validation" (Aber, 1997). As it relates to this research, calibration involves analyzing detrital zircon time-series to determine the model parameters (Section 5), which consist of cyclic-periods and age-maxima found from periodograms and correlograms. A basic tenet of hypothesis testing is that predictions from a model can only be validated after repeated successful tests of the model with independent data. That is, the data for any test must not be used in any way to derive parameters in the model or vice versa (Aber, 1997; McDowall, 2004; Waters and Craw, 2006; Crisp et al., 2011). This means that if a model is "calibrated" from values in one database, then a completely different database must be assembled to test and "validate" the model. Climatic researchers sometimes violate this basic tenet of testing, with a specific example discussed in Section 3.5.

When assessing reproducibility of results, the period of a cycle is more likely to be real if it can be reproduced within a small ± error when measured from a time-series completely independent from a model. Here, we generally consider a cycle is validated if its periodicity falls within ±1% of a model. In this way, repeated validations with independent data boost the likelihood of a cycle being real.

To develop the models, coherent periodicities and phases are found from the seven time-series constructed from the aforementioned databases. Ideally, the records from the seven databases should also be completely independent, which is not entirely the case. The Voice-DB,

Roberts-DB, and Puetz-2019-dB are each completely independent from Puetz-2021-dB, Dep-Modern-DB, and Dep-200 *Ma*-DB. Also, Dep-Modern-DB is completely independent from Dep-200 *Ma*-DB. The largest database, Combined-DB, is approximately 65% independent from Puetz-2019-dB but only 35% independent from Puetz-2021-dB. The Puetz-2019-dB is roughly 95% independent from the Voice-DB and about 85% independent from the Roberts-DB.

It is desirable, but not required, to have independent datasets to calibrate a model. The fact that some of the detrital zircon databases are not completely independent from the others reduces the effectiveness of the tests, but not drastically so. The average independence is close enough to 100% to provide a relatively diverse set of tests to assess reproducibility. However, after the model is "calibrated" this way, then 100% independence is indeed a strict requirement for subsequent testing. This means that a completely new detrital zircon database will be required to test and validate the models presented in Section 5.

3.2. Sampling considerations

Another basic tenet of hypothesis testing is random selection of samples. Non-random sampling introduces a bias that can result in incorrect interpretations. Examples of non-random sampling include sampling based on judgement or samples selected for their convenience. For example, a detrital zircon sample is random when all global locations have an equal chance of being selected. That is, selection of any zircon always happens by chance, rather than by choice. Random samples are more likely to be representative of the entire global population, which enhances confidence in subsequent statistical inferences.

A key obstacle in assessing global geological/climatic properties, such as detrital zircon ages, is that investigators seldom, if ever, use a random number generator to select sample sites. Instead, investigators typically select a location to augment understanding of a specific geological region, which is a form of convenience sampling. Then zircons are gathered in a "cluster" from the sampled rock. Cluster sampling often increases the uncertainty of estimates made from geological populations (Lo and Watson, 1998). Nonetheless, cluster sampling is economically efficient, and thus preferred, because it significantly reduces travel time as well as sampling time. For this reason, true random sampling of geological processes is impractical and will likely never be achieved. However, it is possible to simulate random sampling by weighting cluster samples collected by convenience. By weighting samples proportionally to pre-defined surface areas from which the samples were gathered, convenience sampling and cluster sampling become appropriate for making geological estimates (Stehman and

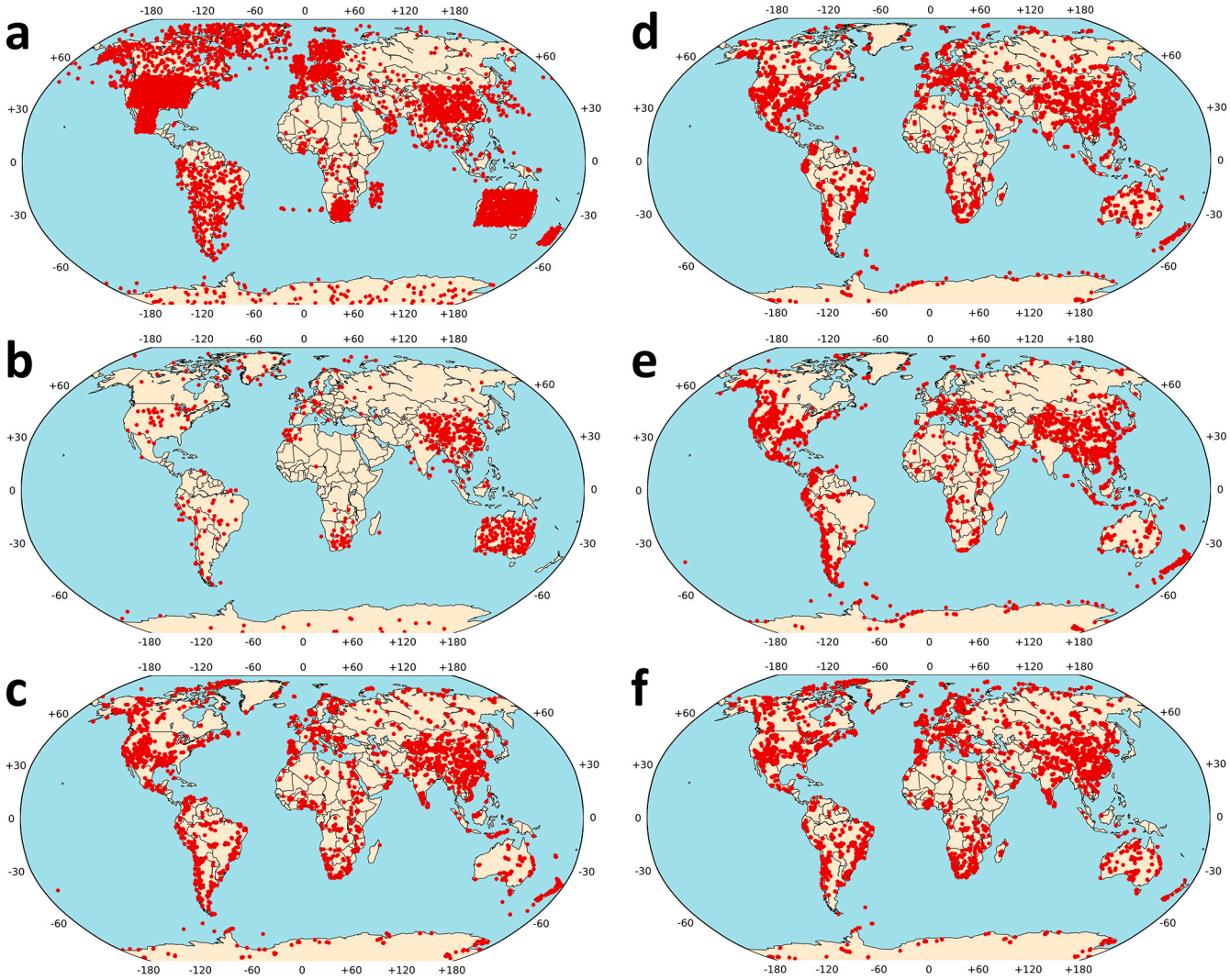

Fig. 3. U—Pb detrital zircon sample locations. Panels: (a) Voice-DB with randomly generated locations based on sampled country; (b) Roberts-DB with randomly generated locations based on sampled country; (c) Puetz-2019-dB records with single grain concordia ages; d) Puetz-2021-dB; (e) Dep-Modern-DB; and (f) Dep-200 *Ma*-DB.

Selkowitz, 2010; Puetz et al., 2017; Puetz and Condie, 2020). Maps of sampling densities for six of the detrital zircon databases (Fig. 3) illustrate the disproportionate sampling typically found is "global" databases.

Because the enhanced Voice-DB and Roberts-DB contain country names but not GPS coordinates, the records are weighted proportionally to country surface areas. Conversely, the records in the remaining databases are weighted proportionally to surface areas of grids roughly equivalent to 12° latitude x 12° longitude equatorial grids. After applying regional weighting, the detrital zircon age-distributions from the seven databases simulate time-series developed from random samples.

3.3. Accuracy and precision of ages

After weighting the records to simulate random sampling, the next objective is to develop time-series in the form of U—Pb age distributions. When doing so, it is helpful to understand the accuracy of individual age-maxima and minima in the time-series. It might be tempting to equate the uncertainty of an age-peak with the uncertainty of a single zircon grain, which is not the case. Published uncertainties quantify the precision of U—Pb zircon ages (Schoene et al., 2013). The true ages will remain unknown, but they are assumed to be accurate if isotope decay rates are estimated correctly. Gathering a large set of random-like samples can accurately pinpoint age-peaks because, at a given age, the standard deviation of the uncertainties of individual grains (precision errors) will produce a normal distribution around the "true" age. This rationale is generally used when estimating the age of an igneous rock. In these instances, the stated ± error of the rock's age is significantly smaller than individual U—Pb zircon uncertainties (Georgiev et al., 2016; Lopez et al., 2018). We use the same rationale to assess uncertainties associated with individual age-peaks in U—Pb detrital zircon age distributions.

The zircon ages from the Voice-DB and Roberts-DB likely employ age-cutoffs to select either a $^{206}Pb/^{238}U$ age or a $^{207}Pb/^{206}Pb$ as the "best age" – a practice still commonly used today. However, we filter records from the other five databases to only include non-iterative ages for concordance classes 1 through 5 (Puetz et al., 2021). Some investigators (Zimmermann et al., 2018; Vermeesch, 2020) recommend single grain concordia ages, whereas Puetz et al. (2021) demonstrating that non-iterative ages produce nearly identical age distributions for time-series segregated by concordance classes 1 through 5. Conversely, all arbitrary age-cutoff methods produce divergent age distributions for concordance classes 1 through 5. Because of strong correlations among class 1–5 non-iterative age-distributions (Puetz et al., 2021), rejecting records with concordance classes >5 does not contribute to a filtering bias (Gehrels et al., 2019). Thus, we are reasonable sure the five time-series constructed from non-iterative ages produce highly accurate unbiased estimates of the global U—Pb detrital zircon age distribution. But how accurate?

The red curves (Fig. 4) illustrate 3σ Gaussian bell curves, which include 99.7% of all random samples with a standard deviation of σ. Each Gaussian curve is calculated at 250-myr increments by using the mean precision error of individual zircon grains (Fig. 4, green curve). At a given age, the sharpness of a red curve (Fig. 4) corresponds to the expected distribution of a set of zircon samples with the same age – if the number of records per bin are sufficiently large. Thus, the relatively small Roberts-DB (less than 50,000 records) often fails to meet the "records per bin" criterion, whereas bins from the Combined-DB (with nearly a million records) normally satisfy this threshold.

Because the number of records per bin increase as the age decreases and because the precision errors progressively decrease for ages below ~1600 *Ma*, a Phanerozoic zircon age distribution (541–0 *Ma*) might contain sufficiently sharp age-peaks to detect ultra-high frequency periodicities as small as 1-myr. Of course, this is far from certain. We defer further discussions on the limits for detecting high frequency variation until explaining the entire methodology and after conducting the entire set of tests. The basic approach employs six sets of bandpass filtered time-series from each of the seven databases (Section 3.9). Table 1 summarizes the systematic approach for analyzing periodicities based on sampling frequency, time-ranges, and bin sizes for the seven studies. Except for study 7, each test is designed to evaluate periodicities in a range from ~4 to 16 times the Nyquist limit (twice the bin size or bandwidth). Each study (Table 1) terminates at a different time in the past to minimize endpoint bias, which sometimes occurs from difficulty in measuring properties at the beginning and end of a time-series. Endpoint bias is generally observed from extreme outliers at the endpoints of a bandpass filtered time-series. The bias is generally found when bins have few or no samples. Especially for the high frequency tests, the oldest age is set to relatively young ages so the sample-count per bin is sufficiently large and extreme outliers are minimized. Section S4 of Supplement S1 discusses the choice of a 4350–0 *Ma* age range for the

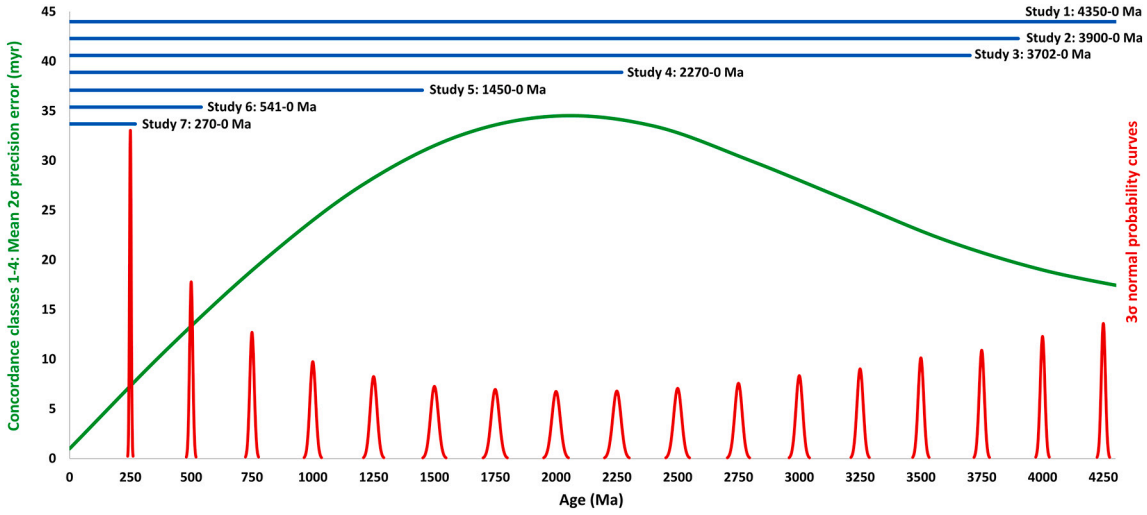

Fig. 4. Accuracy of U—Pb zircon age-peaks, as a function of time. Green curve: mean 2σ uncertainty (precision errors) from the records in Puetz-2021-dB for concordance classes 1 through 4; red curves: normal 3σ Gaussian distributions (99.7% band) at 250-myr increments, derived from the standard deviations in the green curve; and blue lines: range of time-series being analyzed. Study 1 (spanning 4350–00 *Ma*) includes periodicities of ultra-low frequencies where accurate ages are less critical, whereas study 7 (spanning 270–0 *Ma*) includes periodicities of ultra-high frequencies where accurate ages are of utmost importance. (For interpretation of the references to color in this figure legend, the reader is referred to the web version of this article.)

Table 1
Properties of time-series analyzed in this study.

Study No.	Frequency description	Periodicity range (myr)	Nyquist limit (myr)	Age range (*Ma*)	Bin size (myr)	No. of databases tested
1	Ultra-low	1000–225	60	4350–0	30	7
2	Low	333–75	20	3900–0	10	7
3	Medium-low	110–25	6	3702–0	3	5
4	Medium-high	37–8	2	2270–0	1	5
5	High	12.5–2.7	0.6	1450–0	0.3	4
6	Ultra-high	4.2–0.9	0.2	541–0	0.1	4
7	Ultra-high	1.4–0.3	0.2	270–0	0.1	4

low-frequency test, including a discussion of possible bias from Western Australia samples between 4350 *Ma* and 3900 *Ma*. From this analysis, we conclude that Western Australian samples do not unduly bias the global age distribution for the 4350–3900 *Ma* interval.

3.4. Evaluating periodicities and correlations

Just as the ages of igneous rocks and peaks in U—Pb age distributions both have greater precision than the single-grain U—Pb ages from which they are estimated, the periodicity of a cycle is typically more accurate than the uncertainties of individual peaks in the time-series. For a set of periodic peaks with a ± 1σ error, the number of cyclic repetitions primarily controls the error-curve (Hinnov, 2005; Puetz and Condie, 2019) which has a hyperbolic shape. Thus, as cyclic repetitions increase, the estimated periodicity becomes increasingly accurate (Fig. 5a).

Similarly, constructing a time-series with sufficiently large sampling points (*n*) can minimize the probability of detecting a false signal when correlating a time-series with a sinusoidal model. For a time-series with *n* sampling points, Eq. (1) defines a one-tailed correlation band ($\rho_{1\text{-}\alpha}$), which is a function of the inverse T-distribution ($T_{inv,\alpha}$) with *n*-1 degrees of freedom (*df*), where α is the *p*-value which designates the probability of a false signal.

$$\rho_\alpha = \left(\frac{T_{inv,\alpha}}{\left(T_{inv,\alpha}\right)^2 + df} \right) \tag{1}$$

The inverse T-distribution ($T_{inv,\alpha}$) is easily calculated with the T.INV function (Microsoft Excel T.INV, 2021) or the tinv function (MATLAB,

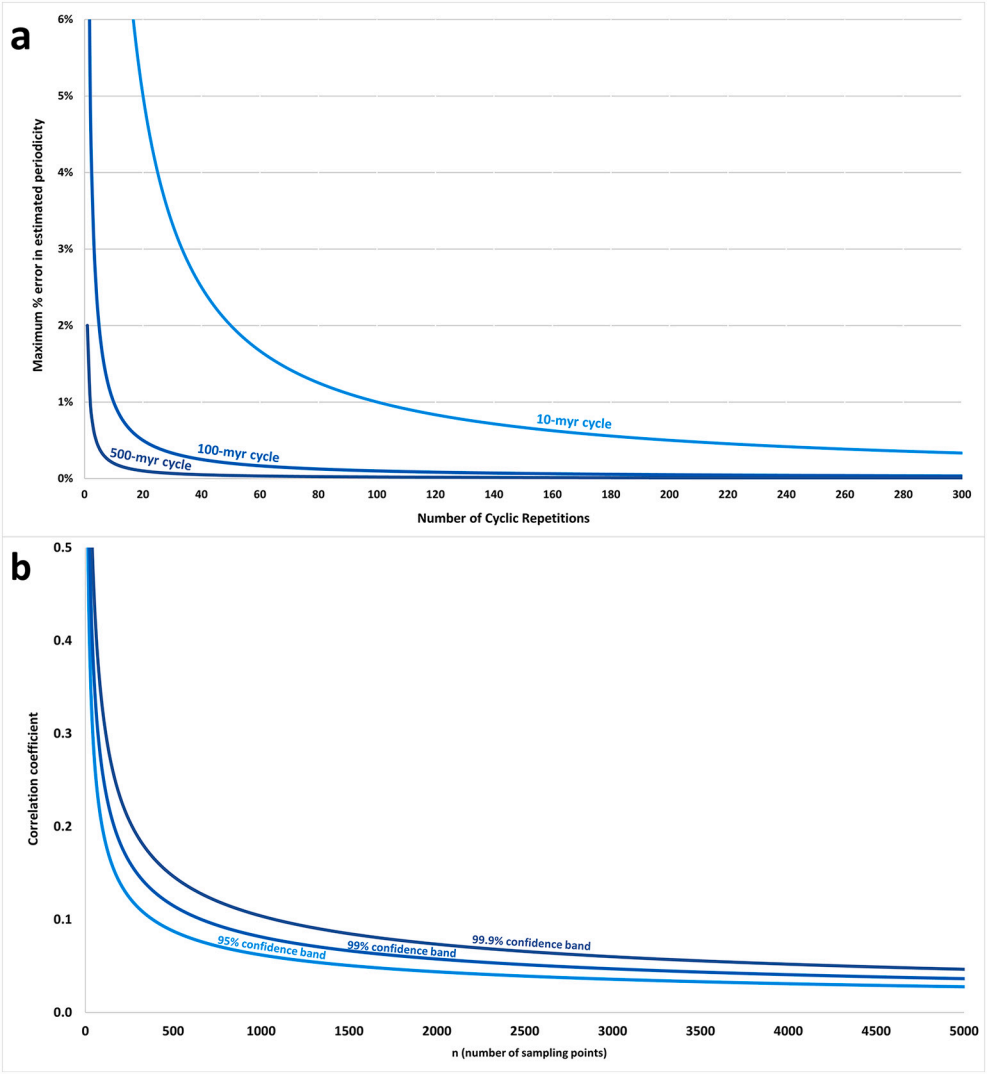

Fig. 5. Reliability of periodicities and correlations as a function of sampling duration. Panels: (a) For a time-series with age-peaks having a ± 1σ accuracy, the maximum error for the estimated periodicity (%, vertical axis) is a function of the period, *p*, and the cyclic repetitions, *r* (horizontal axis), given by the function $2\sigma/rp$; for U—Pb zircon age-peaks with 5-myr uncertainty, the hyperbolic curves define expected uncertainties for cycles with periods of 10, 100, and 500-myr. (b) 95% (light blue), 99% (medium blue), and 99.9% (dark blue) confidence bands (Eq. (1)) for evaluating the correlation between a time-series and a sinusoidal mode using *n* sampling points. (For interpretation of the references to color in this figure legend, the reader is referred to the web version of this article.)

2021). After setting α to 0.05, 0.01, and 0.001, the corresponding 95%, 99%, and 99.9% confidence bands are calculated as a function of n (Fig. 5b) for 1-tailed tests. The bands illustrate the correlations that are required for a time-series to be statistically significant at 95%, 99%, and 99.9% confidence levels with a sinusoidal model, where the time-series and the model have n sampling points. The correlation is determined to be statistically significant when it exceeds the specified confidence band.

Alternatively, the correlation confidence bands (Fig. 5b) can be determined from randomly generated sequences via Monte Carlo simulations (Metropolis et al., 1953). Jorgensen (2000) adds to this by discussing problems related to adequate sample size for Monte Carlo simulations. Furthermore, Mudelsee (2003) discusses Monte Carlo scenarios for using time-series with either $n > 200$ or $n > 500$ for achieving acceptable accuracy in geoscience studies.

Regardless of the approach, increasing the duration of a time-series has at least two analytical benefits. First, it generally gives a more accurate estimate of periodicity. Second, it minimizes the probability of time-series A producing a spurious correlation with either a sinusoidal model or time-series B.

3.5. Spectral analysis capabilities

When studying a time-series via spectral analysis, a keen understanding of spectral analysis capabilities benefits interpretations. Specifically, it is beneficial to use spectral analysis to its fullest practical limits without exceeding its capabilities, and then reporting results to the same precision as its capabilities. Many Earth scientists seem to believe that spectral analysis is incapable of producing reliable estimates beyond 1 or 2-digit precision. For this reason, a type of reporting bias occurs when periodogram results are rounded to a number ending in 0 or 5, such as 130, 135, or 140-myr rather than 128, 136, or 142. In a slightly different twist, sentences are sometimes worded to suggest that when spectral analysis reveal cycles of 30, 32, and 34-myr that these periodicities can be treated as the same cycle – even though the 2-myr separation equates to a 6.25% difference. If age-peaks are reasonably reliable and cyclic repetitions exceed ~20, then spectral analysis is capable of estimating periodicity to within 1% of the true periodicity (Fig. 5a). Given these capabilities, the differences among 30, 32, and 34-myr indicate that either (a) each time-series contains a different cycle, or (b) some of the time-series are significantly flawed and unrepresentative of the true processes.

Awareness of spectral analysis capabilities will certainly enhance realistic interpretations. As one example, Boulila et al. (2018) found an ~250-myr cycle from a Phanerozoic sea-level time-series. However, the Phanerozoic only contains two repetitions of this cycle, and spectral analysis is incapable of reliable estimates from a time-series with so few repetitions. Thus, one should be highly skeptical of this 250-myr estimate. Another example also demonstrates misunderstandings of spectral analysis capabilities as well as possible biased reporting of a detected cycle. Kutterolf et al. (2008, 2013) compiled a 1.2-myr time-series of Circum-Pacific (Ring of Fire) volcanism in the form of well-preserved tephra layers. Ash layers were dated by correlating them with tephra layers dated from on-land tephra. The ages for undated ash layers were estimated from their relative position between known "tie points" using linear interpolation (Kutterolf et al., 2008). This dating procedure is common, and in fact, the preferred unbiased method when sedimentation rates are unknown. Extending their earlier work, Kutterolf et al. (2013) identified 408 tephra layers at sites along the Ring of Fire and estimated the tephra ages have uncertainties ranging up to 14%. Even though sedimentary tie points are radiometrically dated, layers between tie points cannot be radiometrically dated and thus have large uncertainties. Their spectral analysis results indicate periodicity in Ring of Fire volcanism of 44-kyr, whereas our analysis of their data using a bandpass filter shows 45.3-kyr periodicity. For a time-series with 27 cyclic repetitions spanning 1.2-myr, the 1.3-kyr difference between our results is large enough to wonder if they found a 44.9-kyr cycle or perhaps a 44.4-kyr cycle and truncated the decimal portion of the result – a type of reporting bias.

Yet, the 1.3-kyr difference in results is relatively minor when compared to their subsequent time-series adjustments. Kutterolf et al. (2013) then assumed that no process other than Earth's obliquity is expected to concentrate spectral power around the 44-kyr frequency band, and thus consider their results as a statistically significant detection of tephra layer variation caused by the 41-kyr obliquity cycle in climatic variation. They attempt to justify this claim by stating the tephra layers have uncertainties ranging up to 14% of their age, and they subsequently revised the ages by "compressing" all tephra ages by 10%. By altering the ages this way, the reassigned ages are 10% younger than their original estimates. Next, they published the power spectrum showing 41-kyr periodicity from the revised ages, rather than publishing the spectrum with 44-kyr periodicity from the unbiased time-series.

This example (Kutterolf et al., 2013) highlights a serious problem that should never happen, as well as three common problems with interpreting spectral analysis results: (a) changing the ages of isotopically dated tie points to conform with a particular hypothesis should never happen because radiometric dates have far greater accuracy than ages from assumed sedimentation rates; (b) incorrectly equating uncertainties in the ages of individual peaks with uncertainties in periodicity (Section 3.4); (c) revising ages to conform to a hypothesis should never happen because it violates the basic tenet of hypothesis testing of complete independence between the data and the model being tested (Section 3.1); and (d) a general distrust in spectral analysis capabilities by incorrectly assuming that a 7.3% difference between a spectral peak (44-kyr) and a hypothesis (41-kyr) constitutes a legitimate validation of the hypothesis.

Our general guideline is quite restrictive. A 2% difference might be considered as a validation for a time-series with 5 to 20 cyclic repetitions, whereas the allowable difference shrinks to 1% for a time-series with reliable age-peaks and more than 20 cyclic repetitions. The justification for these tight validation restrictions rests on numerous tests of synthesized sinusoidal time-series constructed from Eq. (2), where a_t is the amplitude of the signal at time, t, Φ is the phase of a cyclic maximum, and p is the period of the cycle.

$$a_t = 1 + cos\left(\frac{2\pi(t-\Phi)}{p}\right) \tag{2}$$

Section S1 of Supplement S1 contains two sets of sinusoidal time-series, with the additive compilation of 2 sinusoids and 15 sinusoids. These synthetic time-series are used in a series of tests with progressively large random noise added to them. Then we perform spectral analysis to determine which cycles are detected and their accuracy. This type of test has a huge advantage because one knows beforehand the true periodicities (the periods, p, in Eq. (2) used to construct the sinusoids). Thus, one knows beforehand what the results should be.

To achieve the highest degree of accuracy and precision, we estimate all spectral peaks using standard 3-point interpolation. This can increase the accuracy of spectral-peak estimates by up to one digit. Standard 3-point interpolation (Eq. (3)) optimizes estimates of spectral peaks, where f is the interpolated estimate, f_i is the frequency of a spectral peak s_i is the corresponding spectral power, f_{i-1} and f_{i+1} are the frequencies adjacent to f_i, and s_{i-1} and s_{i+1} are the spectral powers adjacent to s_i.

$$f = f_i + \left(\frac{f_{i+1} - f_i}{2}\right)\left(\frac{s_{i+1} - s_{i-1}}{2s_i - s_{i+1} - s_{i-1}}\right) \tag{3}$$

Because we know the answers beforehand, comparisons of results with input periods provide objective assessments of maximum capabilities of spectral analysis. These tests are conducted for perfectly measured sinusoids (no noise) and for sinusoids with disguised signals (progressive additions of noise). Section S1 of Supplement S1 provides extensive details of these tests, which are briefly summarized here. For a

sinusoidal time-series with multiple cycles, spectral analysis enhanced with 3-point interpolation can accurately estimate periodicity to 4-digits for cycles with more than 10 repetitions, whereas the accuracy shrinks to 3-digits or lower for cycles with fewer than 5 repetitions. If two low frequency cycles have similar periods and few repetitions, spectral analysis might merge them into single cycle rather than showing them separately. After adding noise to simulate measurement errors associated with imperfect time-series, spectral analysis will generally still produce estimates that are accurate to 3-digits, which we consider to be the maximum capability of spectral analysis when applied to a geological time-series with reliable data and greater than 10 to 20 cyclic repetitions.

3.6. Global representativeness

When comparing one global time-series with another, we want to be reasonably sure that both time-series are reliable global proxies (rather than incomplete regional proxies). This is especially relevant to geological time-series which are generally understood be heterogeneously distributed throughout the globe (Cawood et al., 2013; Puetz et al., 2017). When assessing global representativeness, factors to consider include bin-size, number of records per bin, and the heterogeneity of the property being measured. Zircon age-distributions are quite heterogenous, whereas $\delta^{18}O$ values are likely to be more globally homogenous (but still variable) for a given age. If so, then to attain global representativeness, fewer $\delta^{18}O$ records would be required per bin than for detrital zircon records.

Because estimates of periodicity are optimized when reliable data extends into the distal past (Section 3.4), we naturally seek extended time-series. Of course, reliable is the key. Typically, a trade-off exists between finding reliable data further into the past and extending cyclic repetitions. Defining the point at which unreliability supplants repetitions is often subjective. When attempting to estimate global age distributions, as here, the number of records per bin often provides an indirect measure of reliability. For instance, when estimating global $\delta^{18}O$ variation at 1-myr intervals, will a 1-myr bin with a single $\delta^{18}O$ sample provide a reliable global estimate for that interval? Probably not. Because the properties of a climatic time-series (which might be more homogeneous globally) differ from a detrital zircon time-series (being more heterogenous globally), considerable knowledge of a particular time-series property is a requisite to assessing its reliability as a global proxy. If such a determination is definitive, then the point for terminating a time-series becomes known, and spectral analysis can be performed with increased confidence. Whether the time-series is of the highest quality or of inferior quality, spectral analysis will always return an answer with its relevance equivalent to its reliability. Thus, with a diligent assessment of time-series quality prior to spectral analysis, it is possible to attain 3-digit accuracy when estimating periodicity with sufficient cyclic repetitions of high-quality data.

3.7. Periodogram smoothing window

The variety of spectral analysis methods is extensive and not discussed in detail here. The divergent approaches might lead to some hesitancy about which method to use or if one method has a distinct advantage over the others. Our overall assessment is that the specific periodogram choice is trivial when compared to the factors of utmost importance – numerous cyclical repetitions and globally representative data. Sometimes excessive attention is given to complex approaches for estimating periodicity and confidence bands, while minimal attention is given to the more critical factors of cyclic repetitions and data quality. We have changed our views on one key aspect of spectral analysis, the smoothing parameter, which is now kept to a minimum in the studies here. Most spectral analysis programs either eliminate or minimize unsightly sidelobes (Scargle, 1982) via an array of smoothing options. We use REDFIT software (Schulz and Mudelsee, 2002), which employs a Lomb–Scargle Fourier transform using a first-order autoregressive (AR1) process to estimate red-noise confidence bands (Fig. 2, red). REDFIT provides five methods for suppressing sidelobes: (a) rectangular, (b) Welch, (c) Hanning, (d) triangular, (e) Blackman-Harris. REDFIT also includes an n50 parameter for smoothing the power spectrum. In the past, we smoothed rather aggressively, which allowed us to focus on the dominant periodicities. However, we now change this approach and smoothing minimally to study all possible periodicities – including weak signals that could be either real cycles or a byproduct of random noise. Lengthy time-series do require some smoothing. To estimate the degree of smoothing when using Welch's method, we initially set n50 to the value given by Eq. (4), where the REDFIT smoothing parameter is an integer, n_{50}, and n is the number of sampling points (bins) in an evenly spaced time-series.

$$n_{50} = \frac{\sqrt{n}}{30} - 3 \tag{4}$$

This equation returns a real number, which must then be rounder to an integer. When the equation returns a number < 1, n50 is set to 1. However, for studies 6 and 7, we found the smoothing was insufficient at n50 = 10 and reset n50 to 15. Table 2 summarizes the studies in terms of bin size, number of sample points (bins), and n50 settings.

A Lomb-Scargle periodogram provides a means for estimating periodicity for an unevenly sampled time-series (Scargle, 1982). However, we still bin records at evenly spaced intervals because binning provides advantages that simplify subsequent tests. The advantages include assessing appropriate sampling densities as a function of time (records per bin), convenient cross-correlation tests, and bandpass filtering to transform the time-series into stationary sequences (Scheel and Scholtes, 2000).

Section S1 of Supplement S1 illustrates and discusses 15 periodograms from the Roberts-DB time-series by setting n50 to 1, 2, and 3 for each of the five methods for suppressing sidelobes (Fig. S6). The illustration (Fig. S6) gives visual insights into how smoothing affects the power spectrum. The supplement also illustrates how bandpass filtering a time-series with evenly spaced intervals provides a means for assessing stationarity (a flattened time-series with similar variation throughout the time-series). The inherent difficulty in measuring the beginning and end of a time-series can produce a disproportionally large number of outliers, referred to as endpoint bias (Hardy and Jamieson, 2017; Puetz and Condie, 2019). Bandpass filtering allows us to evaluate stationarity and the locations of outliers, and thus determine an appropriate age-range for minimizing endpoint bias for each time-series.

In summary, the periodogram method is relatively unimportant, but it is best to minimize smoothing the power spectrum if the goal is to better understand all possible periodicities, including dominant cycles as well as weaker cycles. We use Welch's method in REDFIT and primarily focus on problems related to representative global sampling, stationary time-series, and high-quality data with reasonably accurate ages.

3.8. Age and signal biases

As discussed, the initial objective is to obtain a time-series with reasonably accurate ages and signals. If either the ages or signals have

Table 2
REDFIT smoothing parameter for Welch's method.

Study	Bin size (myr)	Interval (*Ma*)	No. of bins (n)	n_{50} from Eq. (4)	n50 used in REDFIT
1	30	4350–0	145	−0.8	1
2	10	3900–0	390	0.6	1
3	3	3702–0	1234	3.4	3
4	1	2270–0	2270	5.7	6
5	0.3	1450–0	4833	9.7	10
6 & 7	0.1	541–0	5410	10.4	15

questionable accuracies, then interpreting results might lead to flawed conclusions. For detrital zircon, global sampling, disproportionate sampling, selecting the best U—Pb age, and filtering bias are four key factors that could bias the time-series ages and signals.

We assess the global extensiveness of samples by plotting their GPS coordinates on maps (Fig. 3). At this point, the nearly one million record Combined-DB is approaching global coverage, and it has the most accurate U—Pb ages and the most complete global coverage. Thus, the Combined-DB is our preferred database for evaluating results. However, many war-torn, arid, and polar regions of the globe remain undersampled. Thus, further work is required attain global coverage – especially after considering the heterogenous nature of detrital zircon age distributions.

Biases related to the heterogeneity of U—Pb ages combined with unusually heavy convenience sampling in regions such as Western Europe, the Western USA, and China are minimized by weighting the samples proportionally to the geographic surface areas encompassing the samples (Lo and Watson, 1998; Stehman and Selkowitz, 2010; Puetz et al., 2017; Puetz and Condie, 2020). All detrital zircon age distributions in studies 1 through 6 employ this geographic weighting strategy (Section 3.1).

A critical problem related to U—Pb geochronology is how to select the best age from the three primary chronometers. A comprehensive study of detrital zircon ages (Puetz et al., 2021) demonstrates that non-iterative, probability-based ages (Puetz et al., 2021) and iterative concordia ages from *IsoplotR* (Vermeesch, 2018) both produce nearly identical age distributions for concordance classes 1 through 5 (Puetz et al., 2021). Zircon analyses defined as class 1 concordance (~100 ± 1% concordant) are generally agreed to be highly accurate. Because the U—Pb age distributions for classes 1 through 5 replicate the age distribution from the concordant class 1 records, we are confident all ages from the 5 concordance classes are accurate. The same type of reproducibility fails for all arbitrary age-cutoff models. Thus, by using non-iterative, probability-based ages, as done here, a higher degree of accuracy is achieved (versus the current convention of a 1000 *Ma* cutoff for switching from $^{206}Pb/^{238}U$ ages to $^{207}Pb/^{206}Pb$ ages) when estimating time-series age peaks. Moreover, U—Pb zircon analyses have 2σ uncertainties (Fig. 4, green curve) as small as 0.5% to 3.0% of the U—Pb age, making zircon ages among the most precise of all types of geological data. Because detrital zircon ages essentially span Earth history, a means exists for producing reasonably accurate time-series with an immensely large number of cyclic repetitions – something that is not yet possible using other types of geological data. Accuracy and duration are two key requirements for achieving reliable spectral analysis results. Thus, detrital zircon time-series stand out as a premier means for reliably detecting periodicities in geological processes. In addition to the 91-myr periodicity detected in our detrital zircon tests for the Phanerozoic and Neoproterozoic, the interval from 4300 to 2700 *Ma* also shows 91–94 myr periodicity during the Hadean and Archean (Condie et al., 2018). Thus, the long duration of these detrital zircon time-series provides a means for testing cyclic persistence.

Another concern arises from our decision to exclude detrital zircon analyses with a concordance class greater than 5. Excluding such records will contribute to a filtering bias (Gehrels et al., 2019) if the unknown age distribution from the rejected records differs from the known age distribution from the accepted records. While this is certainly possible, the age distributions for classes 1 through 5 are nearly identical. This means that a filtering bias is not detected for the first five concordance classes, and thus, is unlikely to be present in the rejected records. Thus, we dismiss filtering bias from the list of legitimate concerns.

When attempting to assign ages to sedimentary sequences, a different type of problem emerges. The only points with reliable ages are isotopically dated tie-points, which are generally polarity chrons (Berggren et al., 1995). Between tie-points, researchers apply one of two approaches: (a) assume a constant sedimentation rate and use linear interpolation to estimate ages, or (b) assume a variable sedimentation rate between tie-points and tune the ages to periodicities postulated by the Milankovitch hypothesis (Milankovitch, 1941). The second approach is widely used. For instance, between tie-points Lisiecki and Raymo (2005) utilize a Milankovitch model (Laskar et al., 1993) to assign ages to the LR04 stack of global benthic $\delta^{18}O$ records – a stack often used by researchers to assign ages to sedimentary sequences.

A key problem with this methodology is that the procedure of tuning sedimentary sequences to a Milankovitch model biases spectral power toward Milankovitch frequencies, which many already recognize (Hinnov, 2000; Neeman, 1993; Shackleton et al., 1995; Hilgen et al., 2015; Puetz et al., 2016). Biasing time-series this way leads to a type of circular reasoning where each test of an "orbitally tuned" sedimentary sequence reveals Milankovitch periodicity, which is incorrectly perceived as reaffirmation of the Milankovitch hypothesis. Of course, a legitimate test of any hypothesis requires complete independence between the data and the model being tested (Aber, 1997; McDowall, 2004; Waters and Craw, 2006; Crisp et al., 2011). Because the practice of "orbital tuning" began almost immediately after Hays et al. (1976) reignited interest in the Milankovitch hypothesis, the hypothesis has never been rigorously and repeatedly tested with completely independent data. Despite orbital tuning at the kyr scale, ages at the myr scale of sedimentary sequences are essentially dated isotopically, meaning that orbital tuning bias is minimal when evaluating periodicities >1-myr.

For these reasons, we consider $\delta^{18}O$ time-series as valid climatic proxies above the Milankovitch frequencies, but still prefer focusing on detrital zircon age distributions for at least five reasons. The current set of global detrital zircon databases include: (a) this set of seven completely to partially independent databases allow for testing the reproducibility of results, (b) global sampling of detrital zircon is extensive, covering all but of few regions of the global continental crust, (c) the sample size is large, now approaching 1 million records for the Combined-DB, meaning that age peaks (the signals) can be estimated reasonably well, (d) detrital zircon collected from a cluster samples generally have origins covering a wide area, meaning the cluster sample behaves like a random sample covering a large area when compared to an cluster sample from an igneous rock, and (e) U—Pb ages are highly accurate, with the mean 2σ uncertainty generally ranging from only 0.5% to 3% of the age (Fig. 4). Coupled with the high sample sizes, age-peak uncertainties are much smaller than errors for individual ages. For these reasons, we consider U—Pb detrital zircon time-series to be among the most accurate of all available time-series in the natural sciences – both in terms of its signals (y-axis age counts) and its ages (x-axis), which span most of Earth's history.

3.9. Bandpass filtering

Bandpass filtering with a Gaussian kernel (Babaud et al., 1986) removes high frequency variation and dampens low frequency variation. In the process a middle-range of frequencies remain for time-series studies. As performed here, the two filtering steps are: (a) removing high frequency variation by binning records, which eliminates all periodicities less than the Nyquist limit, which is twice the bin-size (Shannon, 1949), and (b) attenuating low frequency variation after dividing the time-series with a moving 61-weight Gaussian kernel. Table 1 lists the bin-size (bandwidth) and time-series ranges for each study. We conservatively prefer studying periodicities at about four times the Nyquist limit, which is eight times the bin size. Collectively, the seven studies assess periodicity in a range from 300-kyr to 999-myr, with some overlap of bands being analyzed in successive studies. After applying the bandpass filters, the time-series are transformed into stationary sequences. This transformation makes them optimal for various types of analyses, including assessments of endpoint bias, spectral analysis, and cross correlation analysis.

3.10. Deposition age bias

A depositional age bias occurs for any detrital zircon sample that is not a modern sediment. Sedimentary rocks yield zircon grains older than the depositional age but no concordant grains younger that the depositional interval (Reimink et al., 2021; Puetz and Condie, 2021) which biases the age-distribution against young ages. Estimating the global U—Pb age distribution from modern-sediments is one option for eliminating depositional bias. Another option is to progressively weight bins with younger ages having weights higher than bins with older ages. This is accomplished by weighting the records proportionally to the number of records for each depositional period. By separating the Combined-DB into two parts (Dep-Modern-DB and Dep-200 *Ma*-DB), two large databases are rendered that are completely independent of the other. The Combined-DB and its two subsets are weighted to compensate for depositional age bias. Thus, the three age distributions should simulate an age distribution from modern sediments.

3.11. Reproducibility

After weighting the records for biases that are adjustable, a means exists for testing the degree to which periodicities detected in one detrital zircon time-series are reproducible in another time-series. Reproducing results is a key aspect of scientific research. Reproducibility concerns the way analyses are conducted and involves both ethical and methodological components (Thompson and Burnett, 2012). Reproducible research ensures that analyses from a particular methodological study can be conducted by independent investigators with equivalent results (Thompson and Burnett, 2012).

Here, we assess the reproducibility of periodicities detected in the U—Pb detrital zircon age distribution by conducting six sets of tests for variable frequency ranges (Table 1), with each set of tests involving time-series from the seven detrital zircon databases (Section 2). We test for coherency based on the consistency of (a) spectral peaks in periodograms and (b) phase alignments in the correlograms. When periodicities and phase alignments are consistently reproduced at high confidence levels, we classify a cycle as being validated, and include the validated cycle in a model. In some instances, alignments are marginal. This produces a marginal validation requiring further testing with new independent data, Additionally, marginal validations are generally assigned small weights in the models.

Pre-analysis assessments involving best U—Pb age methods, stationarity (Section S3 of Supplement S1), and sampling densities influence our decisions on which databases and which portions of a time-series qualify for each test (Fig. 4, blue bars). For the ultra-low and low frequency tests, all seven detrital zircon age distributions are included. For the medium-low and medium high frequency tests, age distributions from Puetz-2019-DB, Puetz-2021-DB, Combined-DB, Dep-Modern-DB, and Dep-200*Ma*-DB are included. The high and ultra-high frequency tests are limited to age distributions from Puetz-2019-DB, Puetz-2021-DB, Combined-DB, Dep-Modern-DB.

Fig. 6 illustrates correlograms that compare the seven low frequency time-series with a 171.24-myr sinusoidal model having an age-peak at 116.3 *Ma*. The ~171-myr cycle is validated because (a) the seven correlogram peaks generally align with the model (Fig. 6, black vertical line) for the two segments (Fig. 6a,c) and the entire 3900–0 *Ma* interval (Fig. 6b), (b) the confidence levels exceed 95% for five time-series and the mean correlation curve (Fig. 6b), and (c) the test spans 23 cyclic repetitions, which is sufficiently large for a meaningful test. Obviously, the half segments (Fig. 6a,c) contain fewer cyclic repetitions (only 11), making them more prone to errors in measuring periodicity. As often happens with a validated cycle, maxima for the half segments general align with the model (vertical black line) but with some divergence and lower confidence levels than the alignment for the entire time-series. Thus, we do not expect perfect alignments with 95% confidence from all seven correlograms, but we do expect the weight of the evidence and

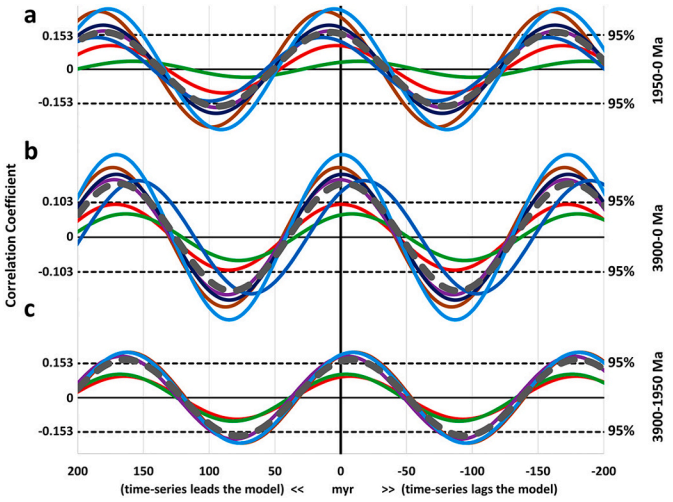

Fig. 6. Example of coherent correlograms. Low frequency test for the interval 3900–0 *Ma*. Correlograms compare a 171.84-myr sinusoidal model (maximum at 111.05 *Ma* and 23 cyclic repetitions) to seven age distributions: (red) Voice-DB, (green) Roberts-DB, (brown) Puetz-2019-DB, (purple) Puetz-2021-DB, (dark blue) Combined-DB, (medium blue) Dep-Modern-DB, (light blue) Dep-200 *Ma*-DB, and (thick dashed gray) average of the seven correlograms. (For interpretation of the references to color in this figure legend, the reader is referred to the web version of this article.)

the average correlograms (thick dashed gray curves) to approach the 95% band for the halves and exceed the 95% band for the entire age range to fully validate a cycle.

Identical tests are progressively conducted at all frequencies for all six sets of tests, recorded as power spectra of maximum mean correlations, and then displayed in the Results (Section 4). Many of these tests failed to validate cycles. For example, the correlogram test of a 65-myr cycle (Fig. 7) failed to show evidence of coherent periodicity. In the half segments (Fig. 7a, c), the dashed gray curves are misaligned with the model, most of the confidence levels fall below 95%, and the individual correlograms tend to be misaligned with the others. By systematically evaluating all frequencies this way, the multi-test correlograms reveal

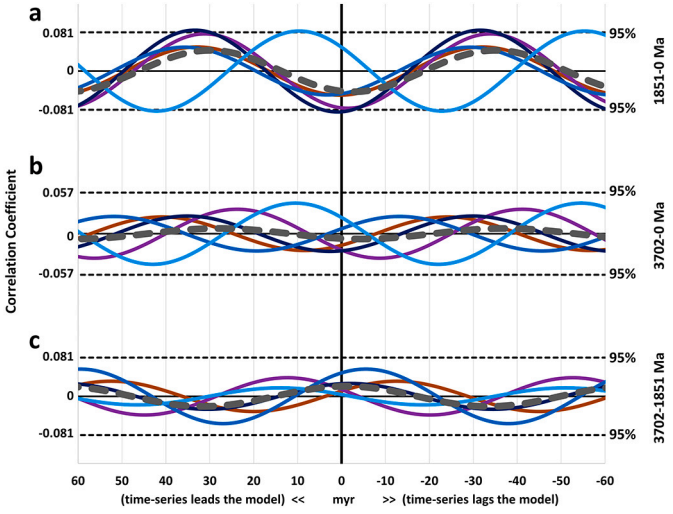

Fig. 7. Example of incoherent correlograms. Medium-Low frequency test for the interval 3702–0 *Ma*. Correlograms compare a 65-myr sinusoidal model (maximum at 62 *Ma* and 57 cyclic repetitions) to five age distributions: (brown) Puetz-2019-DB, (purple) Puetz-2021-DB, (dark blue) Combined-DB, (medium blue) Dep-Modern-DB, (light blue) Dep-200 *Ma*-DB, and (thick dashed gray) average of the five correlograms. (For interpretation of the references to color in this figure legend, the reader is referred to the web version of this article.)

the degree of reproducibility for the half segments and full intervals. If the time-series for the three segments produce similar correlograms at high confidence levels, then the likelihood increases these same results will be reproducible for new tests with data completely independent from the seven detrital zircon databases.

4. Results

Results are given in two sections – correlograms and periodograms. The correlogram section is limited to a special sequence of eight period-tripling cycles, which are either fully validated or marginally validated. Rounded to three digits, this tripling sequence has periods of ~0.373, 1.12, 3.35, 10.1, 30.2, 90.5, 272, and 815 myr, with each cycle having ±1% uncertainty. Analyses of the correlograms literally involved thousands of tests, far too many to present here individually. However, the collective results from the correlogram tests are summarized in the top panel of the periodograms (Section 4.2) by plotting the "maximum mean correlation" at evenly spaced frequencies. This generates a spectrum that behaves like an average periodogram. The maximum mean correlation curves generally display the same spectral peaks as the individual periodograms, but sometimes the periodograms diverge. Because a maximum mean correlation curve provides a type of weighted average for the seven power spectra, it is optimal for assessing reproducibility.

4.1. Correlograms

Among the various periodicities identified as likely candidates for reproducible cycles, one set stands out for multiple reasons: (a) starting at 0.3725-myr, each successive cycle in this sequence has a period exactly three times larger than its predecessor up to 814.7-myr; (b) with the exception of the 30.2-myr cycle, the eight period-tripling cycles share a common maximum at ~265.35 *Ma*; and (c) with only a few exceptions, the period-tripling cycles synchronously align with the models (within ±10% of the period) when tested via cross-correlations for each full time-series and its half segments. Table 3 summarizes some key properties of the period-tripling sequence, with the associated correlograms illustrated in Figs. 8-15.

Periodograms of detrital zircon age distributions typically reveal periodicity ranging from 730 to 830-myr – including the power spectra in this study. Unless each repetition of the ~800 myr cycle is sampled perfectly, estimating periodicity for a time-series with only five cyclic repetitions presents formidable challenges (Section 3.4, Fig. 5). In this instance, the cross-correlation analysis (Fig. 8) constrains the uncertainty by identifying 815-myr as the period which produces the highest mean correlation among the seven time-series for the entire 4350–0 *Ma* interval (Fig. 8b) and the two segments (Fig. 8a, c). The mean correlogram curve (Fig. 8b, dashed gray) deviates from the model's 265.35 *Ma* maximum (Table 3, last column) by a miniscule 0.4%. None of the correlograms produce perfect fits for the half segments and full intervals. Yet, the tests involving 815-myr (Fig. 8) and of the 272-myr models (Fig. 9) produce results that range from strong to moderately strong for the segments, and generally strong for the entire intervals. This reaffirms the hyperbolic deterioration in the reliability of periodicity estimates as cyclic repetitions decrease (Fig. 5) and demonstrates the heightened importance of increasing cyclic repetitions when data availability and data quality allows for such extensions.

The 90.5-myr periodicity is the next cycle in the period-tripling sequence. For this frequency range, correlograms from the Voice-DB and Roberts-DB are excluded for one or more of the following reasons: (a) non-stationarity in the bandpass filtered time-series, (b) insufficient sampling as determined from low record counts per bin, or (c) increased age-uncertainty from usage of an age-cutoff model for assigning the best U—Pb age. The remaining five correlograms for the 3702–1851 segment (Fig. 10c) reveal weak confidence levels but near-perfect alignments with the model. However, the correlograms for the 1851–0 *Ma* segment (Fig. 10a) and the entire 3702–0 *Ma* interval (Fig. 10c) show both high confidence levels and nearly perfect alignments with the 90.5175-myr model with a 265.35 *Ma* peak. In fact, the maximum mean correlation (Fig. 10b, dashed gray) only deviated from the model (Fig. 10, black vertical) by 0.62%. If one interprets the small deviations (0.40%, 1.62%, and 0.62%) from the three models as a measurement errors, then the collective results support the hypothesis of a 90.5, 272, and 815-myr period-tripling sequence propagating harmonically throughout Earth history.

Validating the 30.2-myr cycle is the most problematic of the eight cycles in the period-tripling sequence. The correlograms testing the 30.2-myr cycle are misaligned with low confidence levels (Figs. 11a-11c), whereas if the model is revised to 30.55-myr, the correlograms are perfectly aligned with high confidence levels (Figs. 11d-11e). Could the 1.26% difference between the hypothetical cycle (30.17-myr) and the measured cycle (30.55-myr) be an artifact of sampling errors or measurement errors? Some sampling/measurement error seems likely. However, these errors are unlikely to contribute entirely to the 1.26% difference because of the 75 cyclic repetitions in the time-series. A more likely explanation is that a combination of incorrect periodicities in the period-tripling models, sampling errors, and other measurement errors collectively contribute to the 1.26% divergence. Further testing with a new independent detrital zircon data will be required to determine why the 30.2-myr cycle deviates 1.26% from the measured cycle. Even though this test fails to completely validate the 30.2-myr cycle, the 1.26% difference is close enough to consider this as either a marginal validation or a candidate for validation.

The correlograms testing the 10.1-myr cycle for the 725–0 *Ma* segment (Fig. 12a) are mostly aligned with the model at high confidence levels, whereas the correlograms for the 1450–725 *Ma* segment (Fig. 12c) are well aligned but at low confidence levels. As with the 90.5, 272, and 815-myr cycles, the 10.1-myr cycle is well aligned for the entire 1450–0 Ma interval (4.87% deviation) and at very high confidence levels. The relatively low correlations for the 1450–725 *Ma* could indicate that we stretched the analyses beyond the capabilities of detecting the 10.1-myr cycle due to fewer samples per bin and/or larger age-errors in this age-range.

The correlograms testing the 3.35-myr cycle for the 1200–0 *Ma* interval (Fig. 13b) are generally aligned with the model (4.47% deviation) but just below the 95% confidence level. Otherwise, the correlograms patterns are similar to the 10.1-myr tests. Specifically, the weaker

Table 3
Summary of correlogram results for main period-tripling sequence.

Figure number	Period of cycle (myr)	No. of cyclic reps	Age-range with aligned cycle (*Ma*)	Model common peak (*Ma*)	Optimum peak (*Ma*)	Common peak – optimum peak as % of period
8	814.66	5	4350–0	265.35	268.61	−0.40%
9	271.55	14	3900–0	265.35	269.76	−1.62%
10	90.518	41	3702–0	265.35	265.91	−0.62%
11	30.173	75	2270–0	265.35	251.55	45.74%
12	10.058	144	1450–0	265.35	264.86	4.87%
13	3.3525	358	1200–0	265.35	265.50	−4.47%
14	1.1175	242	270–0	265.35	265.45	−8.95%
15	0.3725	725	270–0	265.35	265.33	5.37%

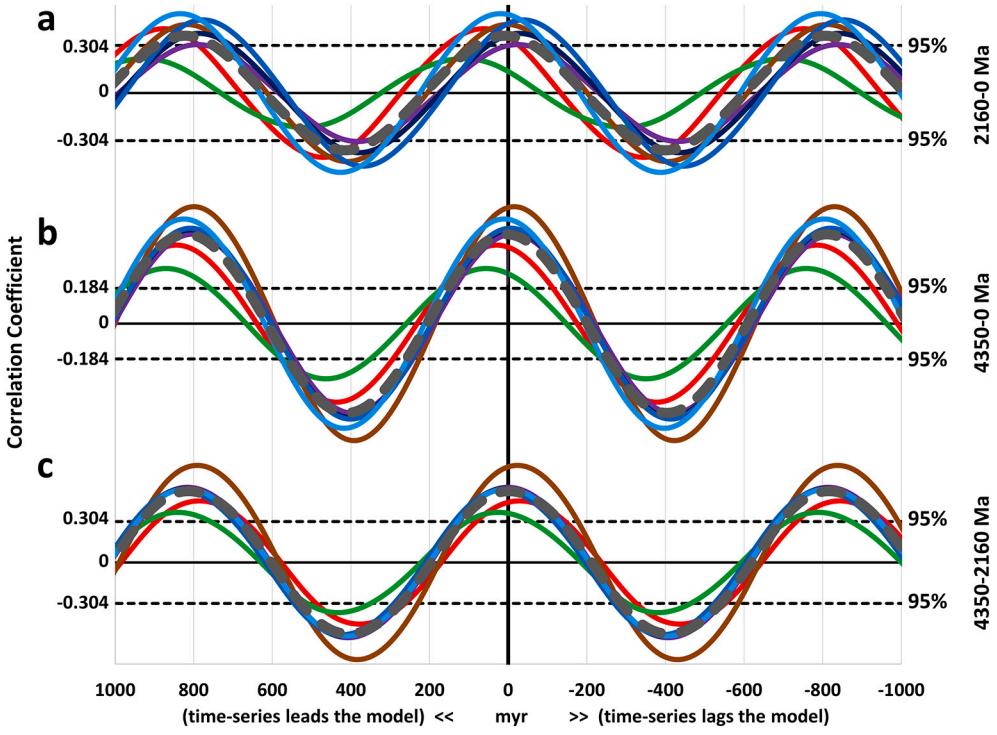

Fig. 8. Correlograms testing 815-myr periodicity. Ultra-low frequency test for the interval 4350–0 *Ma*. Correlograms compare an 814.6575-myr sinusoidal model (maximum at 265.35 *Ma* and 5 cyclic repetitions) to seven age distributions: (red) Voice-DB, (green) Roberts-DB, (brown) Puetz-2019-DB, (purple) Puetz-2021-DB, (dark blue) Combined-DB, (medium blue) Dep-Modern-DB, (light blue) Dep-200 *Ma*-DB, and (thick dashed gray) average of the seven correlograms. (For interpretation of the references to color in this figure legend, the reader is referred to the web version of this article.)

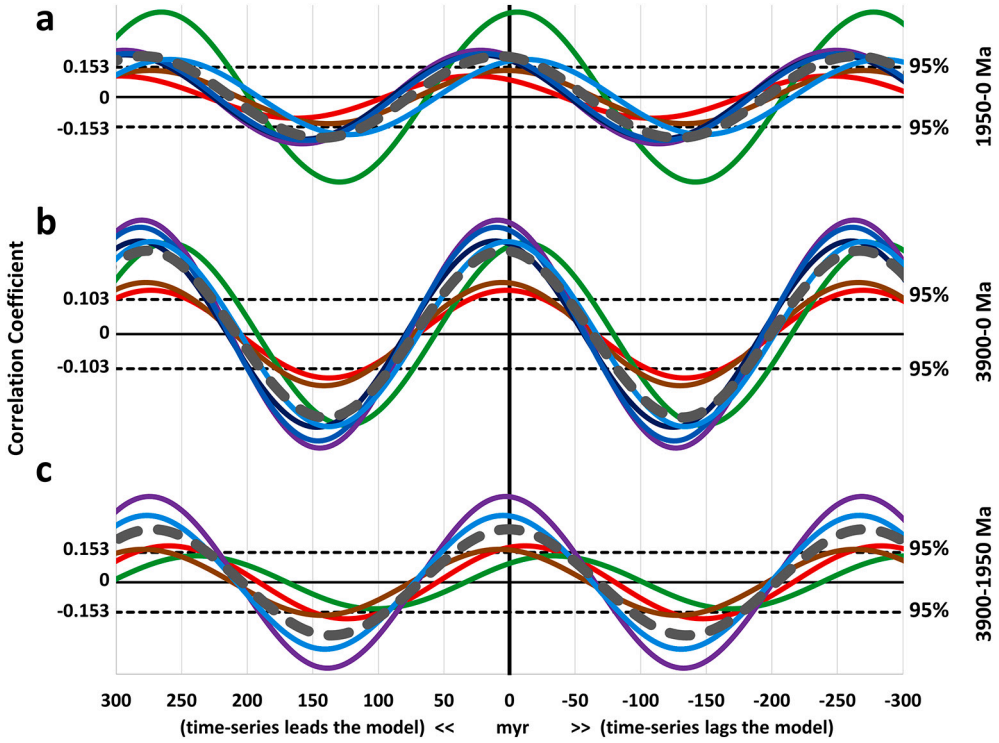

Fig. 9. Correlograms testing 272-myr periodicity. Low frequency test for the interval 3900–0 *Ma*. Correlograms compare a 271.5525-myr sinusoidal model (maximum at 265.35 *Ma* and 14 cyclic repetitions) to seven age distributions (refer to Fig. 8 for database color codes).

correlations for the 1200–600 *Ma* (Fig. 13c) could indicate that we stretched the analyses beyond the capabilities of detecting the 3.35-myr cycle due to fewer samples per bin and/or larger age-errors in this age-range. Because the correlograms are well aligned but at confidence levels slightly below 95%, we treat the 3.35-myr cycle as a marginal validation.

The final two sets of correlograms (Figs. 14-15) test the 1.118-myr and 0.373-myr cycles for the interval 270–0 *Ma*. Like the 3.35-myr tests, these ultra-high frequency cycles generally align with the models, but the confidence levels are below those required for strong validations. For the entire 270–0 *Ma*, the mean correlogram testing the 1.118-myr cycle does exceed the 95% confidence level (Fig. 14b), and

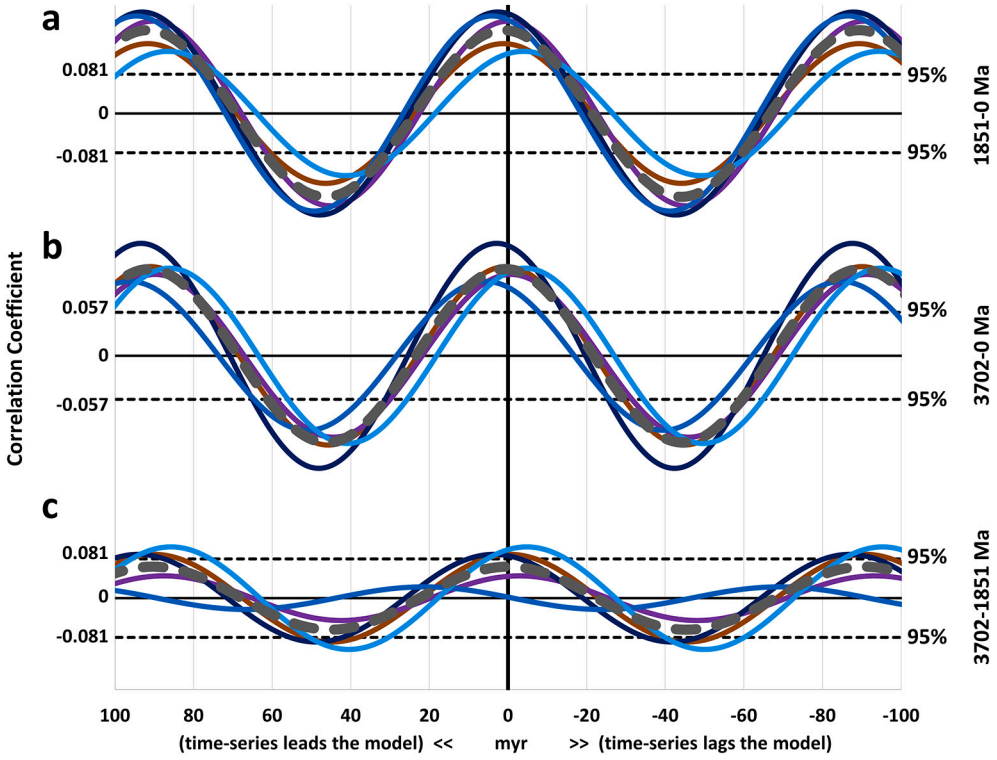

Fig. 10. Correlograms testing 90.5-myr periodicity. Medium-low frequency test for the interval 3702–0 *Ma*. Correlograms compare a 90.5175-myr sinusoidal model (maximum at 265.35 *Ma* and 41 cyclic repetitions) to five age distributions: (brown) Puetz-2019-DB, (purple) Puetz-2021-DB, (dark blue) Combined-DB, (medium blue) Dep-Modern-DB, (light blue) Dep-200 *Ma*-DB, and (thick dashed gray) average of the five correlograms. (For interpretation of the references to color in this figure legend, the reader is referred to the web version of this article.)

the deviation from the model (8.95%) falls within the 10% threshold. Even though this test validates the 1.118-myr cycle, it is by the thinnest of margins. The mean correlogram for the 0.373-myr test falls below the 95% confidence level (Fig. 15b), but the 5.37% deviation between the maximum mean correlation and the model comes close to a synchronous alignment – making this a marginal validation that will require further testing with new data.

In summary, these tests of a hypothetical period-tripling sequence, with periods of 0.373, 1.12, 3.35, 10.1, 30.2, 90.5, 272, and 815-myr, yields generally positive results. The 90.5, 272, and 815-myr components are synchronously aligned at high confidence levels with a sinusoidal model having a common peak at 265.35 *Ma*. These three cycles are likely to be real and reproducible in new, high quality, globally representative, detrital zircon databases. Validating the 30.2-myr cycle as a component of this tripling sequence is problematic because the cycle is found to be 30.55-myr in a bandpass filtered time-series with 74 repetitions, instead of the predicted 30.2-myr periodicity. The 0.373, 1.12, 3.35, and 10.1-myr components align reasonably well (within 10%) with the sinusoidal models sharing a common peak at 265.35 *Ma*; however, the confidence levels sometimes fall short of the 95% confidence threshold. For cycles such as these detected when the bin size is less than 4-myr, the accuracy of U—Pb detrital zircon ages, global sampling representativeness, and smaller samples per bin likely contribute to increased measurement errors. Even those these factors do not prevent detection, they will likely inhibit definitive detection of the 0.373, 1.12, 3.35, 10.1, and 30.2-myr cycles. Future tests with new independent detrital zircon data is required to determine the reproducibility of these high frequency myr cycles.

4.2. Periodograms

The first panel above the periodograms (Figs. 16a-22a) depicts the maximum mean correlation curve – a curve than equates to an average of all periodograms below it. The mean correlation curves also serve as a metric for assessing the reproducibility of periodicities. At the very top of each figure (Figs. 16-22), the blue numbers specify the number of cyclic repetitions, which correspond to hypothetical harmonic cycles designated by vertical gray lines. The green and red numbers in the second row corresponds to the periodicities of the vertical gray lines. The primary period-tripling cycles of 0.375, 1.12, …, 815-myr are assigned to the green harmonic group, whereas the cycles that do not fit with the green harmonics are assigned to the red harmonics. After analyzing the periodograms and maximum mean correlation curves for possible harmonic combinations from the first six prime numbers (2, 3, 5, 7, 11, and 13), the only consistent harmonics that fit the data were found in multiples of 2 and 3. Thus, the period-doubling and period-tripling sequences became the basis for a tentative hypothesis. Even though the green and red harmonics have no obvious direct link, they are likely connected for two reasons: (a) the red harmonics have a period 1.0305 times larger than the corresponding green harmonics, which can be thought of as the green harmonics sometimes red-shifted (increased periods of 1.0305, reduced frequencies) to a red harmonics; and (b) in a range from one primary period-tripling cycle, p, to the next, a pattern emerged where the green harmonics are predominantly found between p and $p/2$ in the mean correlogram curves (Figs. 16a-22a), whereas the red harmonics are predominantly found between $p/2$ and $p/3$. These distinct ranges are highlighted with light green backgrounds for the green harmonics, and light red backgrounds for the red harmonics. Within the range where green harmonics prevail (between p and $p/2$), 79% of the validated cycles are green and 21% are red. Within the range where red harmonics prevail (between $p/2$ and $p/3$), this reverses and only 23% of the validated cycles are green while 77% are red. If the comparison is restricted to the 25 to 1000-myr range (Figs. 16-18) where sampling densities are the highest and relative age uncertainties are the smallest, then the green-red distribution is 94% green and 6% red within the green bands, and 7% green and 93.3% red within the red bands. Thus, we tentatively interpret the 1.0305 redshift within the $p/2$ and $p/3$ range as real, and later discuss possible meanings.

Figs. 16-22 illustrate the alignments of the hypothetical harmonics with peaks in the maximum mean correlation curves and spectral peaks in the periodograms. Section 5 through 9 discuss individual results, collective results, and additional interpretations. Table 4 summarize the

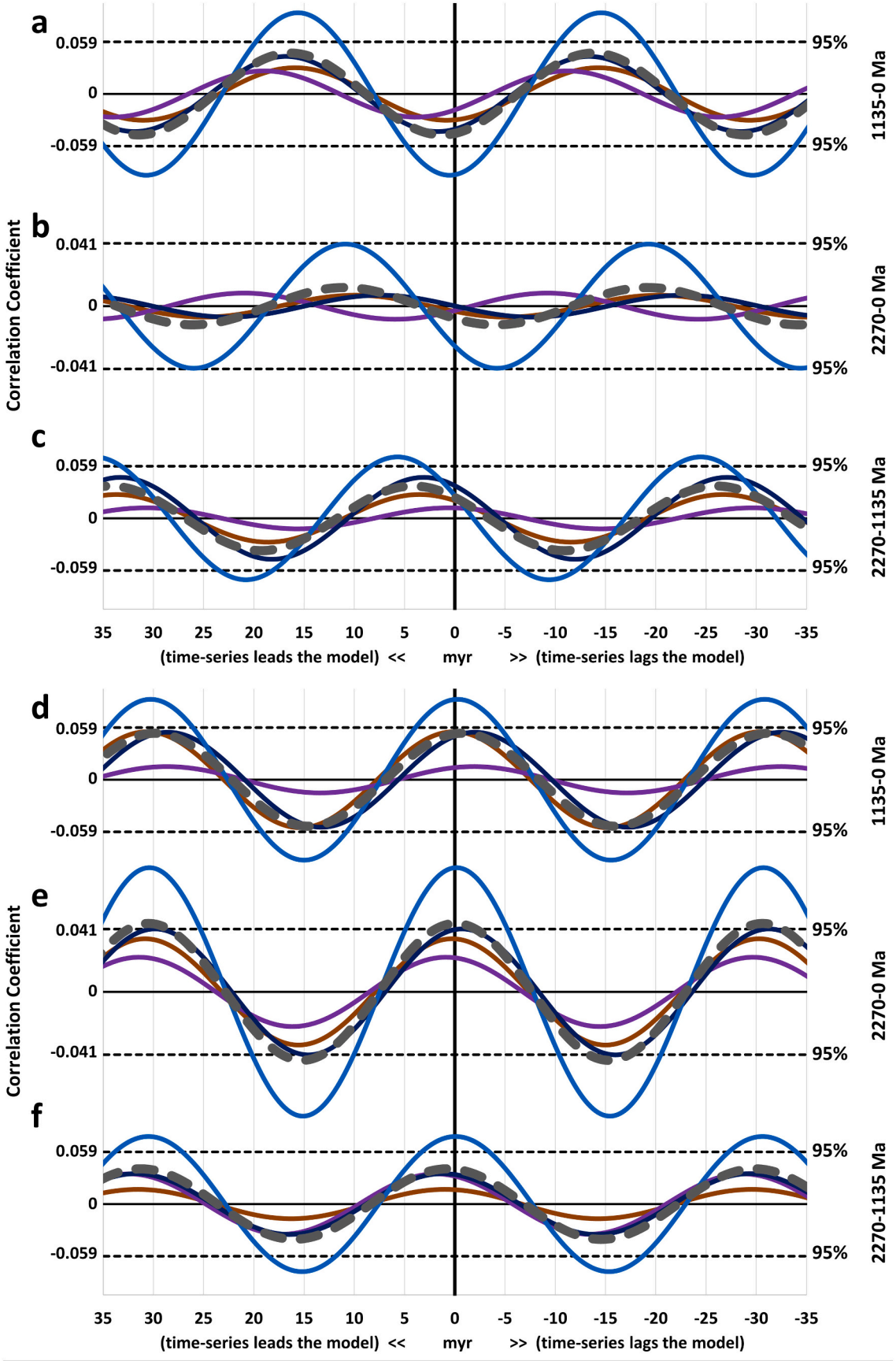

Fig. 11. Correlograms testing 30.2-myr periodicity. Medium-low frequency tests for the interval 2270–0 *Ma*. Panels (a-c): The first set of correlograms compare a 30.1725-myr sinusoidal model (maximum at 265.35 *Ma* and 75 cyclic repetitions) to five age distributions. Panels (d-f): The second set of correlograms compare a 30.55-myr sinusoidal model (maximum at 251.41 *Ma* and 74 cyclic repetitions) to the same age distributions (refer to Fig. 10 for database color codes).

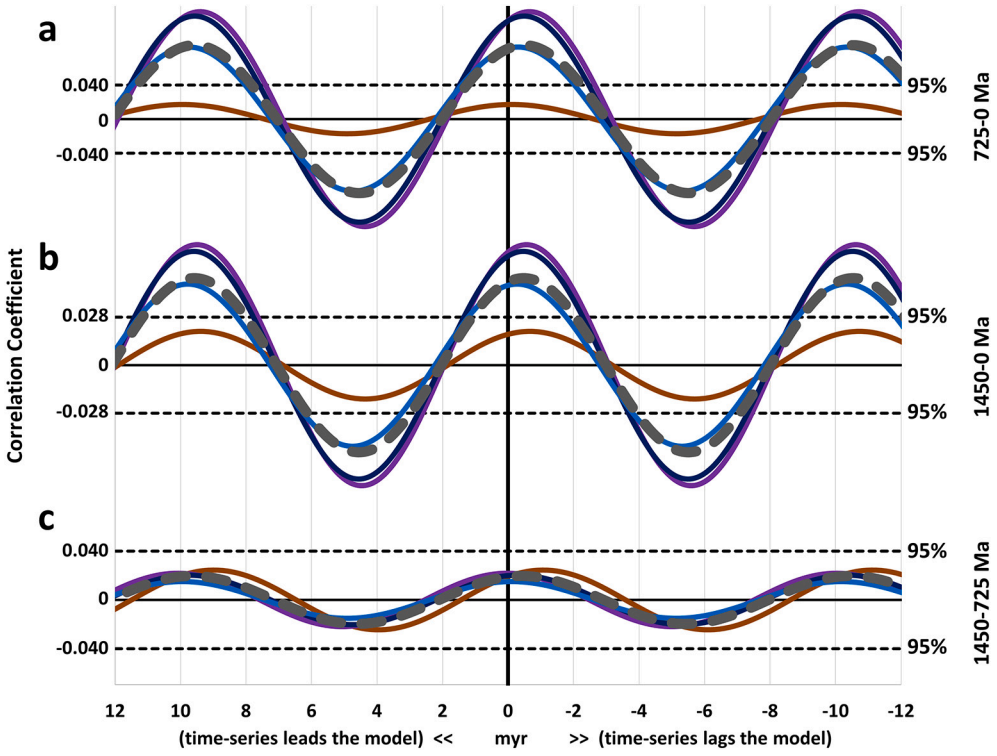

Fig. 12. Correlograms testing 10.1-myr periodicity. High frequency test for the interval 1450–0 *Ma*. Correlograms compare a 10.0575-myr sinusoidal model (maximum at 265.35 *Ma* and 144 cyclic repetitions) to four age distributions: Puetz-2019-DB, (purple) Puetz-2021-DB, (dark blue) Combined-DB, (medium blue) Dep-Modern-DB, and (thick dashed gray) average of the four correlograms. (For interpretation of the references to color in this figure legend, the reader is referred to the web version of this article.)

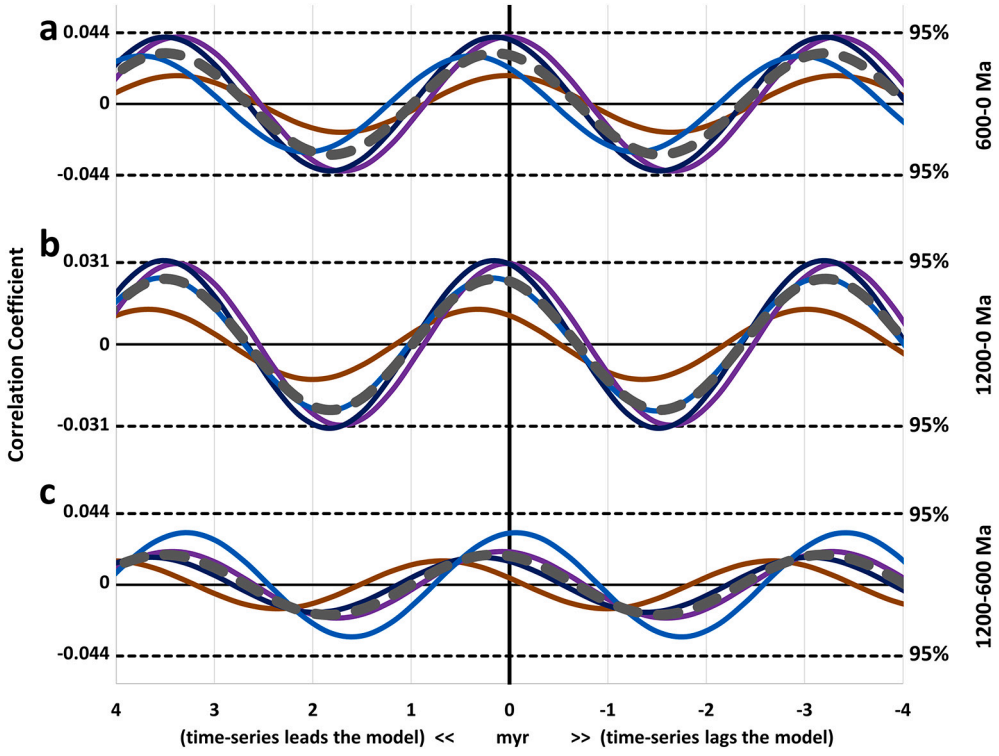

Fig. 13. Correlograms testing 3.35-myr periodicity. Ultra-high frequency test for the interval 1200–0 *Ma*. Correlograms compare a 3.3525-myr sinusoidal model (maximum at 265.35 *Ma* and 358 cyclic repetitions) to four age distributions: (refer to Fig. 12 for database color codes).

periods of hypothetical green harmonics, and Table 5 summarizes red harmonics. Both tables include validated cycles (bold color-coded periods) and unvalidated cycles (regular black text). The rows give hypothetical period-doubling sequences, whereas the columns give hypothetical period-tripling sequences. Validated cycles are used to construct six models (Section 5) to simulate variation in the U—Pb detrital zircon age distribution at various timescales.

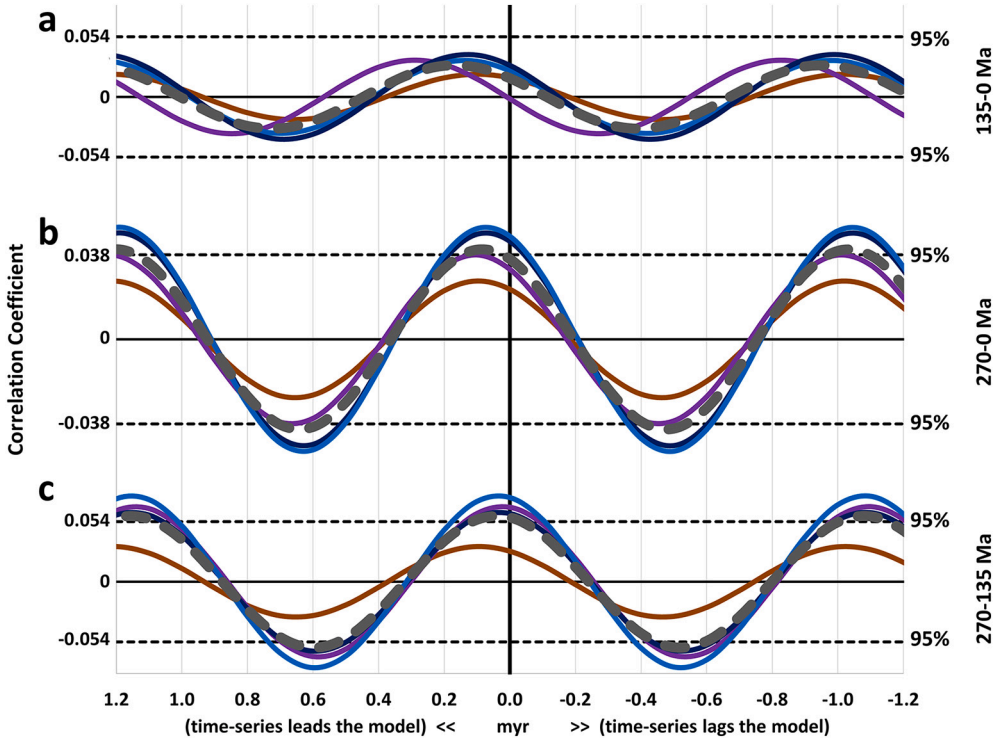

Fig. 14. Correlograms testing 1.1175-myr periodicity. Ultra-high frequency test for the interval 270–0 *Ma*. Correlograms compare a 1.1175-myr sinusoidal model (maximum at 265.35 *Ma* and 242 cyclic repetitions) to four age distributions: (refer to Fig. 12 for database color codes).

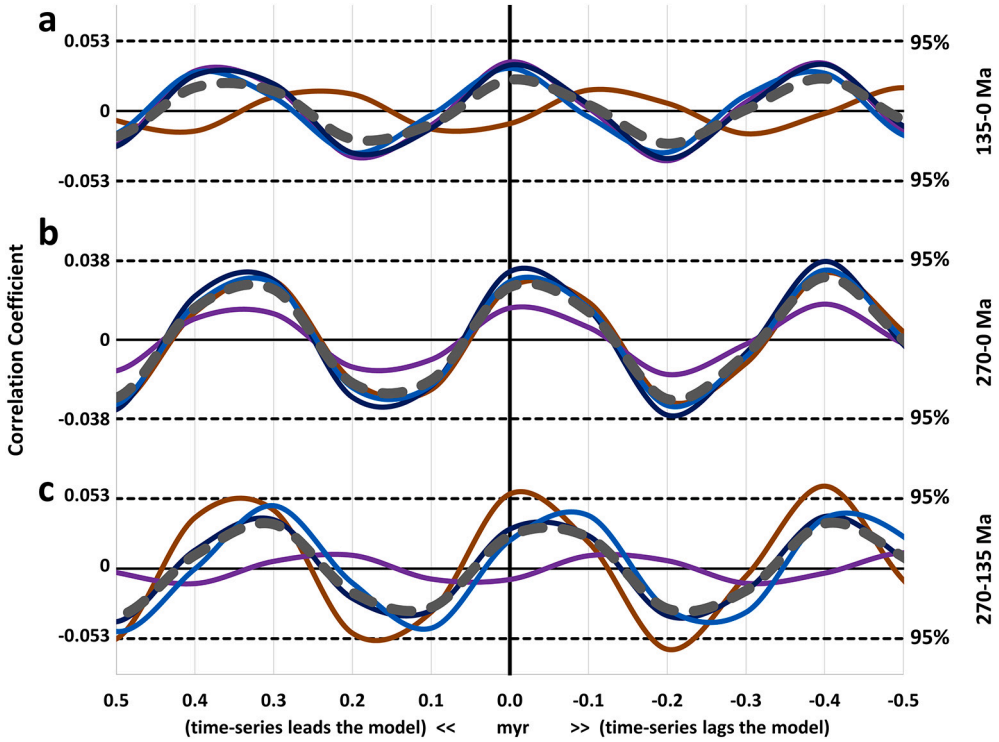

Fig. 15. Correlograms testing 373-kyr periodicity. Ultra-high frequency test for the interval 270–0 *Ma*. Correlograms compare a 0.3725-myr sinusoidal model (maximum at 265.35 *Ma* and 725 cyclic repetitions) to four age distributions. Refer to Fig. 12 for database color codes.

5. Models

Based on the results, six models are developed consisting of sinusoids, as defined by Eq. (2). The ultra-low frequency model contains 11 sinusoids, whereas all other models include 16 sinusoids. Models only include validated or marginal cycles, which are correlated with the Combined-DB. The correlation coefficients serve as weights for the sinusoids. Thus, cycles that correlate highly with the Combined-DB attain

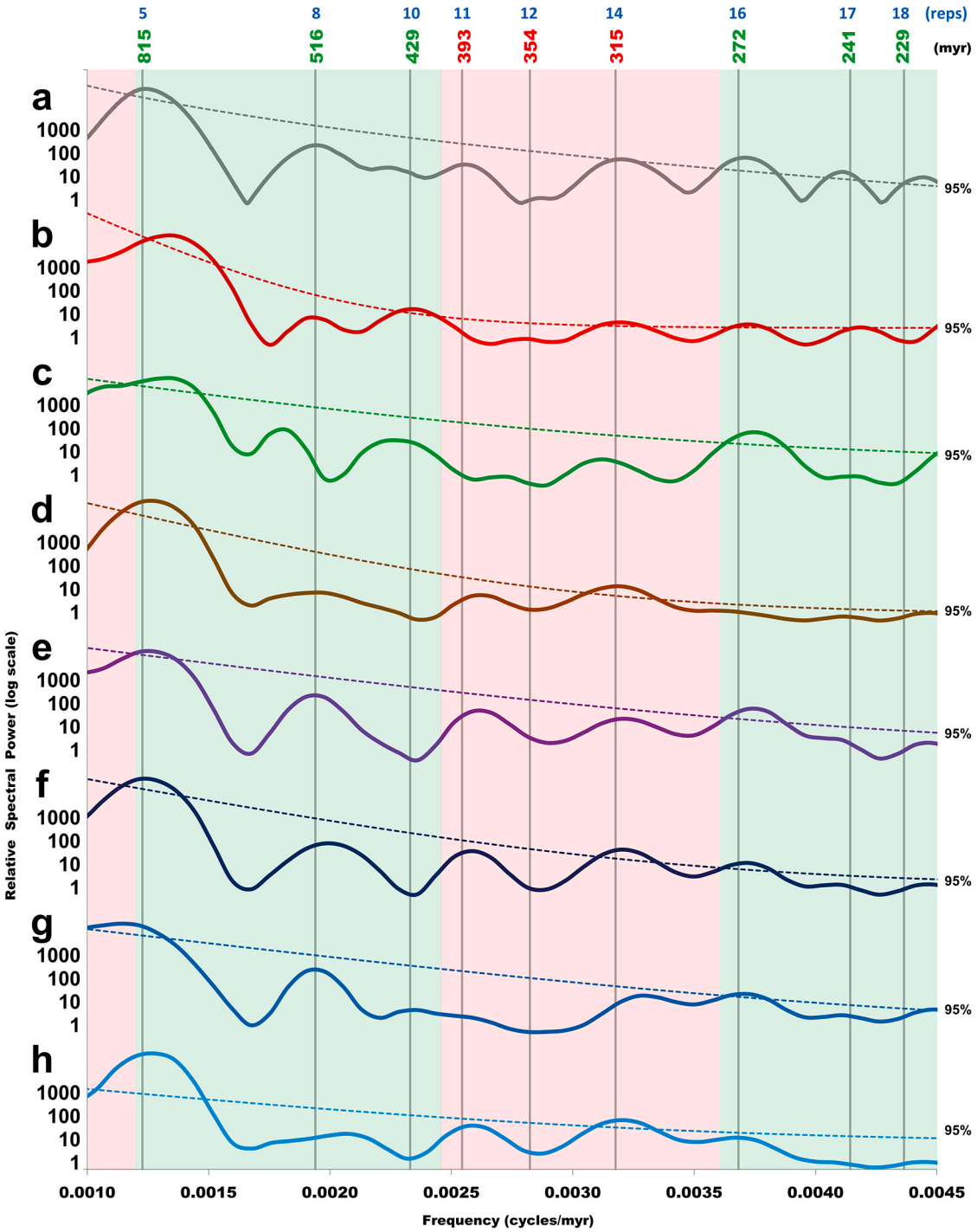

Fig. 16. Maximum mean correlation and periodograms. Ultra-low frequency tests for the interval 4350–0 *Ma*, testing periodicity in the 222–1000 myr range. The number of cyclic repetitions in the top row correspond to the sinusoidal models being tested in the second row. Log scale power spectra: (gray) maximum mean correlations from correlograms, and periodograms for (red) Voice-DB, (green) Roberts-DB, (brown) Puetz-2019-DB, (purple) Puetz-2021-DB, (dark blue) Combined-DB, (medium blue) Dep-Modern-DB, and (light blue) Dep-200 *Ma*-DB. (For interpretation of the references to color in this figure legend, the reader is referred to the web version of this article.)

larger weights than those with small correlations. It is not always clear if a cycle should be validated. When a marginal cycle is included as a candidate, the process self-corrects by either assigning a small weight to it or eliminating the marginal cycle from the model if its correlation is not in the top 16. Using this approach, the six models of global detrital zircon variation are available for testing with data that are completely independent from the seven detrital zircon databases used to construct the models.

Eq. (5) defines the hypothetical million year period-doubling and period-tripling sequences (Tables 4 and 5), $p_{i,j}$, in terms of a base cycle, b = 2.8168582 × 10^{-6} yr for the green harmonics; b = 1.93518882 × 10^{-6} yr for the red harmonics; a timescale divisor, s, set to 10^6 for myr cycles; a doubling index, i, given in column 1 (Tables 4 and 5); and a tripling index, j, given in rows 1 and 14 (Tables 4 and 5).

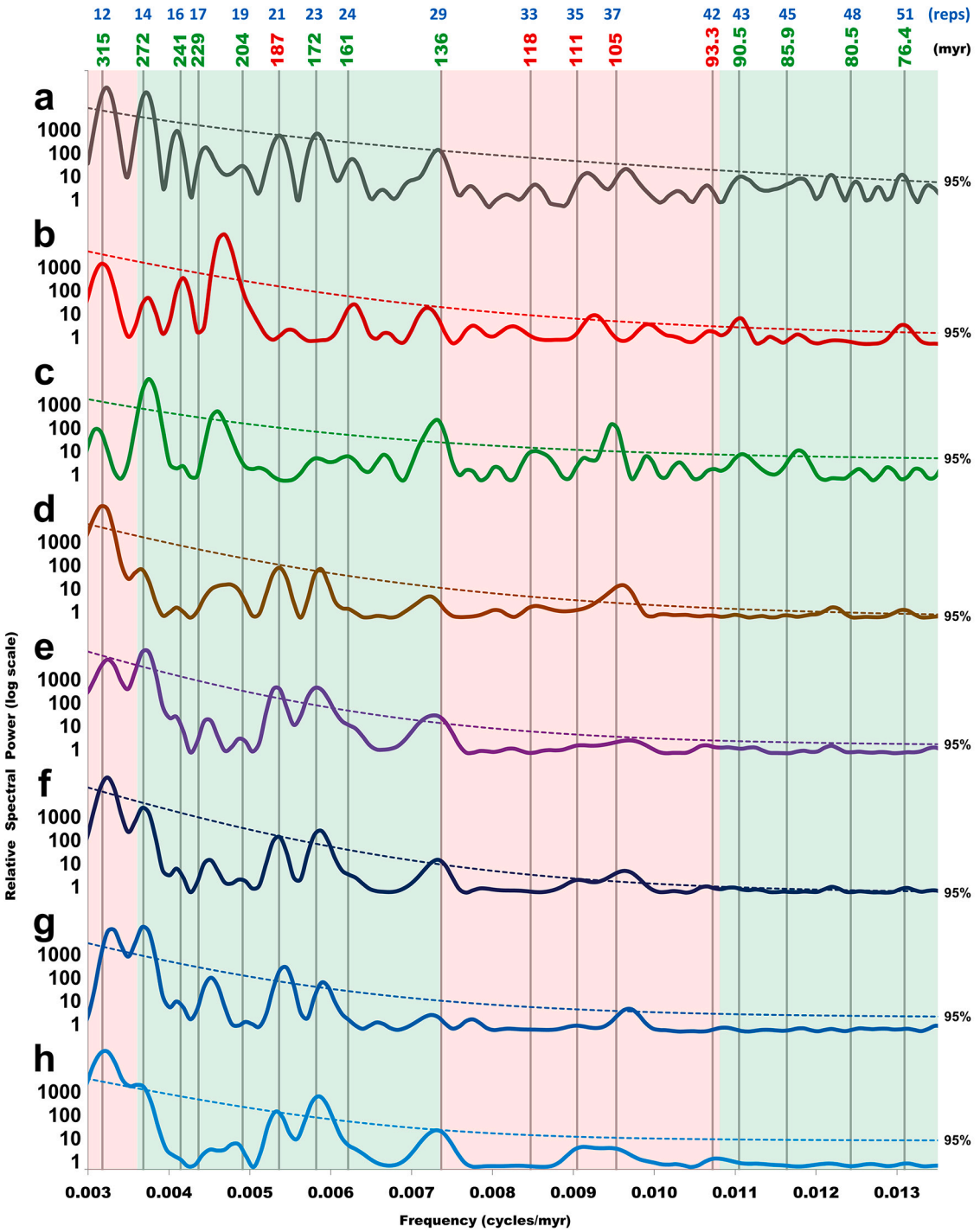

Fig. 17. Maximum mean correlation and periodograms. Low frequency tests for the interval 3900–0 *Ma*, testing periodicity in the 75–333 myr range. The number of cyclic repetitions in the top row correspond to the sinusoidal models being tested in the second row. Refer to Fig. 16 for database color codes of log scale power spectra.

$$p_{i,j} = \frac{b \times 3^i \times 2^j}{s} \tag{5}$$

This equation can be used to test for possible harmonic periodicities in the decadal to kyr range; however, the analyses here primarily focus on myr periodicities. Tables 6 and 7 list the periods, weights, and phase-peaks for the variables in the sinusoidal models, which provides a convenient means for reconstructing the models in this study. The six empirically based models (Figs. 23-28, green curves) are correlated with the bandpass filtered detrital zircon age distributions from the Combined-DB (Figs. 23-28, blue curves).

Using these periods, weights, and phase-peaks (Tables 5 and 6) with the sinusoidal equation (Eq. (2)), the detrital zircon models are tested against independent time-series to determine if the models can be applied to other types of data.

6. Application

The sinusoidal models (Section 5) are derived from time-series

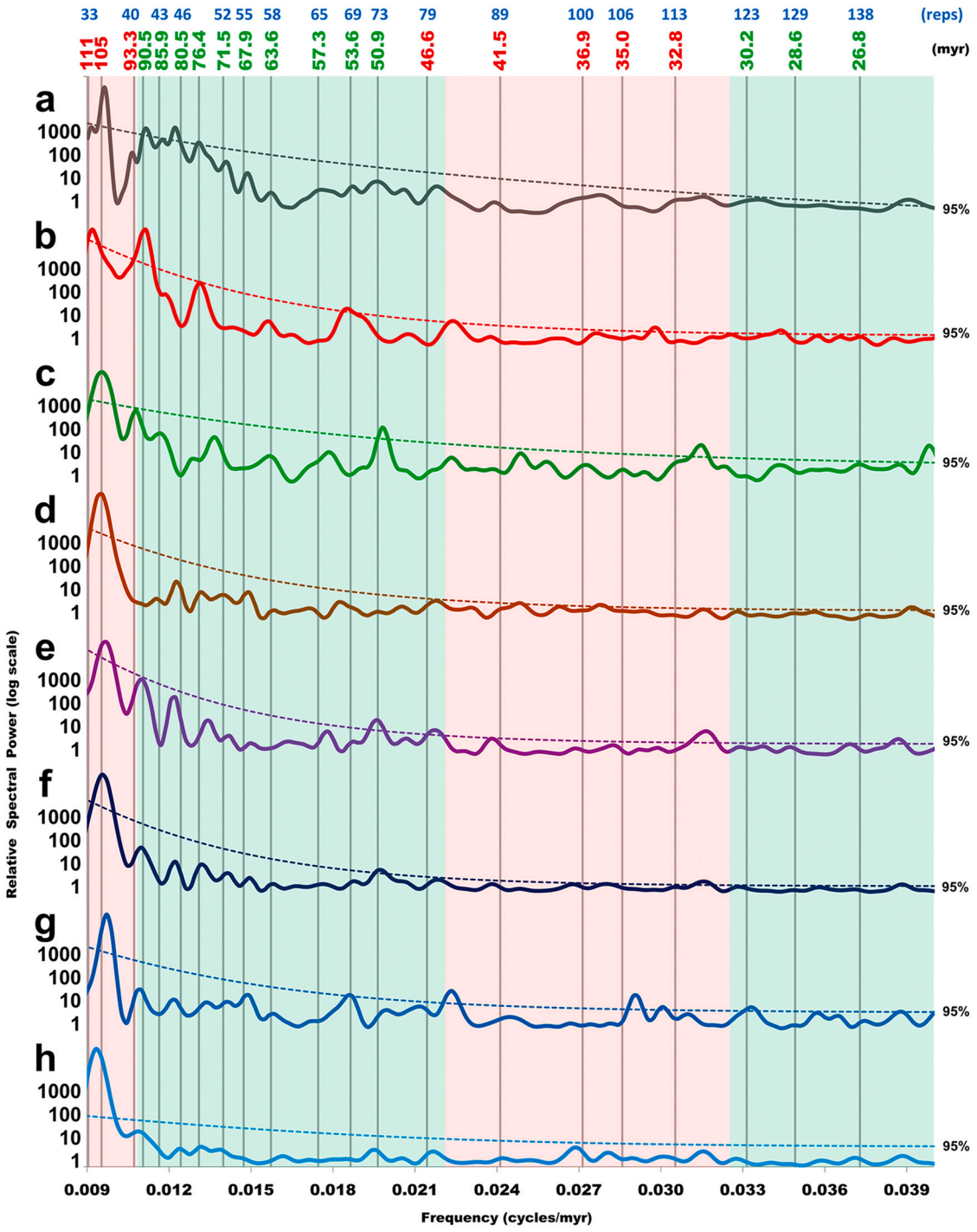

Fig. 18. Maximum mean correlation and periodograms. Medium-low frequency tests for the interval 3702–0 *Ma*, testing periodicity in the 25–111 myr range. The number of cyclic repetitions in the top row correspond to the sinusoidal models being tested in the second row. Refer to Fig. 16 for database color codes of log scale power spectra.

constructed from seven detrital zircon databases. As such, the Section 4 results are not legitimate tests of the model. To accomplish that, a completely new global database of independent detrital zircon ages must be compiled. Because such an independent database will likely remain unavailable for at least another one to two years, immediate evaluations of the detrital zircon models are only possible via comparisons of geological time-series suspected to be linked to the production of continental crust.

The first such test compares the ultra-low frequency model with plate velocities and a bandpass filtered age distribution from U—Pb igneous zircons (Fig. 29). The orange vertical backgrounds correspond to a 393-myr cycle, one of the 11 sinusoidal components of Model 1. Because plate velocities have large unquantified errors (Condie et al., 2021) and only entail five cyclic repetitions, a rigorous test is not possible. With these caveats in mind, plate velocities (Fig. 29a) show evidence of 393-myr periodicity which leads the model by 90-myr, with a correlation of 0.337. The bandpass filtered time-series of U—Pb igneous zircon ages (Fig. 29b) is synchronously correlated ($\rho = 0.701$) with the model (Fic.

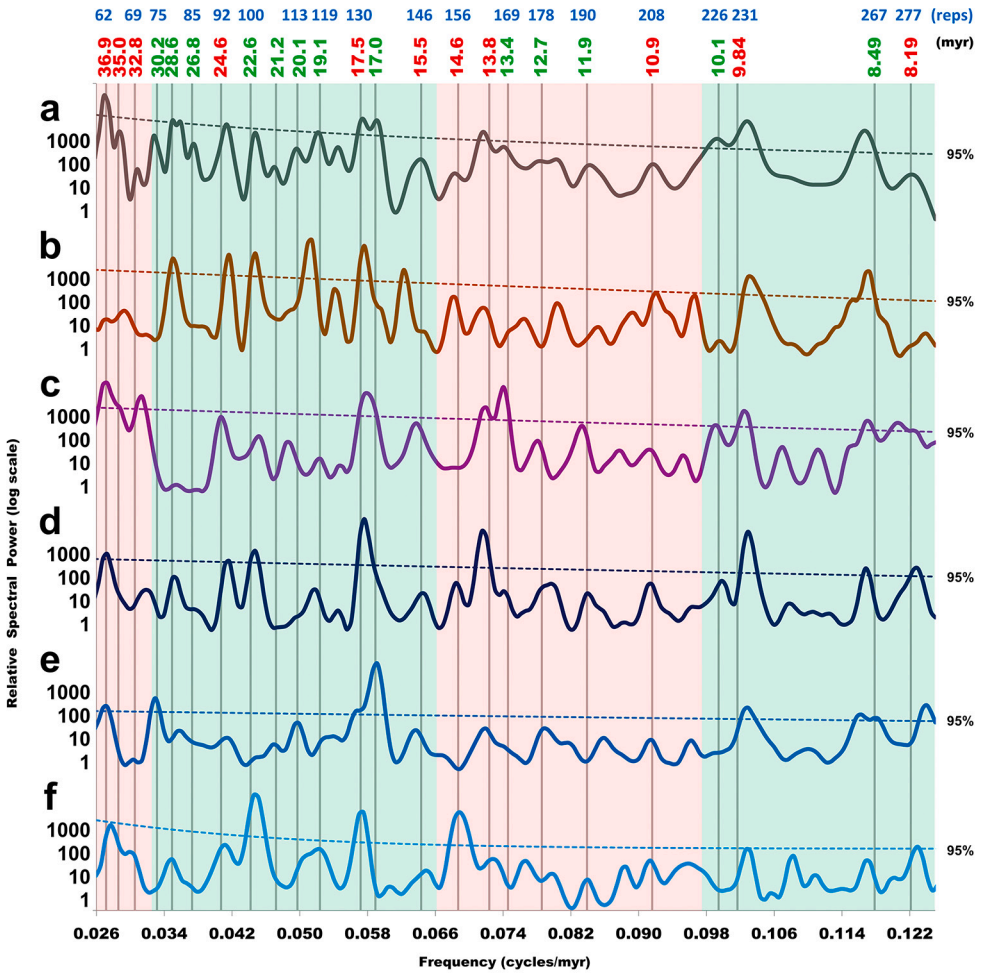

Fig. 19. Maximum mean correlation and periodograms. Medium-high frequency tests for the interval 2270–0 *Ma*, testing periodicity in the 8–39 myr range. The number of cyclic repetitions in the top row correspond to the sinusoidal models being tested in the second row. Log scale power spectra: (gray) maximum mean correlations from correlograms, and periodograms for (brown) Puetz-2019-DB, (purple) Puetz-2021-DB, (dark blue) Combined-DB, (medium blue) Dep-Modern-DB, and (light blue) Dep-200 *Ma*-DB. (For interpretation of the references to color in this figure legend, the reader is referred to the web version of this article.)

29c) over the 4000-myr test interval. Interestingly, although not necessarily significant, the igneous zircon time-series has a higher correlation ($\rho = 0.701$) with the model than the detrital zircon time-series ($\rho = 0.659$) used to develop the model. This suggests that the model is indeed a viable proxy of variation in global magmatic activity, which most researchers already assume.

The test of an indistinguishable relationship between igneous and detrital zircon age distributions continues with Model 2 (low frequency model) with time-series binned at 10-myr intervals for the 3400–0 *Ma* interval. Additionally, we explore a possible relationship with metamorphic activity use the age-distribution from zircon rims and investigate intervals of significant global glaciation. Cross-correlation analyses show the model is synchronous with the three U—Pb age distributions as follows: zircon rim ages ($\rho = 0.533$), igneous zircon ages ($\rho = 0.762$), and detrital zircon ages ($\rho = 0.822$) from which the model was developed. In this study, the ages are binned at 10-myr intervals. If one interprets zircon rim ages as times of metamorphic events, then this implies that on a global scale, metamorphism reaches maxima at about the same times as maxima in global magmatic production.

To explore a possible link between global climate variation and the model, Fig. 30 includes established periods of glaciation designated with vertical orange backgrounds. Further details regarding the certainty and extensiveness of these glaciations are discussed in numerous studies (Geboy et al., 2013; Young, 2018; Alvarenga et al., 2019; Chen et al., 2019). Other glacial periods likely exist; however, these are excluded because of poor dating and/or considerable disagreement about their legitimacy. A tentative interpretation is that extensive glacial periods coincide with (or slightly lag) times of magmatic minima. Magmatic minima and the associated glaciations might reflect periodicity in atmospheric chemistry, possibly linked to lower rates of emissions of greenhouse gases during minima and drawdowns of these gases during chemical weathering of uplifted rock (Edmond, 1992; Fang et al., 2019).

Precambrian evidence of a possible link between global magmatic activity and global climatic variation is primarily limited to analyses of glacial periods, although Nance (2021) postulates that $\delta^{18}O\ (‰)_{zircon}$ acts as a legitimate continuous proxy of Precambrian climate. Several proxies of Phanerozoic climate exist, which allows for time-series comparisons since 540 *Ma*. Boulila et al. (2018) use the Phanerozoic sea-level curve as a climate proxy and found evidence of 36-myr and 91-myr periodicity in sea levels. These cycles correspond reasonably well with two dominant cycles found in the detrital zircon – suggesting a correlation between felsic magmatism and global climate. The rationale for treating sea-level as a climate proxy rests on the assumption that as the global climate warms, glaciers melt and sea levels rise, whereas when the climate cools and glacial areas expand, sea levels fall. However, sea levels might also be affected by variation in the thickness of oceanic crust, mean ocean depth, seafloor spreading rates, and continental crust elevation during collisional phases. For these reasons, and because of significant inconsistencies among the various sea level curves and Phanerozoic $\delta^{18}O$ time-series, the study turns to periodicities found from Cenozoic climate proxies (Zachos et al., 2001) to investigate a possible link between magmatic production and global climate.

When binned at 100-kyr intervals, the $\delta^{18}O$ and $\delta^{13}C$ time-series generally contain enough samples per bin for the 35–0 *Ma* interval to assess periodicities in the 300 to 1400-kyr range. Of particular interest, do the periodicities from the 35–0 *Ma* climatic time-series (Fig. 31)

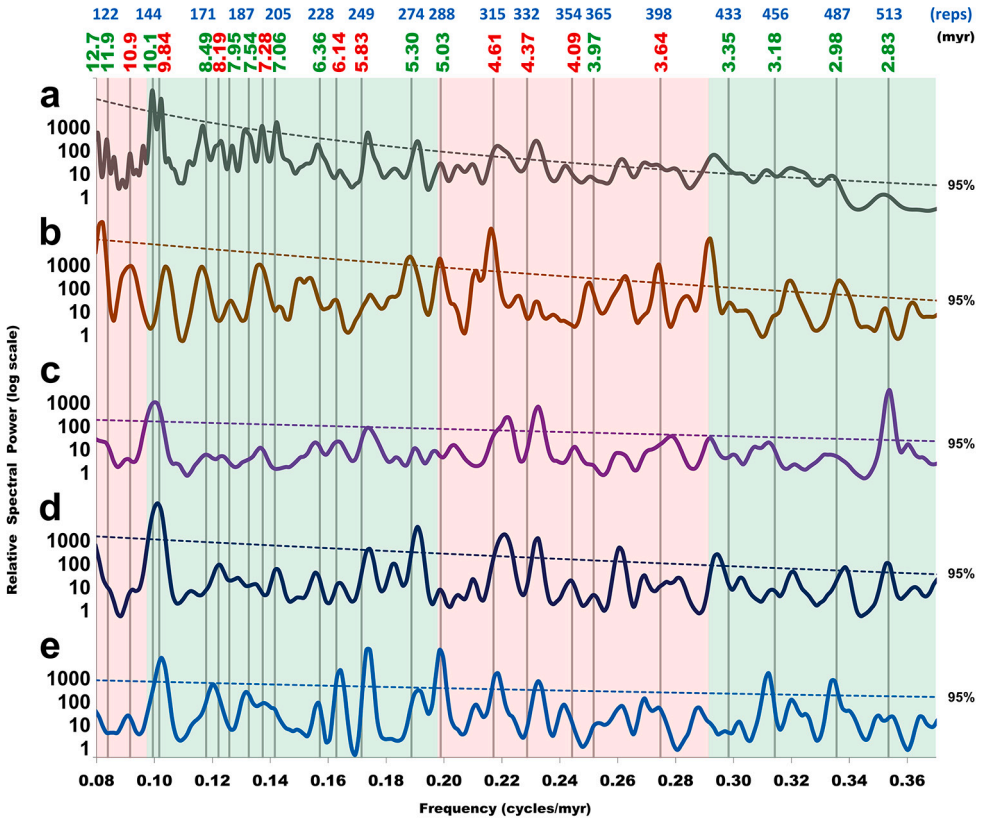

Fig. 20. Maximum mean correlation and periodograms. High frequency tests for the interval 1450–0 *Ma*, testing periodicity in the 2.7–12.5 myr range. The number of cyclic repetitions in the top row correspond to the sinusoidal models being tested in the second row. Refer to Fig. 19 for database color codes of log scale power spectra.

correspond to the 1118-kyr and 372.5-kyr cycles found from the primary period-tripling sequence found in detrital zircon age distributions (Fig. 22a)? In general, they do. The detrital zircon maximum mean correlation curve (Fig. 22a) has three strong periodicities clustered at 1152, 1118, and 1061-kyr. These same three periodicities are found from the climatic time-series. The $\delta^{18}O$ time-series shows a dominant peak within 1% of the 1118-kyr cycle and a smaller peak near 1061-kyr (Fig. 31a). Conversely, the $\delta^{13}C$ time-series shows a dominant peak within 1% of the 1152-kyr cycle and a smaller peak near 1061-kyr (Fig. 31b). In addition to several other harmonics, the $\delta^{18}O$ and $\delta^{13}C$ time-series both show marginal evidence of 373-kyr periodicity. The 31 and 94 cyclic repetitions (Fig. 31, top row) for the 1118 and 373-kyr cycles, respectively, are sufficiently large to provide reasonable estimates of the true periodicities.

If the primary period-tripling sequence extends to even higher frequencies, then one would expect periodicities of 124.2-kyr and 41.4-kyr in the climatic and detrital zircon time-series. A test of these cycles is currently not possible for detrital zircon. However, when binned at 10-kyr intervals, the $\delta^{18}O$ and $\delta^{13}C$ time-series generally contain enough samples per bin for the 14–0 *Ma* interval to assess periodicities in the 30 to 140-kyr range (Fig. 32). In this range, sedimentary sequences are often calibrated to the Milankovitch cycles, sometimes referred to as astro-tuning. The $\delta^{18}O$ and $\delta^{13}C$ time-series are calibrated to the GPTS-95 timescale (Zachos et al., 2001), which involves astro-tuning from 5.23–0 *Ma* and linear interpolation between tie-point from 14.01–5.23 *Ma*. For the 5.23–0 *Ma* interval, the periodograms from $\delta^{18}O$ (Fig. 32a) and $\delta^{13}C$ (Fig. 32b) both exhibit strong spectral peaks at the Milankovitch frequencies of ~95-kyr and 41-kyr. Conversely, for the 14.01–5.23 *Ma* interval, the periodograms from $\delta^{18}O$ (Fig. 32c) and $\delta^{13}C$ (Fig. 32d) both exhibit strong spectral peaks within 1% of 124.2-kyr – essential validating another cycle in the primary period-tripling sequence. They also show evidence of a ~ 41.4-kyr periodicity, but the spectral peaks are far weaker than those from the astro-tuned periodograms.

The stark difference between the calibrated cycles (Fig. 32a-32b) and the cycles from the unbiased time-series (Fig. 32c-32d) clearly illustrate the points that Aber (1997) addresses. A calibrated time-series does not and cannot validate its correctness. A time-series calibrated to a cyclical model only shows the expected variation if the model is valid. To test if the model is valid, one must always use data completely independent from the model (Aber, 1997; McDowall, 2004; Waters and Craw, 2006; Crisp et al., 2011). Thus, the periodograms from the unbiased time-series (Fig. 32c-32d) provide the only legitimate tests of the Milankovitch Theory. Indeed, the periodograms (Fig. 32c-32d) are supportive of the Milankovitch cyclicity, but less so than the calibrated time-series. In fact, the periodograms from the unbiased time-series are equally supportive of the primary period-tripling sequence listed in column 10 of Table 4. Specifically, the Milankovitch Theory postulates a 41-kyr obliquity cycle, whereas the primary period-tripling sequence postulates a 41.4-kyr volcanic-related cycle.

7. Correlation and causality

Research often focuses solely on primary causes, whereas here we explore possible primary, secondary, tertiary, etc. causes for the cascading events that leads to magmatic/zircon production. By assuming every event has a cause (Popper, 1963; Borchardt, 2007), then a 272-myr cyclic event, A, is assumed to be caused by factor B, which can be known or unknown. Then, the cause of B is assumed to have a cause C, and the cause of C is assumed to have a cause D, ad infinitum. Popper (1963) refers to this as *infinite regress*. When determining the cause(s) of any process, such as harmonic cycles, ultimately the question turns into a question of which cause. While the period-tripling harmonics indicate

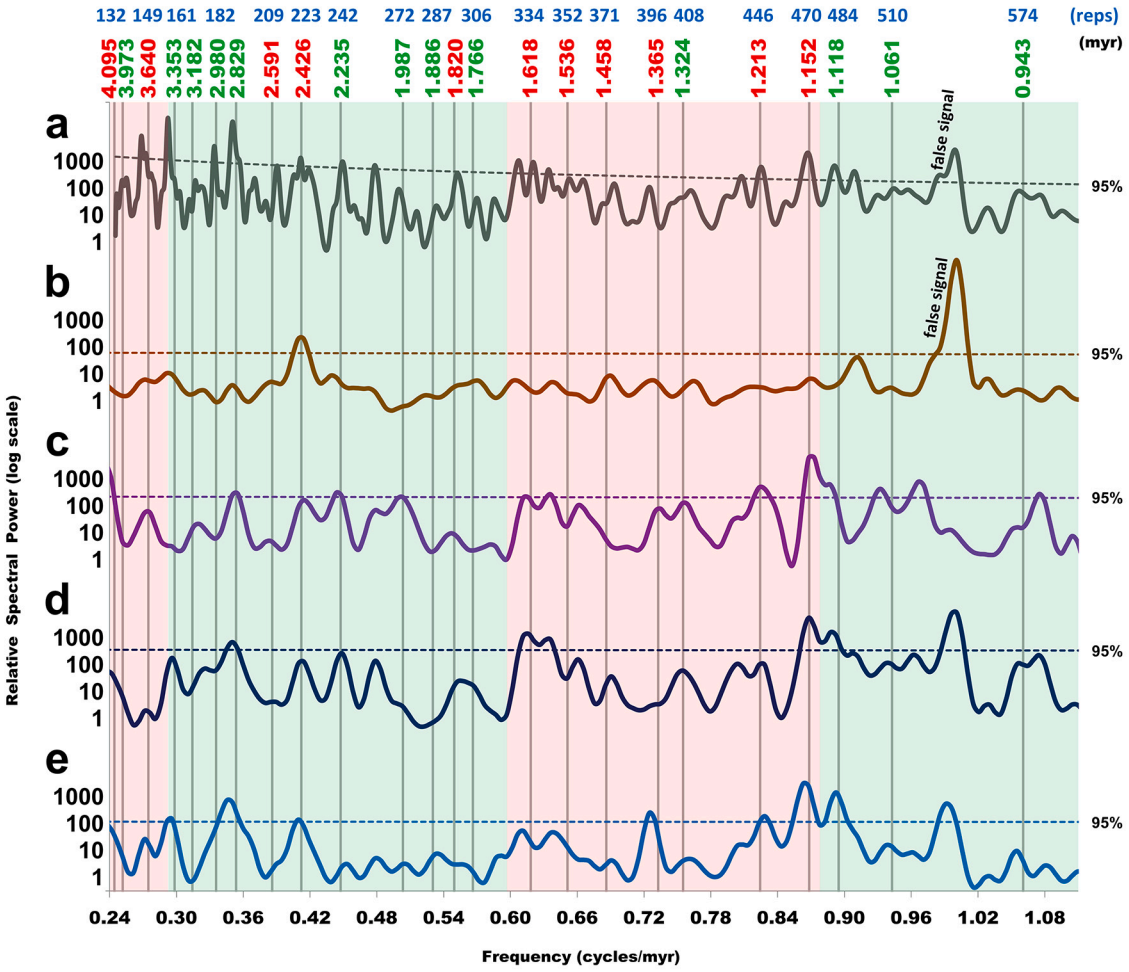

Fig. 21. Maximum mean correlation and periodograms. Ultra-high frequency tests for the interval 541–0 *Ma*, testing periodicity in the 0.9–4.2 myr range. The number of cyclic repetitions in the top row correspond to the sinusoidal models being tested in the second row. Log scale power spectra (gray) maximum mean correlations from correlograms, and periodograms for (brown) Puetz-2019-DB, (purple) Puetz-2021-DB, (dark blue) Combined-DB, and (medium blue) Dep-Modern-DB. (For interpretation of the references to color in this figure legend, the reader is referred to the web version of this article.)

a common cause, the harmonics do not logically imply the common cause is the direct cause of episodic zircon production. It might be that an indirect common cause best explains a chain of events that ultimately leads to episodic zircon production.

8. Hypothesized causes

Typically, scientific advancement leads to increased understanding of certain processes, which in turn raises new questions to replace those that are answered. This tendency is perhaps the ultimate signal of infinite regress (Popper, 1963). Regarding questions about the validity of the multitude of natural cycles discovered over the past century, most of them are likely valid but often within large ± uncertainties. Our analysis of detrital zircon periodicity (Section 4) shows strong-to-marginal evidence of at least 50 cycles with harmonic periodicities ranging from 300-kyr to 815-myr. Further rigorous testing with reliable independent data will eventually determine which of the detected cycles are indeed reproducible (Section 3.11), and thus, likely real.

Tests aimed to determine the capabilities of spectral analysis (Section 3.5) show that 4-digit precision is achievable when ages and signals are perfect, whereas precision shrinks to 3-digits when significant amounts of noise permeate a time-series for a well-sampled time-series containing more than 20 cyclic repetitions. Thus, we consider 3-digit periodicity as the maximum capability of spectral analysis. Even when these conditions are met, careless reporting and biased reporting have hampered research of periodic events. Careless reporting happens when a spectral peak is rounded to a nearby number ending in 0 or 5 – such as reporting a 97-myr spectral peak as 100-myr or a 39.2-myr spectral peak as 40-myr. Biased reporting happens when an unbiased isotopically dated time-series fails to show the expected periodicity, and then the radiometric ages are calibrated to conform to a certain theory (Section 3.8). Other reported cycles are questionable because the time-series only includes as few as 2 or 3 cyclic repetitions, where spectral analysis will certainly give an answer, but with considerable uncertainty associated with the estimate (Fig. 5).

Yet, the overriding concern of studies aimed to evaluate periodicity pertains to the reliability of the time-series themselves. Our analyses, and those of many others, focus on global explanations of causes. When this is the objective, care must be taken to ensure the measured time-series is indeed representative of global variation over time (Section 3.6). For instance, as a time-series extends further into the past, available samples typically diminish. In some instances, few or no samples are available for certain intervals of interest. When this happens, one must ask: Does the limited sampling density affect the global representativeness of the time-series? There is often no clear-cut answer, but a careful analysis is often required to determine the age for terminating a time-series that extends far into the past. For this reason, progressively shorter durations are most appropriate when investigating high

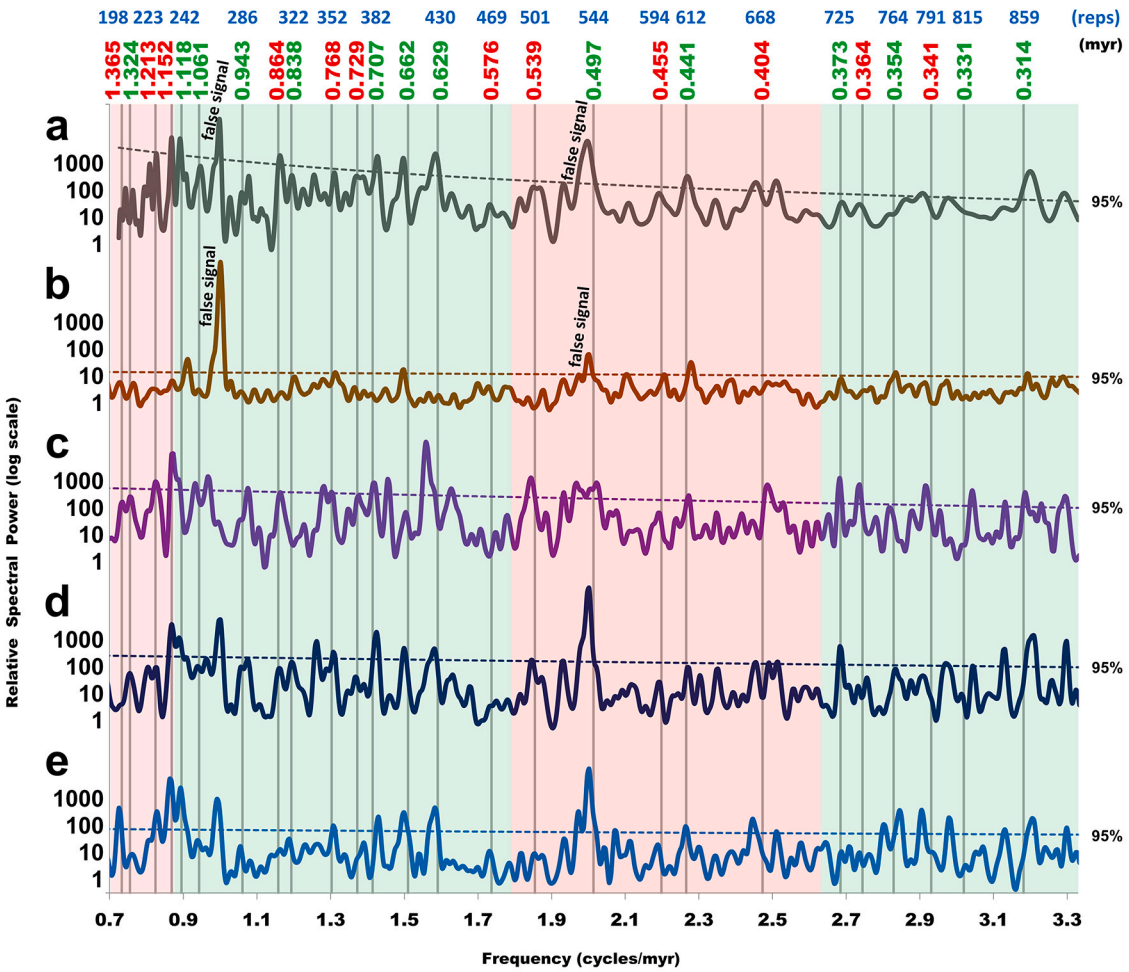

Fig. 22. Maximum mean correlation and periodograms. Ultra-high frequency tests for the interval 270–0 *Ma*, testing periodicity in the 0.3–1.4 myr range. The number of cyclic repetitions in the top row correspond to the sinusoidal models being tested in the second row. Refer to Fig. 21 for database color codes of log scale power spectra.

frequency cycles (Fig. 4).

With a keen awareness that existing hypotheses might have originated from poorly dated, poorly sampled, non-representative, and/or with limited cyclic repetitions in the time-series, we present a diverse list of hypotheses for explaining the cause of natural cycles. When one hypothesis contradicts another, it generally means at least one is incorrect. In other cases, seemingly different hypotheses might fit well together after linking them to a chain of events. We treat this array of postulated causes with tolerant skepticism (Lakatos, 1970, 1978) until it becomes possible to disprove those that are invalid.

It must be noted that Hopf bifurcation theory provides mathematical solutions for period-doubling systems (Ding et al., 2004; Mahboob et al., 2016) and period-tripling systems (Daumont et al., 1997; Bendiksen, 2004). Ding et al. (2004) provide a differential equation solution for an inertial shaker as a vibratory system, whereas Mahboob et al. (2016) developed an electromechanical resonator for Hopf period-doubling bifurcations when dissipation becomes negative. Hopf bifurcation theory focuses on mathematical models for simulating physical processes. Yet, even when a mathematical model accurately simulates a process, the simulation says little or nothing about the cause. In these experiments, the direct cause of the bifurcation harmonics was either a vibrator, shaker, resonator, or similar oscillator. Because bifurcation experiments produce period-doubling and period-tripling cycles with mechanical resonators, it might be safe to assume that some type of resonance causes the harmonic geological cycles. These harmonic related bifurcation experiments are equivalent to the laboratory experiments using fluids of variable viscosity to artificially generate plumes (LeBars and Davaille, 2004; Arndt and Davaille, 2013). It is often beneficial to turn to laboratory experiments to gain a better understanding of how physical processes operate that cannot be measured directly. For this reason, both bifurcation experiments and fluid viscosity experiments might provide meaningful guidance for understanding the cause of the observed geological cycles. As further explained in this section, ongoing research of correlations among planetary, solar, and/or galactic time-series should eventually determine if resonance within the galaxy, the Sun, Earth itself, or some other resonating factor causes the detected harmonic periodicities.

8.1. *Internal causes*

There has been considerable discussion about the causes of the low-frequency LIP and zircon events, with the most direct information coming from experimental and numerical modeling related to mantle plumes and to the supercontinent cycle. Low-frequency cycles are considered to be related to geodynamics and/or mantle cooling: (a) upstairs-related if caused by lithosphere or supercontinent events, and (b) downstairs-related if caused by deep mantle events (Condie et al., 2015, 2021). The lack of a close correspondence of low-frequency cycles to the supercontinent cycle and the fact that these cycles seem to begin long before we had supercontinents (Condie et al., 2015) is problematic

Table 4
Hypothetical green harmonics (myr units).

i\j	1	2	3	4	5	6	7	8	9	10
18	...	...	...	...	...	...	...	...	0.5587	**1.1175**
19	...	...	...	...	...	...	0.4191	**0.8381**	1.6762	**3.3525**
20	...	...	...	...	**0.3143**	**0.6286**	1.2572	2.5144	**5.0287**	**10.058**
21	...	...	...	0.4714	**0.9429**	**1.8858**	3.7716	**7.5431**	15.086	30.173
22	...	**0.3536**	**0.7072**	1.4143	**2.8287**	5.6573	11.315	**22.629**	45.259	**90.518**
23	0.5304	**1.0608**	2.1215	4.2430	**8.4860**	**16.972**	33.944	**67.888**	**135.78**	**271.55**
24	1.5911	**3.1823**	**6.3645**	**12.729**	25.458	**50.916**	101.83	**203.66**	407.33	**814.66**
25	4.7734	9.5468	**19.094**	38.187	**76.374**	152.75	305.50	610.99	...	...
26	14.320	**28.640**	**57.281**	114.56	**229.12**	458.24	916.49	...	...	...
27	42.961	**85.921**	**171.84**	343.68	687.37	...	...	...	...	...
28	128.88	257.76	**515.53**	...	...	...	...	...	...	...
29	386.64	773.29	...	...	...	...	...	...	...	...
i/j	**10**	**11**	**12**	**13**	**14**	**15**	**16**	**17**	**18**	**19**
12	...	...	...	...	...	...	...	...	0.3924	0.7849
13	...	...	...	...	...	...	...	0.5886	1.1773	2.3546
14	0.0138	...	...	...	...	**0.4415**	0.8830	**1.7659**	3.5319	**7.0637**
15	0.0414	...	...	**0.3311**	**0.6622**	**1.3244**	2.6489	**5.2978**	10.596	**21.191**
16	0.1242	...	**0.4967**	0.9933	**1.9867**	**3.9733**	**7.9467**	15.893	31.787	**63.573**
17	**0.3725**	0.7450	1.4900	**2.9800**	5.9600	**11.920**	23.840	47.680	95.360	190.72
18	**1.1175**	**2.2350**	4.4700	8.9400	17.880	35.760	**71.520**	143.04	286.08	572.16
19	**3.3525**	6.7050	**13.410**	**26.820**	**53.640**	107.28	214.56	**429.12**	858.24	...
20	**10.058**	**20.115**	40.230	**80.460**	**160.92**	321.84	643.68	...	...	...
21	30.173	60.345	120.69	**241.38**	482.76	965.52	...	...	...	...
22	**90.518**	181.04	362.07	724.14	...	...	...	...	...	...
23	**271.55**	543.11	...	...	...	...	...	...	...	...
24	**814.66**	...	...	...	...	...	...	...	...	...

Table 5
Hypothetical red harmonics (myr units).

i\j	1	2	3	4	5	6	7	8	9	10
17	...	...	...	...	...	...	...	...	0.3839	**0.7677**
18	...	...	...	...	...	...	...	**0.5758**	**1.1516**	2.3032
19	...	...	...	...	...	0.4318	**0.8637**	1.7274	3.4548	6.9095
20	...	...	...	0.3239	0.6478	1.2955	**2.5911**	5.1821	10.364	20.729
21	...	...	0.4858	0.9717	1.9433	3.8866	7.7732	**15.546**	31.093	62.186
22	**0.3644**	**0.7287**	**1.4575**	2.9150	**5.8299**	11.660	23.320	**46.639**	**93.279**	**186.56**
23	1.0931	2.1862	**4.3724**	8.7449	**17.490**	**34.980**	69.959	139.92	279.84	559.67
24	3.2793	6.5587	13.117	26.235	52.469	**104.94**	209.88	419.75	839.51	...
25	**9.8380**	19.676	39.352	78.704	157.41	**314.82**	629.63	...	...	...
26	29.514	59.028	**118.06**	236.11	472.22	944.45	...	...	...	...
27	88.542	177.08	**354.17**	708.33	...	...	...	...	...	...
28	265.63	531.25	...	...	...	...	...	...	...	...
29	796.88	...	...	...	...	...	...	...	...	...
i/j	**10**	**11**	**12**	**13**	**14**	**15**	**16**	**17**	**18**	**19**
11	...	...	...	...	...	...	...	...	...	**0.5392**
12	...	...	...	...	...	...	...	**0.4044**	0.8088	**1.6176**
13	...	...	...	...	...	0.3033	0.6066	**1.2132**	**2.4264**	4.8528
14	...	...	...	...	**0.4549**	0.9099	**1.8198**	**3.6396**	**7.2792**	**14.558**
15	...	...	**0.3412**	0.6824	**1.3648**	2.7297	5.4594	**10.919**	21.838	43.675
16	...	0.5118	1.0236	2.0473	**4.0945**	**8.1891**	16.378	**32.756**	65.513	131.03
17	**0.7677**	**1.5355**	3.0709	**6.1418**	12.284	**24.567**	49.134	98.269	196.54	**393.08**
18	2.3032	**4.6064**	9.2127	18.425	**36.851**	73.702	147.40	294.81	589.61	...
19	6.9095	**13.819**	27.638	55.276	**110.55**	221.10	442.21	884.42	...	...
20	20.729	**41.457**	82.914	165.83	331.66	663.31	...	...	...	...
21	62.186	124.37	248.74	497.49	994.97	...	...	...	...	...
22	**186.56**	373.11	746.23	...	...	...	...	...	...	...
23	559.67	...	...	...	...	...	...	...	...	...

for upstairs-related causes for these cycles. More likely, the supercontinent cycle adapted to already existing cycles of downstairs origin.

8.1.1. Deep mantle hypotheses

In recent years, the rapid evolution of numerical computing provides a means of simulating complex processes for convection with temperature-dependent viscosity, subduction, plume generation, and convection with compositional variation (Walzer and Hendel, 2008; Davaille and Limare, 2015). These studies are particularly important for 3-D time-dependent mantle flows with large variations in material properties. One approach of these models has been to study possible catastrophic overturns of the mantle. Davies (2008) was among the first to show that subduction of oceanic crust can lead to layering beneath the 660-km discontinuity, which in turn causes the upper mantle temperature to increase. This layering is postulated to break down every 100 to 150-myr, leading to mantle overturns that result in bursts of magmatism at Earth's surface. Periods of mantle plume generation may also lead to global episodes of enhanced magma production (Ogawa, 2007; Li et al., 2018). Mantle plumes are common features of thermal convection at high Rayleigh number and there is a good correlation between the shapes of LLSVPs at the base of the mantle and the time variation of core-mantle heat flux, which varies with periods of 100 to 200-myr (Li et al.,

Table 6
Periods (myr), weights (ρ), and peaks (*Ma*) for low frequency models.

1: Ultra-low freq. (Fig. 23)			2: Low freq. (Fig. 24)			3: Med-low freq. (Fig. 25)		
Period	Wt. (ρ)	Φ peak	Period	Wt. (ρ)	Φ peak	Period	Wt. (ρ)	Φ peak
814.7	0.487	265.35	814.7	0.302	265.35	314.8	0.205	247.00
515.5	0.257	53.98	515.5	0.300	53.98	271.6	0.214	265.35
429.1	0.071	169.40	393.1	0.287	245.95	241.4	0.123	62.00
393.1	0.155	245.95	314.8	0.304	247.00	186.6	0.259	75.50
314.8	0.178	247.00	271.6	0.288	265.35	171.8	0.322	111.05
271.6	0.162	265.35	241.4	0.174	62.00	160.9	0.150	111.00
241.4	0.119	62.00	229.1	0.134	60.95	135.8	0.270	255.00
229.1	0.108	60.95	203.7	0.104	10.86	110.6	0.147	104.00
203.7	0.043	10.86	186.6	0.225	75.50	104.9	0.169	85.66
186.6	0.129	75.50	171.8	0.190	111.05	90.52	0.175	265.35
171.8	0.089	111.05	160.9	0.087	111.00	85.92	0.127	8.91
...	...	...	135.8	0.146	255.00	80.46	0.114	18.24
...	...	...	110.6	0.092	104.00	76.37	0.166	21.35
...	...	...	104.9	0.082	85.66	71.52	0.094	27.38
...	...	...	90.52	0.072	265.35	67.89	0.085	23.21
...	...	...	85.92	0.079	8.91	53.64	0.068	39.37

Table 7
Periods (myr), weights (ρ), and peaks (*Ma*) for high frequency models.

4: Med-high freq. (Fig. 26)			5: High freq. (Fig. 27)			6: Ultra-low freq. (Fig. 28)		
Period	Wt. (ρ)	Φ peak	Period	Wt. (ρ)	Φ peak	Period	Wt. (ρ)	Φ peak
93.279	0.238	78.90	26.820	0.102	16.920	10.058	0.112	265.35
90.518	0.272	265.35	24.567	0.120	21.560	9.8380	0.113	3.714
85.921	0.272	8.91	20.115	0.124	15.290	8.1891	0.086	0.227
80.460	0.275	18.24	19.094	0.155	17.610	7.5431	0.078	4.100
76.374	0.293	21.35	17.490	0.122	4.440	7.0638	0.078	3.125
71.520	0.254	27.38	15.546	0.099	11.775	5.0287	0.079	2.024
67.888	0.087	23.21	14.558	0.180	0.649	3.9734	0.117	2.276
63.573	0.261	41.19	13.819	0.166	3.189	3.6396	0.107	2.739
53.640	0.245	39.37	13.410	0.194	2.807	3.3525	0.214	265.35
46.639	0.100	45.89	10.058	0.321	265.35	2.8287	0.153	2.903
36.851	0.193	1.71	9.8380	0.216	3.714	2.4264	0.143	1.108
34.980	0.085	11.63	8.4860	0.084	4.500	1.8858	0.120	0.347
28.640	0.115	14.62	8.1891	0.132	0.227	1.8198	0.136	0.833
26.820	0.118	16.92	7.0638	0.131	3.125	1.6176	0.152	0.606
24.567	0.103	21.56	5.0287	0.089	2.024	1.5355	0.151	0.971
17.490	0.085	4.44	4.0945	0.094	1.826	1.1516	0.190	1.140

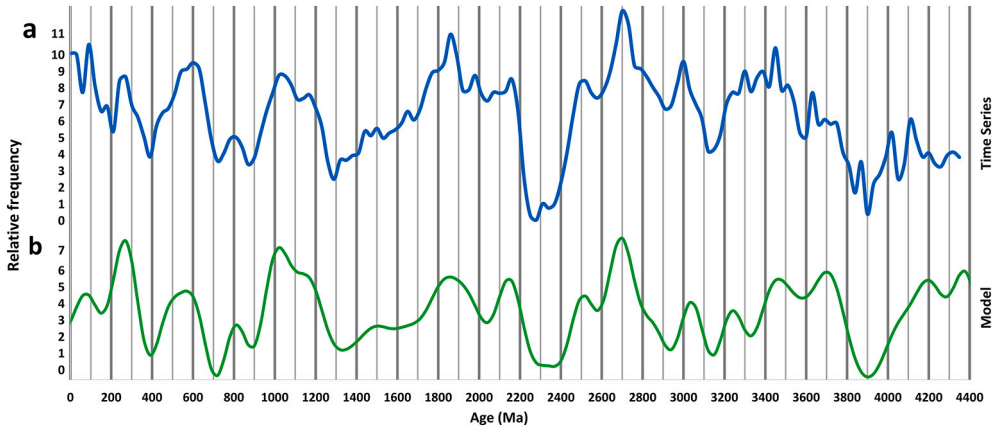

Fig. 23. U—Pb age distribution and the ultra-low frequency Model 1. Time-series for the interval 4350–0 *Ma*, binned at 30-myr intervals. Panels: (a) bandpass filtered U—Pb age distribution from Combined-DB, and (b) ultra-low frequency model. Correlation coefficient = 0.659.

2018). Plumes are transient and develop on characteristic time scales of 30 to 200-myr for mantle viscosities between 10^{19} and 10^{22} Pa s. However, their distribution in space and time is postulated to be chaotic, which implies other factors must also contribute to cyclical global LIP events. Previous studies have proposed that there may be two types of LIP events: (a) those associated with insulation or isolation of mantle beneath supercontinents (Gurnis, 1988; Coltice et al., 2007), and (b) those not associated with supercontinents but perhaps created by the return flow from slab avalanches from the Mantle Transition Zone (MTZ) (Koppers et al., 2021). Cheng (2018) suggests that magmatic heat transport contributes to terrestrial present-day heat loss as well as playing a key role in mantle cooling. Li et al. (2018) propose links among

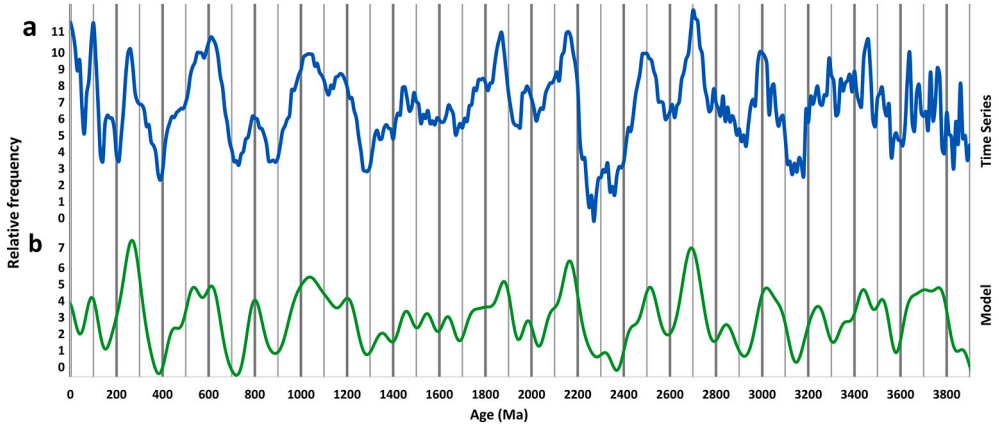

Fig. 24. U—Pb age distribution and the low frequency Model 2. Time-series for the interval 3900–0 *Ma*, binned at 10-myr intervals. Panels: (a) bandpass filtered U—Pb age distribution from Combined-DB, and (b) low frequency model. Correlation coefficient = 0.788.

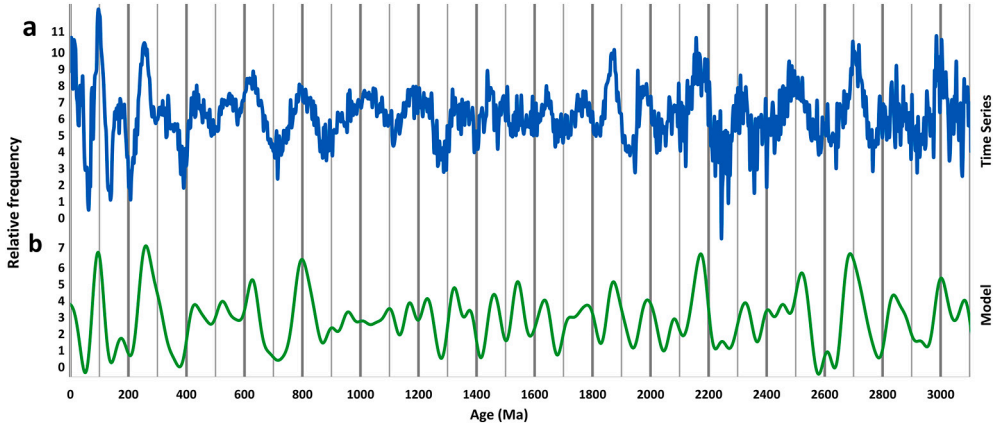

Fig. 25. U—Pb age distribution and the medium-low frequency Model 3. Time-series for the interval 3100–0 *Ma*, binned at 3-myr intervals. Panels: (a) bandpass filtered U—Pb age distribution from Combined-DB, and (b) medium-low frequency model. Correlation coefficient = 0.668.

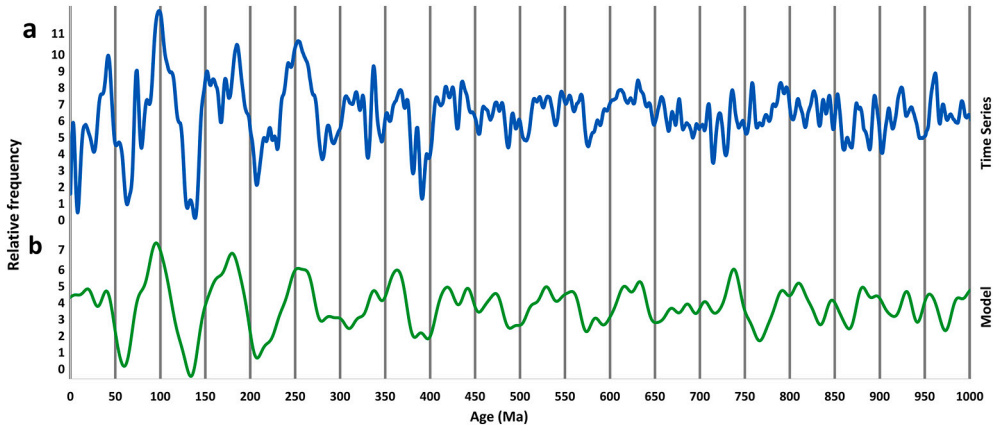

Fig. 26. U—Pb age distribution and the medium-high frequency Model 4. Time-series for the interval 1000–0 *Ma*, binned at 1-myr intervals. Panels: (a) bandpass filtered U—Pb age distribution from Combined-DB, and (b) medium-high frequency model. Correlation coefficient = 0.691.

the lowermost mantle structure, core-mantle boundary heat flux, and mantle plume formation. Additionally, recent spectral analysis studies of plume generation through time show that total plume heat flux increases with time and shows significant cyclicity, and that many of the same simulated cycles also appear in the detrital zircon age distribution (Li et al., in preparation).

Some of the most important results are from plumes generated in laboratory experiments using fluids of variable viscosity (LeBars and Davaille, 2004; Arndt and Davaille, 2013). As thermochemical plumes rise in these experiments, the plume material becomes denser and then sinks back to the bottom of the tank, whereby the whole process re-develops (LeBars and Davaille, 2004; Davaille and Limare, 2015). In these lab experimenters, several overturn episodes are observed but the later ones become progressively more disorganized. Plausible values for

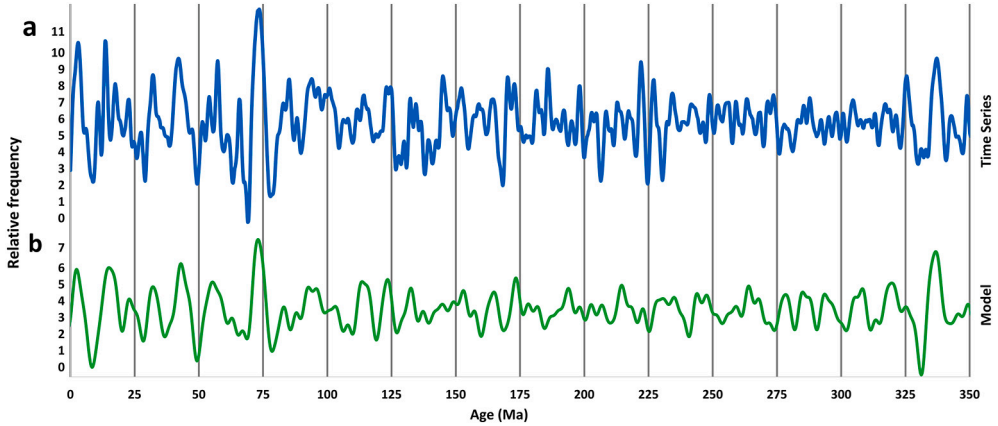

Fig. 27. U—Pb age distribution and the high frequency Model 5. Time-series for the interval 350–0 *Ma*, binned at 0.3-myr intervals. Panels: (a) bandpass filtered U—Pb age distribution from Combined-DB, and (b) high frequency model. Correlation coefficient = 0.619.

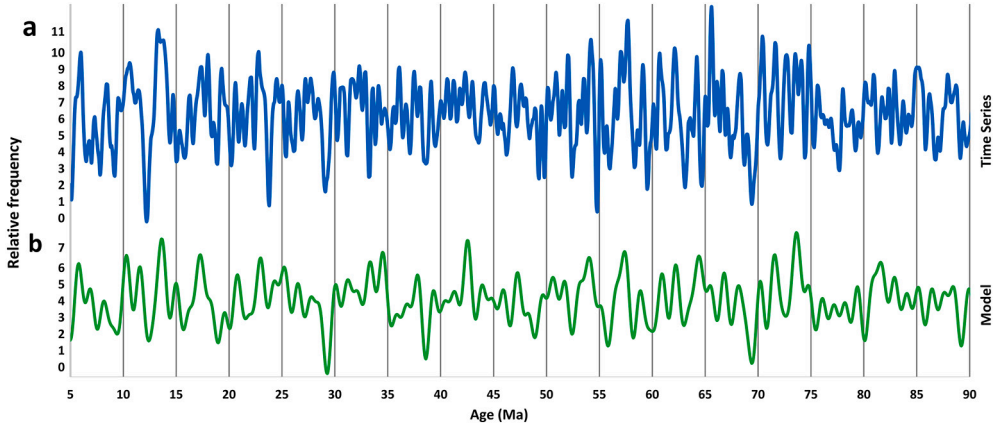

Fig. 28. U—Pb age distribution and the ultra-high frequency Model 6. Time-series for the interval 90–5 *Ma*, binned at 0.1-myr intervals. Panels: (a) bandpass filtered U—Pb age distribution from Combined-DB, and (b) ultra-high frequency model. Correlation coefficient = 0.515.

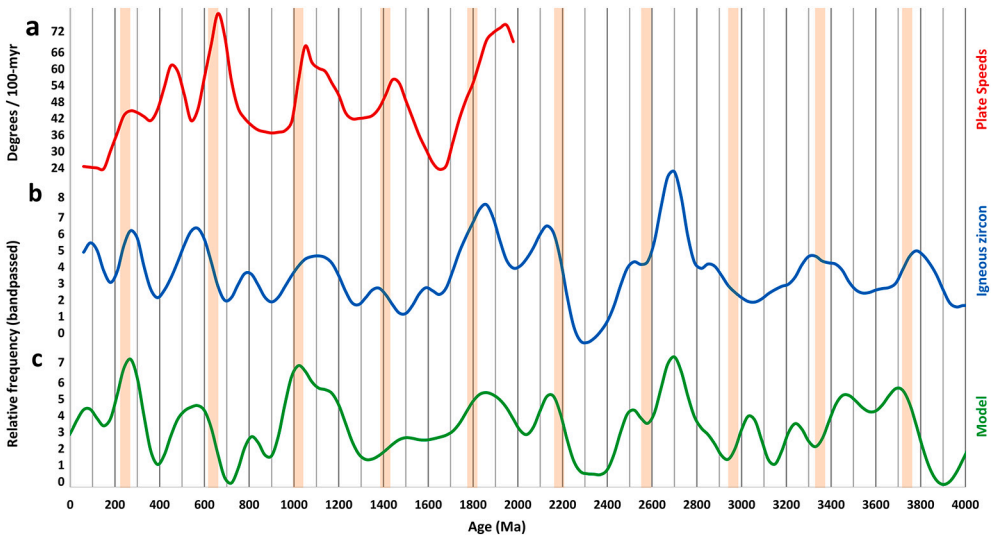

Fig. 29. Tests of Model 1 (ultra-low frequency). Comparison of geological time-series with Model 1 for the 4350–0 *Ma* interval. Light orange vertical backgrounds designate peaks of the 393.1-myr component of Model 1. Panels are: (a) plate speeds (Condie et al., 2021) lead the model by ~100-myr with a correlation of 0.337; (b) bandpass filtered U—Pb igneous zircon age distribution (Puetz and Condie, 2019) is synchronous with the model with a correlation of 0.701; and (c) ultra-low frequency Model 1 derived from the U—Pb detrital zircon age distribution from Combined-DB.

evolving mantle viscosity show that periodic plume generation would begin in the Hadean with immense volumes of hot material arriving at the top of the mantle. Results of numerical and experimental modeling studies show that global recurrence times of mantle overturn and/or plume events are on time scales of 100 to 200-myr, which is in good agreement with our observed age cycle in both LIP and zircon time series around 90.5-myr (Puetz and Condie, 2019). For an unknown reason, the related period-tripling components of 272 and 815-myr have larger amplitudes (likely related to amplitude modulation) and beginning at about 2 *Ga*, the supercontinent cycle developed in-phase with these low

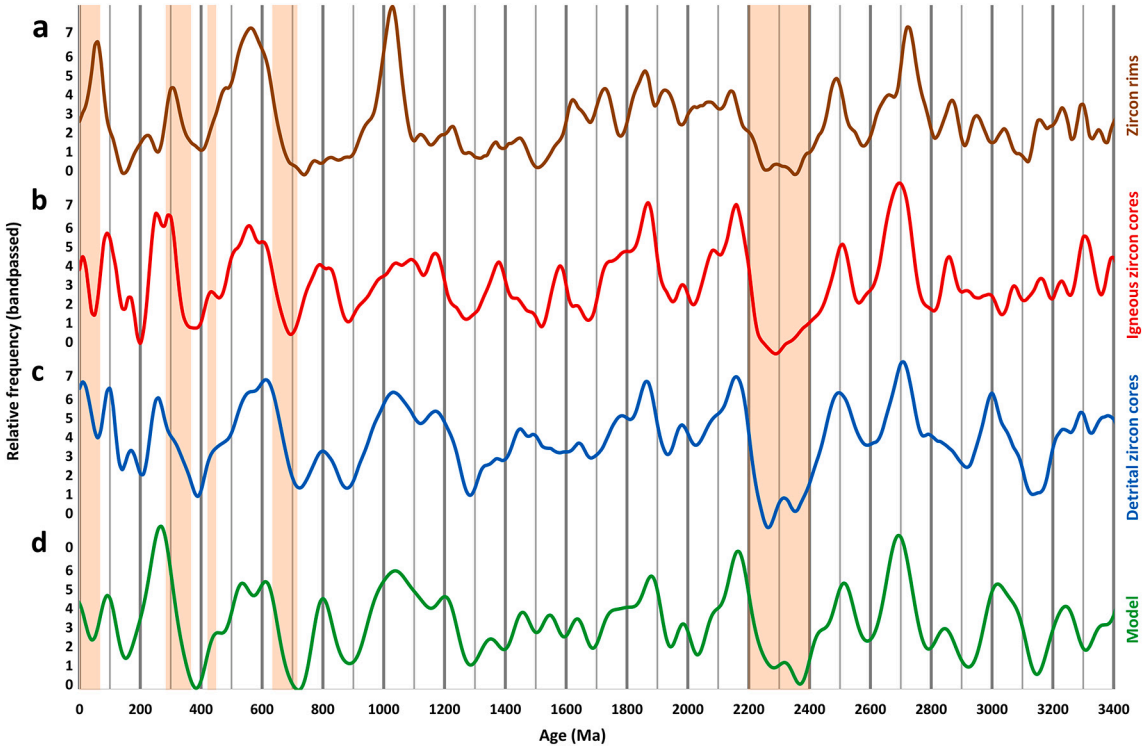

Fig. 30. Tests of Model 2 (low frequency). Comparisons of three geological time-series with Model 2 for the 3400–0 *Ma* interval. Light orange vertical backgrounds designate established periods of widespread glaciation. Panels are: (a) bandpass filtered U—Pb age-distribution from zircon rims (Puetz and Condie, 2019; Puetz et al., 2021) is synchronous with the model with a correlation of 0.533; (b) bandpass filtered U—Pb igneous zircon age distribution (Puetz and Condie, 2019) is synchronous with the model with a correlation of 0.762; (c) bandpass filtered U—Pb detrital zircon age distribution from the Combined-DB is synchronous with the model with a correlation of 0.822; and (d) low frequency Model 2 derived from the U—Pb detrital zircon age distribution in panel (c).

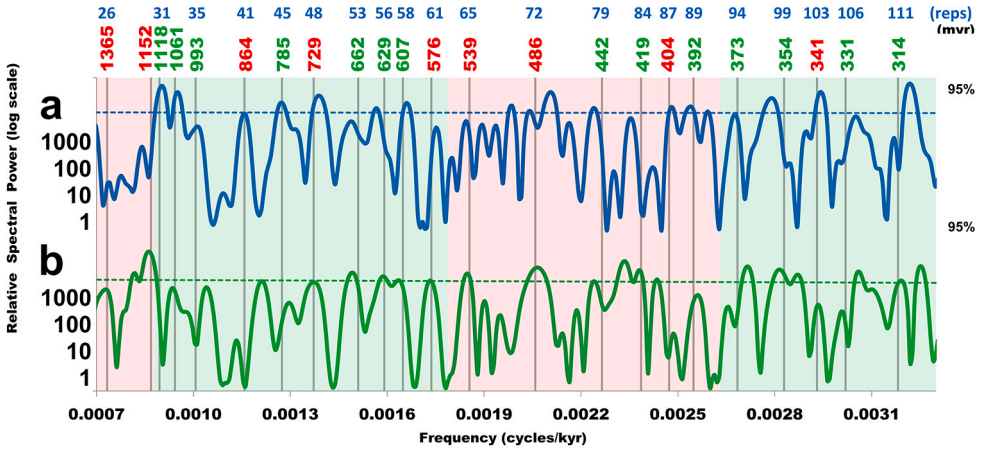

Fig. 31. Periodicities ranging from 300 to 1400 kyr in climate related time-series. Periodograms from climatic data (Zachos et al., 2001) for the interval 35–0 *Ma*, binned at 100-kyr increments. Periodograms are for: (a) $\delta^{18}O$, and (b) $\delta^{13}C$.

frequency cycles.

8.1.2. *Lithospheric-activated hypotheses*

Lithosphere-activated events are generally related to short-lived phenomena in the lithosphere or uppermost mantle. The most common models are those related to the sudden breakthrough of slabs stored in the MTZ resulting in slab avalanches (Machetel and Humler, 2003; Goes et al., 2017). When descending slabs reach the lower mantle, they initiate a mantle overturn or global plume event. Although lithosphere-activated events are generally related to plate tectonics, they may also operate in a stagnant lid regime if delaminated segments of the lithosphere collect in the MTZ. Numerical models by Davies (1995) have shown a range of possible behaviors in the upper mantle related to layering and that lithosphere-activated mantle overturns may have resulted in short-lived global magmatic-tectonic events.

8.2. *External causes*

We consider four hypotheses of external processes that might explain the periodicities found from detrital zircon age distributions: (a) periodic impact events, (b) cycles in the density of dark matter, (c) climate cycles as postulated by the Milankovitch Theory, and (d) harmonic

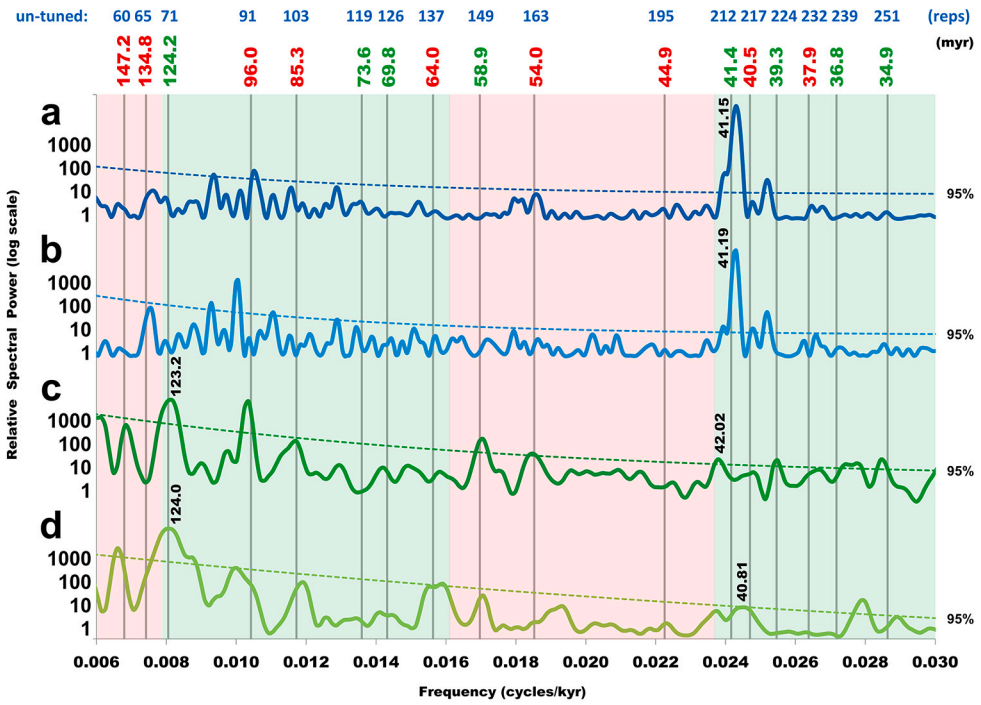

Fig. 32. Periodicities ranging from 30 to 140 kyr in climate related time-series. Periodograms from climate data (Zachos et al., 2001) for the interval 14–0 *Ma*, binned at 10-kyr increments. Periodograms are for the astro-tuned segment of the GPTS-95 timescale from 5.23–0 *Ma*, and for the untuned segment of the GPTS-95 timescale from 14.01–5.23 *Ma*: (a) $\delta^{18}O$ from the astro-tuned segment; (b) $\delta^{13}C$ from the astro-tuned segment; (c) $\delta^{18}O$ from the untuned segment; and (d) $\delta^{13}C$ from the untuned segment.

periodicities in solar activity.

8.2.1. Periodic asteroid/comet impacts

Richards et al. (2015) hypothesize that shock waves from the Chicxulub impact triggered the Deccan Traps, and Rampino (2015, 2018) further postulates that the Solar System's vertical oscillations through the Galactic disc periodically perturbs Oort Cloud comets. In turn, the hypothesized periodic impact events cause episodic geological and mass extinction events (Tiwari and Rao, 1998; Rampino (2015, 2018). One problem with the asteroid impact hypothesis is that modern Pacific-rim volcanism is unrelated to impact events. Thus, even though shock waves from asteroid impacts might contribute to isolated instances of increased magmatic activity, periodic impacts are unlikely to be the primary cause of periodic global magmatism.

8.2.2. Cycles in dark matter density

Some researchers postulate that dark matter within the Milky Way is unevenly distributed, with higher densities along the galactic disk and lower densities beyond (Randall and Reece, 2014; Rampino, 2015, 2018). As the Solar System oscillates through the galactic plane with a postulated 30-myr periodicity, Rampino (2015, 2018) postulates the variable density of dark matter periodically heats the terrestrial core/mantle, which causes regular pulses in mantle plumes and tectonic activity. Even though this could explain the ~30.2-myr periodicity in zircon production, it does not easily explain the other seven detected period-tripling components in the sequence from 815-myr to 0.373-myr.

8.2.3. Milankovitch climate cycles

A quarter century after Milankovitch (1941) introduced the hypothesis of external causes of periodic climate, Hays et al. (1976) propelled the obscure hypothesis into mainstream climatic research. The hypothesis states that predictable cycles in Earth's eccentricity, obliquity, and precession causes corresponding variation in the solar radiation reaching Earth, which in turn causes climate cycles. Kutterolf et al. (2013) further propose that the thickness of polar ice caps varies synchronously with the Milankovitch periodicities, which in turns causes periodic crustal stress that leads to volcanic episodes. However, the hypothesis of climate cycles causing volcanic cycles is questionable because many Phanerozoic intervals experienced considerable climate variation without evidence of polar ice caps (Sternai et al., 2020).

8.2.4. Solar activity harmonics

Some have suggested variation in solar activity causes volcanism on Earth (Stothers, 1989; Strestik, 2003). However, the evidence is far from conclusive. The concentrations of cosmic-ray radionuclides, such as ^{10}Be and ^{14}C, found in polar ice cores and tree rings (Vieira et al., 2011; Steinhilber et al., 2012) provide a means for reconstructing solar activity over many millennia. Using this approach, McCracken et al. (2013) found 15 significant periodicities ranging from 40 to 2320 years. Rather than corresponding to the primary period-tripling green harmonics found from detrital zircon ages, the solar cycles found by McCracken et al. (2013) closely correspond to four sets of period-doubling red harmonics, as defined by Eq. (5) using a timescale of years. The first set of hypothetical period-doubling cycles are $p_{8,13}$ (104-yr) and $p_{8,14}$ (208.0-yr Suess/De Vries cycle); the second set of cycles are $p_{11,5}$ (10.97-yr Schwabe cycle), $p_{11,6}$ (21.9-yr Hale polarity cycle), $p_{11,8}$ (87.76-yr Gleissberg cycle), $p_{11,10}$ (351.0-yr), and $p_{11,11}$ (702.1-yr); the third set of cycles are $p_{12,6}$ (65.82-yr), $p_{12,7}$ (131.6-yr), and $p_{12,9}$ (526.6-yr); and the fourth set of cycles are $p_{14,3}$ (74.05-yr) and $p_{14,4}$ (148.1-yr). McCracken et al. (2013) conclude that the stable natures of the Gleissberg cycle and the other related solar harmonics indicate a strong frequency control in the solar dynamo. Even though the detected solar harmonics correspond to the hypothetical red harmonics in the decadal to 1000-yr range, evidence to link solar cycles to possible volcanic/magmatic periodicities less than 1000 years is not yet available.

9. Testing hypotheses

While reviewing these divergent ideas of the cause of the episodic zircon production, we consider tests that can conclusively determine which hypotheses have merit and which should be eliminated from further consideration. Such tests are possible after the hypotheses are enhanced with sufficient details to make them falsifiable. As suggested by Popper (1963), the only legitimate test of a hypothesis is a rigorous attempt to disprove it. Research articles often list reasons for favoring a particular hypothesis. This is fine for developing a hypothesis, but

ultimately, the hypothesis must be tested with a legitimate attempt to disprove it. If the disproof attempt fails, the hypothesis is supported. Attempts to disprove a hypothesis are often achievable by first assuming a hypothesis is true, and then deducing what else must be true. Then, the resulting deductions might provide a means for falsifying inappropriate hypotheses.

9.1. Testing deep mantle hypotheses

A straightforward way to test if mantle events might cause low-frequency geological cycles is to compare results of both laboratory and numerical models with observed zircon periodicities. If they agree, then global mantle events remain viable as a cause. Conversely, if the results disagree, then hypotheses of episodic global mantle events can be eliminated from consideration. Currently, geodynamic models are not yet developed to a stage for rigorous comparisons because laboratory and numerical models tend to produce quasi-period cycles rather than robust periodicities. Testing if the supercontinent cycle causes low-frequency terrestrial cycles has been challenging. Importantly, the supercontinent cycle appears to be speeding up with time, and hence should not be considered as a fixed cycle. To determine if the supercontinent cycle is the primary cause of a given geological cycle requires careful comparisons with igneous and detrital zircon age distributions. One way to falsify this relationship is if a given cycle begins before the supercontinent cycle is established around 2 *Ga*. For instance, the 815-Myr cycle is often related to the supercontinent cycle, but we now recognize that this cycle began by at least 4 *Ga* – long before the supercontinent cycle began and thus cannot be easily linked to the supercontinent cycle. However, it is still possible that when the supercontinent cycle began, it adapted to an already existing mantle cycle, such as the 815-myr cycle.

9.2. Testing lithosphere-activated hypotheses

An attempt to falsify lithosphere-activated cycles related to plate tectonics as the primary cause of detrital zircon periodicity rests on identifying when plate tectonics began. Many investigators favor ~3 *Ga* as the starting age of plate tectonics (Condie, 2016). However, based on evidence from global igneous and detrital zircon age distributions (Figs. 8, 9, 29, 30), the 272 and 815-myr cycles were operational back to at least 4 *Ga*. This extensive time-range essentially falsifies the lithosphere-activated hypothesis. Yet, if it can be shown that plate tectonics developed by ~4 *Ma*, then plate tectonics could again serve as a possible explanation. Another problem that we know little about is whether postulated lithosphere-activated cycles could operate in a stagnant lid planetary regime. If they can, then it would seem likely that the periodicities would change when plate tectonics began.

9.3. Testing periodic asteroid/comet impacts

On Earth, virtually all evidence of asteroid impacts of all sizes has been erased by continual subduction, erosion, volcanic resurfacing, and/or orogenesis. Thus, direct tests of a global link between impact events and magmatic/volcanic cycle will never be possible. However, if we assume that the impact history on Earth mimics the impact histories on the Moon, Mars, Mercury, and Venus, as most planetary scientists already do (Wetherill, 1975; Mann, 2018), then indirect tests are possible. The ages of inner Solar System impacts are generally estimated by crater counting methods, and these ages predominantly range from 3.7 to 4.1 *Ga* (Supplement S2). Planetary scientists refer to this interval as the Late Heavy Bombardment (Wetherill, 1975; Mann, 2018). In addition to ages estimated from crater counting, some lunar craters are isotopically dated from rocks collected during the Apollo missions (Turner et al., 1973; Tera et al., 1973; Wetherill, 1975). Both methods produce similar ages, with crater counting errors typically estimated as ±100-myr for ages older than 3.4 *Ga*. Because isotopically dated lunar rocks and ejecta from the Apollo missions are predominantly older than 3.4 *Ga*, it is not yet possible to reliably calibrate crater counting models for ages younger than 3.4 *Ga*, which is the major limitation of the crater counting method.

Nonetheless, plans are in progress to resolve this. Like the Sheepbed mudstone in the Gale Crater on Mars, which was dated with a mass spectrometer onboard the Curiosity Rover (Farley et al., 2014), NASA has commissioned several studies to date impact craters and surface ages on the Moon, Mars, and small bodies such as Vesta via in situ geochronology from onboard instrumentation (Cohen et al., 2021). Until then, hypotheses related to Inner Solar System impact histories should all be treated tentatively until a sufficiently large sample of impact events, with ages younger than 3.4 *Ga*, can be isotopically dated. This will provide a means for enhanced calibration of crater counting chronologies. This could happen within the next decade, and thus provide a means for testing the various hypothesis of Inner Solar System impact histories.

9.4. Testing cycles in dark matter density

If the density of dark matter within the Solar System varies with regular periodicity, then the effects should be detectable from cosmological objects other than Earth. For instance, star formation might be correspondingly cyclic, the Inner Solar System planetoids should have magmatic periodicities like those on Earth, and solar cycles should also correspond accordingly. If peaks in the ages of star formations and peaks in Lunar, Martian, and Mercurian surface ages are found to differ from detrital zircon maxima on Earth, then it would seem appropriate to reject the dark matter hypothesis. Thus, the dark matter hypothesis might be relatively easy to disprove if it is false. The main problems with analyzing star formation cycles and the resurfacing history of the Moon, Mars, and Mercury are the large uncertainties associated with these ages. Inner Solar System resurfacing ages younger than 3.4 *Ga* have uncertainties as large as 0.5-gyr (Section 9.3), whereas the ages of Solar region stars are 3 to 6 times larger. Over the past decade, methods for dating nearby stars have decreased from approximately ±3-gyr (Nordstrom et al., 2004; Holmberg et al., 2009; Casagrande et al., 2011) to ±1.5-gyr more recently (Sanders and Das, 2018; Lu et al., 2021).

Even with newer satellites equipped with technologies to measure stellar parallax as much as 10 times more accurately than a decade ago, the ages of solar regions stars remain too large to assess if star formation is episodic, and if so, what those periodicities might be. Spectral analysis of bandpass filtered time-series of solar regions stars (Nordstrom et al., 2004; Holmberg et al., 2009; Casagrande et al., 2011; Sanders and Das, 2018; Lu et al., 2021) yields different dominant periodicities ranging from ~600-myr to 1400-myr. Thus, when the bandpass filtered star formation time-series (Figs. 33e-33g) are compared to the 815-myr model (Fig. 33h), they have inconsistent alignments. The inconsistent ages could be a consequence of each study employing a different method for estimating ages. Until astronomers reach a consensus on the optimal dating method, and until the age error are reduced to less than ~300-myr, evaluating possible periodicities in Solar region star formation seems untenable for testing a dark matter hypothesis. Thus, the best approach for testing if potential periodicities in dark matter density cause Inner Solar System magmatism rests on isotopically dating young impact craters on the Moon, Mars, and Mercury to constrain their cratering chronologies (Section 9.3).

9.5. Testing Milankovitch climate cycles

Considerable evidence from ocean core sediments moderately supports climatic periodicities linked to Earth's eccentricity, obliquity, and precession (Milankovitch, 1941; Hays et al., 1976). However, there are few, if any, legitimate published attempts to falsify the Milankovitch hypothesis. To do so requires dating sedimentary sequences so that all ages are isotopically calibrated by a method independent of a

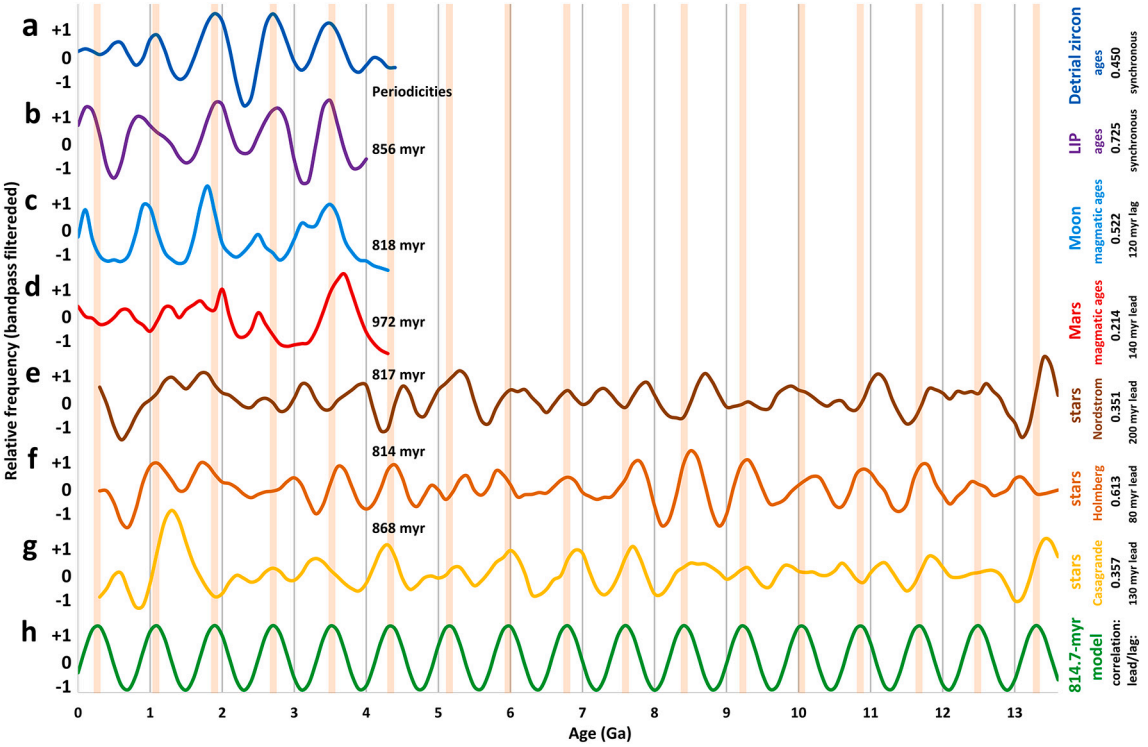

Fig. 33. External tests of 815-myr periodicity. Bandpass filtered time-series of detrital zircon, large igneous provinces ages, inner Solar System magmatic ages, star formations, and an 811.8-myr model. Periodicities from spectral analysis are in the left-center and correlations and lead/lag times along the right. Panels are: (a) detrital zircon age from the Combined-DB; (b) LIP age distribution (Condie et al., 2021); (c) Lunar resurfacing ages (Supplement S3); (d) Martian resurfacing ages (Supplement S4); (e) solar-region star formation ages (Nordstrom et al., 2004); (f) solar-region star formation ages (Holmberg et al., 2009); and (g) solar-region star formation ages (Casagrande et al., 2011); and (h) 815-myr model.

Milankovitch model. Specific examples include avoiding calibrating sedimentary ages to the Milankovitch model of Laskar et al. (1993) or to the LR04-stack of Lisiecki and Raymo (2005). The Milankovitch hypothesis might have merit. However, its validity will only become known from tests using data with independent ages. It will be important for different research teams to independently determine if the observed climatic cycles are best explained by the Milankovitch hypothesis or the hypothetical volcanic/magmatic related period-tripling sequence of 41.4, 124.2, 372.5, and 1118-kyr (Table 4, column j = 10). It could be that episodic volcanic/magmatic activity causes the climate cycles rather than Earth's eccentricity, obliquity, and precession.

9.6. *Testing periodic solar activity*

Because methods for detecting solar activity are currently limited to the Holocene or slightly beyond, it is difficult to rigorously test for a possible link between solar activity and terrestrial magmatic episodes. Yet, as the research community finds ways to accurately date and measure concentrations of cosmic-ray radionuclides, such as ^{10}Be in ice cores and ^{14}C in tree rings (Vieira et al., 2011; Steinhilber et al., 2012), and extend them further into the past, then it should be possible to test the solar-magmatic link hypothesis. However, the short half-lives of these isotopes preclude extending them more than about five half-lives into the past. Because ice cores contain both ^{10}Be and volcanic sulfate emissions discharged into the atmosphere from explosive eruptions (Cole-Dai et al., 2021), it should be possible to determine if ^{10}Be concentrations and volcanic sulfate concentrations vary synchronously. If so, the synchronicity would conclusively demonstrate a solar-magmatic link. Conversely, the absence of a correlation would falsify the solar-magmatic link hypothesis.

10. Conclusion

This work reviews numerous approaches for detecting periodicity found from natural processes. Our assessment is that spectral analysis provides 3-digit accuracy of periodicity for a reliable time-series containing a sufficiently large number of cyclic repetitions (generally >10, but preferably >20). Because we focus on the global U—Pb detrital zircon age distribution and similar global data, in this context a time-series is reliable if it is globally representative of the studied property. Six frequency-bound models are developed to simulate the global U—Pb detrital zircon age distribution.

The reproducible periodicities found from the global detrital zircon age distributions are often like those observed in related processes as well as seemingly unrelated processes. The similar periodicities and correlations suggest a complex chain of related events cause the numerous cycles reported in research. Several hypotheses have been developed to explain what causes the terrestrial cycles, and in some cases, the conjectures might be contradictory. With tolerant skepticism, we focus on possible internal causes as well as external causes. The degree to which each hypothesis is favored (Section 8) is often linked to the academic discipline to which a research team is devoted to. Rigorous attempts to test the various hypotheses will likely require increased collaboration among sedimentologists, climatologists, Precambrian specialists, planetary scientists, solar physicists, astronomers, and astrophysicists. As these multidisciplinary studies begin yielding results, the research community should be able to move forward with terrestrial evolution hypotheses supported from a diverse set of studies.

Even though the causes for the detected harmonics remain unknown, we hope this research sparks enough interest in these topics to ultimately find reliable answers for the cause(s). In all sciences, observations typically preceded explanations, something by many years. For instance, Newton devised an equation to predict gravitational processes

nearly 350 years ago, yet physicists remain contentious and continue to debate the cause of gravitation. Thus, it might require considerable research and time before viable explanations are found for the detected harmonics.

Declaration of Competing Interest

This research did not receive any specific grant from funding agencies in the public, commercial, or not-for-profit sectors.

Acknowledgements

The authors thank Peter Voice and Mike Rampino for constructive suggestions, which improved the manuscript. This research did not receive any specific grant from funding agencies in the public, commercial, or not-for-profit sectors.

Appendix A. Supplementary data

Supplementary data to this article can be found online at https://doi.org/10.1016/j.earscirev.2021.103885.

References

Aber, J.D., 1997. Why don't we believe the models? Bull. Ecol. Soc. Am. 78, 232–233. http://www.jstor.org/stable/20168170.

Alvarenga, C.J.S., Oliveira, G.D., Vieira, L.C., Santos, R.V., Baptista, M.C., Dantas, E.L., 2019. Carbonate chemostratigraphy of the Vazante Group, Brazil: a probable Tonian age. Precambrian Res. 331, 105378 https://doi.org/10.1016/j.precamres.2019.105378.

Arndt, N., Davaille, A., 2013. Episodic earth evolution. Tectonophysics 609, 661–674. https://doi.org/10.1016/j.tecto.2013.07.002.

Babaud, J., Witkin, A.P., Baudin, M., Duda, R.O., 1986. Uniqueness of the Gaussian Kernel for scale-space filtering. IEEE Trans. Pattern Anal. Mach. Intell. PAMI-8 26–33. https://doi.org/10.1109/TPAMI.1986.4767749.

Belozerov, V.B., Ivanov, I.A., 2003. Platform deposition in the West Siberian plate: a kinematic model. Geologiya/Geofizika 44 (8), 781–795.

Bendiksen, O.O., 2004. Nonlinear mode interactions and period-tripling flutter in transonic flow. J. Fluids Struct. 19, 591–606. https://doi.org/10.1016/j.jfluidstructs.2004.01.005.

Berggren, W.A., Kent, D.V., Aubry, M.P., Hardenbol, J., 1995. Geochronology, time scales and global stratigraphic correlation. SEPM Soc. Sediment. Geol. 54 https://doi.org/10.2110/pec.95.04.

Borchardt, G., 2007. The Scientific Worldview: Beyond Newton and Einstein. iUniverse, Lincoln, Nebraska.

Boulila, S., Laskar, J., Haq, B.U., Galbrun, B., Hara, N., 2018. Long-term cyclicities in Phanerozoic Sea-level sedimentary record and their potential drivers. Glob. Planet. Chang. 165, 128–136. https://doi.org/10.1016/j.gloplacha.2018.03.004.

Box, G.E.P., Jenkins, G.M., Reinsel, G.C., Ljung, G.M., 2016. Time Series Analysis: Forecasting and Control, 5th edition. John Wiley & Sons. Inc.

Casagrande, L., Schoenrich, R., Asplund, M., Cassisi, S., Ramirez, I., Melendez, J., Bensby, T., Feltzing, S., 2011. New constraints on the chemical evolution of the solar neighbourhood and Galactic disc(s). Astron. Astrophys. 530, A138. https://doi.org/10.1051/0004-6361/201016276.

Cawood, P.A., Hawkesworth, C.J., Dhuime, B., 2013. The continental record and the generation of continental crust. Geol. Soc. Am. Bull. 125, 14–32. https://doi.org/10.1130/B30722.1.

Chatfield, C., 2004. The Analysis of Time Series: An Introduction, sixth ed. Chapman and Hall, CRC Press, Boca Raton, Florida.

Chen, G., Cheng, Q., 2018. Cyclicity and Persistence of earth's evolution over time: wavelet and fractal analysis. Geophys. Res. Lett. 45, 8223–8230. https://doi.org/10.1029/2018gl078625.

Chen, T., Chen, W., Li, Q., Santosh, M., Li, J., 2019. Discovery of the Huronian Glaciation Event in China: evidence from glacigenic diamictites in the Hutuo Group in Wutai Shan. Precambrian Res. 320, 1–12. https://doi.org/10.1016/j.precamres.2018.10.009.

Cheng, Q., 2018. Extrapolations of secular trends in magmatic intensity and mantle cooling: Implications for future evolution of plate tectonics. Gondwana Res. 63, 268–273. https://doi.org/10.1016/j.gr.2018.08.001.

Cohen, B.A., Young, K.E., Zellner, N.E.B., Zacny, K., Yingst, R.A., Warwick, R., et al., 2021. In Situ Geochronology for the Next Decade. In: 52nd Lunar and Planetary Science Conference 2021, contribution number 2548.

Cole-Dai, J., Ferris, D.G., Kennedy, J.A., Sigl, M., McConnell, J.R., Fudge, T.J., et al., 2021. Comprehensive record of volcanic eruptions in the Holocene (11,000 years) from the WAIS divide, Antarctica ice core. J. Geophys. Res.-Atmos. 126, e2020JD032855 https://doi.org/10.1029/2020JD032855.

Coltice, N., Phillips, B.R., Bertrand, H., Ricard, Y., Rey, P., 2007. Global warming of the mantle at the origin of flood basalts over supercontinents. Geology 35, 391–394. https://doi.org/10.1130/G23240A.1.

Condie, K.C., 1998. Episodic continental growth and supercontinents: a mantle avalanche connection? Earth Planet. Sci. Lett. 163, 97–108. https://doi.org/10.1016/S0012-821X(98)00178-2.

Condie, K.C., 2016. Earth as an Evolving Planetary System, third edition. Academic Press, London. https://doi.org/10.1016/B978-0-12-803689-1.00001-8. 418 pp.

Condie, K.C., Puetz, S.J., 2019. Time series analysis of mantle cycles Part II: the geologic record in zircons, large igneous provinces and mantle lithosphere. Geosci. Front. 10, 1327–1336. https://doi.org/10.1016/j.gsf.2019.03.005.

Condie, K.C., Davaille, A., Aster, R.C., Arndt, N., 2015. Upstairs-downstairs: supercontinents and large igneous provinces, are they related? Int. Geol. Rev. 57, 1341–1348. https://doi.org/10.1080/00206814.2014.963170.

Condie, K.C., Puetz, S.J., Davaille, A., 2018. Episodic Crustal Production before 2.7 Ga. Precambrian Res. 312, 16–22. https://doi.org/10.1016/j.precamres.2018.05.005.

Condie, K.C., Pisarevsky, S.A., Puetz, S.J., 2021. LIPs, orogens and supercontinents: the ongoing saga. Gondwana Res. 96, 105–121. https://doi.org/10.1016/j.gr.2021.05.002.

Crisp, M.D., Trewick, S.A., Cook, L.G., 2011. Hypothesis testing in biogeography. Trends Ecol. Evol. 26, 66–72. https://doi.org/10.1016/j.tree.2010.11.005.

Daumont, I., Kassner, K., Misbah, C., Valance, A., 1997. Cellular self-propulsion of two-dimensional dissipative structures and spatial-period tripling Hopf bifurcation. Phys. Rev. E 55, 6902. https://doi.org/10.1103/PhysRevE.55.6902.

Davaille, A., Limare, A., 2015. Laboratory studies of mantle convection. Treat. Geophys. 7, 89–165. https://doi.org/10.1016/B978-0-444-53802-4.00128-7.

Davies, G.F., 1995. Punctuated tectonic evolution of the earth. Earth Planet. Sci. Lett. 136, 363–379. https://doi.org/10.1016/0012-821X(95)00167-B.

Davies, G.F., 2008. Episodic layering of the early mantle by the basalt barrier mechanism. Earth Planet. Sci. Lett. 275, 382–392. https://doi.org/10.1016/j.epsl.2008.08.036.

Dhuime, B., Hawkesworth, C.J., Storey, C.D., Cawood, P.A., 2011. From sediments to their source rocks: Hf and Nd isotopes in recent river sediments. Geology 39, 407–410. https://doi.org/10.1130/G31785.1.

Ding, W.C., Xie, J.H., Sun, Q.G., 2004. Interaction of Hopf and period doubling bifurcations of a vibro-impact system. J. Sound Vib. 275, 27–45. https://doi.org/10.1016/S0022-460X(03)00740-5.

Dorman, F.H., 1968. Some Australian oxygen isotope temperatures and a theory for a 30-million-year world temperature cycle. J. Geol. 76, 297–313. https://www.jstor.org/stable/30069099.

Edmond, J.M., 1992. Himalayan tectonics, weathering processes, and the strontium isotope record in marine limestones. Science 258, 1594–1597. https://doi.org/10.1126/science.258.5088.1594.

Fang, X., Galy, A., Yang, Y., Zhang, W., Ye, C., Song, C., 2019. Paleogene global cooling–induced temperature feedback on chemical weathering, as recorded in the northern Tibetan Plateau. Geology 47, 992–996. https://doi.org/10.1130/G46422.1.

Farley, K.A., Malespin, C., Mahaffy, P., Grotzinger, J.P., Vasconcelos, P.M., Milliken, R.E., et al., 2014. In situ radiometric and exposure age dating of the martian surface. Science 343. https://doi.org/10.1126/science.1247166 article 1247166.

Geboy, N.J., Kaufman, A.J., Walker, R.J., Misi, A., de Olivier, T.F., Miller, K.E., 2013. Re-Os age constraints and new observations of Proterozoic glacial deposits in the Vazante Group, Brazil. Precambrian Res. 238, 199–213. https://doi.org/10.1016/j.precamres.2013.10.010.

Gehrels, G., Sundell, K., George, S., 2019. 2019 Short Course modules on U-Pb Geochronology of Detrital Zircons: Best Practices for U-Pb Data Acquisition, Reduction, Analysis, and Archiving. GSA 2019 Meeting, Sept 22–25; Phoenix, Arizona. https://sites.google.com/a/laserchron.org/laserchron/.

Georgiev, N., Froitzheim, N., Cherneva, Z., Frei, D., Grozdev, V., Jahn-Awe, S., Nagel, T. J., 2016. Structure and U-Pb zircon geochronology of an Alpine nappe stack telescoped by extensional detachment faulting (Kulidzhik area, Eastern Rhodopes, Bulgaria). Int. J. Earth Sci. 105, 1985e2012. https://doi.org/10.1007/s00531-016-1293-4.

Goes, S., Agrusta, R., van Hunen, J., Garel, F., 2017. Subduction-transition zone interaction: a review. Geosphere 13, 644–664. https://doi.org/10.1130/GES01476.1.

Grabau, A.W. (1940). The Rhythm of the Ages: Earth History in the Light of the Pulsation and Polar Control Theories. In: R.E. Krieger, Huntington, New York.

Gurnis, M., 1988. Large-scale mantle convection and the aggregation and dispersal of supercontinents. Nature 332, 695–699. https://doi.org/10.1038/332695a0.

Hardy, B.W., Jamieson, K.H., 2017. Chapter 42: Overcoming biases in processing of time series data about climate. In: Jamieson, K.H., Kahan, D.M., Scheufele, D.A. (Eds.), The Oxford Handbook of the Science of Science Communication. Oxford University Press.

Hawkesworth, C., Cawood, P., Kemp, T., Storey, C., Dhuime, B., 2009. A matter of preservation. Science 323, 49–50. https://doi.org/10.1126/science.1168549.

Hays, J.D., Imbrie, J., Shackleton, N.J., 1976. Variations in the Earth's orbit: Pacemaker of the ice ages. Science 194, 1121–1132. https://doi.org/10.1126/science.194.4270.1121.

Hilgen, F.J., Hinnov, L.A., Aziz, H.A., Abels, H.A., Batenburg, S., et al., 2015. Stratigraphic continuity and fragmentary sedimentation: the success of cyclostratigraphy as part of integrated stratigraphy. Geol. Soc. Lond. Spec. Publ. 404, 157–197. https://doi.org/10.1144/SP404.12.

Hinnov, L.A., 2000. New perspectives on orbitally forced stratigraphy. Annu. Rev. Earth Planet. Sci. 28, 419–475. https://doi.org/10.1146/annurev.earth.28.1.419.

Hinnov, L.A., 2005. Chapter 4: Earth's orbital parameters and cycle stratigraphy. In: Gradstein, F.M., Ogg, J.G., Smith, A. (Eds.), A Geologic Time Scale 2004. Cambridge University Press, NY.

Holmberg, J., Nordstrom, B., Andersen, J., 2009. The Geneva-Copenhagen survey of the Solar neighbourhood III. Improved distances, ages, and kinematics. Astron. Astrophys. 941–947. https://doi.org/10.1051/0004-6361/200811191.
Holmes, A., 1927. The Age of the Earth: An Introduction to Geological Ideas. Benn, London.
Ikeda, M., Tada, R., 2020. Reconstruction of the chaotic behavior of the Solar System from geologic records. Earth Planet. Sci. Lett. 537, 116168 https://doi.org/10.1016/j.epsl.2020.116168.
Ikeda, M., Ozaki, K., Legrand, J., 2020. Impact of 10-Myr scale monsoon dynamics on Mesozoic climate and ecosystems. Sci. Rep. 10 https://doi.org/10.1038/s41598-020-68542-w.
Isley, A.E., Abbott, D.H., 2002. Implications for the temporal distribution of high-Mg magmas for mantle plume volcanism through time. J. Geol. 110, 141–158. https://doi.org/10.1086/338553.
Johnson, C.M., Van Kranendonk, M.J., 2019. In: Kolb, V.M. (Ed.), Ancient Life and Plate Tectonics. In: Handbook of Astrobiology. Taylor and Francis, Boca Raton. https://doi.org/10.1201/b22230.
Jorgensen, W.L., 2000. Perspective on: Equation of state calculations by fast computing machines. Theor. Chem. Accounts 103, 225–227. https://doi.org/10.1007/s002149900053.
Koppers, A.A.P., Becker, T.W., Jackson, M.G., Konrad, K., Müller, R.D., Romanowicz, B., 2021. Mantle plumes and their role in Earth processes. Nat. Rev. Earth Environ. 2, 382–401. https://doi.org/10.1038/s43017-021-00168-6.
Korenaga, J., 2006. Archean geodynamics and the thermal evolution of earth. In: Benn, K., Mareschal, J.C., Condie, K.C. (Eds.), Archean Geodynamics and Environments. American Geophysical Union, Washington, DC.
Kutterolf, S., Freundt, A., Perez, W., Morz, T., Schacht, U., Wehrmann, H., Schmincke, H.-U., 2008. The Pacific offshore record of Plinian arc volcanism in Central America, part 1: Along-arc correlations. Geochem. Geophys. Geosyst. 9, Q02S01 https://doi.org/10.1029/2007GC001631.
Kutterolf, S., Jegen, M., Mitrovica, J.X., Kwasnitschka, T., Freundt, A., Huybers, P.J., 2013. A detection of Milankovitch frequencies in global volcanic activity. Geology 41, 227–230. https://doi.org/10.1130/G33419.1.
Lakatos, I., Musgrave, A., 1970. Falsification and the Methodology of Scientific Research Programmes. In: Lakatos, I. (Ed.), Criticism and the Growth of Knowledge. Cambridge University Press.
Lakatos, I., 1978. In: Worrall, J., Currie, G. (Eds.), The Methodology of Scientific Research Programmes: Philosophical Papers, Vol. 1. Cambridge University Press.
Lancaster, P.J., Storey, C.D., Hawkesworth, C.J., Dhuime, B., 2011. Understanding the roles of crustal growth and preservation in the detrital zircon record. Earth Planet. Sci. Lett. 305, 405–412. https://doi.org/10.1016/j.epsl.2011.03.022.
Laskar, J., Joutel, F., Boudin, F., 1993. Orbital, precessional and insolation quantities for the Earth from 20 Myr to +10 Myr. Astron. Astrophys. 270, 522–533.
LeBars, M., Davaille, A., 2004. Whole-layer convection in an heterogeneous planetary mantle. J. Geophys. Res. 109 https://doi.org/10.1029/2003JB002617 article 2003JB002617.
Li, M., Zhong, S., Olson, P., 2018. Linking lowermost mantle structure, core-mantle boundary heat flux and mantle plume formation. Phys. Earth Planet. Inter. 277, 10–29. https://doi.org/10.1016/j.pepi.2018.01.010.
Li, M.; Puetz, S.; Condie, K.; Olson, P. (in preparation). The Periodicity of Mantle Plume Heat Flux in 3D Global Geodynamic Models and Its Implications for Growth of Continental Crust.
Lisiecki, L.E., Raymo, M.E., 2005. A Pliocene-Pleistocene stack of 57 globally distributed benthic d18O records. Paleoceanography 20, PA1003. https://doi.org/10.1029/2004PA001071.
Lo, C.P., Watson, L.J., 1998. The influence of geographic sampling methods on vegetation map accuracy evaluation in a swampy environment. Photogramm. Eng. Remote. Sens. 64, 1189–1200.
Lopez, C., Riquelme, R., Martinez, F., Sanchez, C., Mestre, A., 2018. Zircon U-Pb geochronology of the Mesozoic to lower Cenozoic rocks of the Coastal Cordillera in the Antofagasta region (22°30′-23°00′S): insights to the Andean tectonomagmatic evolution. J. S. Am. Earth Sci. 87, 113e138. https://doi.org/10.1016/j.jsames.2017.11.005.
Lu, Y., Angus, R., Curtis, J.L., David, T.J., Kiman, R., 2021. Gyro-Kinematic ages for around 30,000 Kepler Stars. Astron. J. 161 https://doi.org/10.3847/1538-3881/abe4d6 article-189.
Machetel, P., Humler, E., 2003. High mantle temperature during cretaceous avalanche. Earth Planet. Sci. Lett. 208, 125–133. https://doi.org/10.1016/S0012-821X(03)00041-4.
Mahboob, I., Dupuy, R., Nishiguchi, K., Fujiwara, A., Yamaguchi, H., 2016. Hopf and period-doubling bifurcations in an electromechanical resonator. Appl. Phys. Lett. 109, 073101 https://doi.org/10.1063/1.4960735.
Mann, A., 2018. Bashing holes in the tale of Earth's troubled youth. Nature 553, 393–395. https://doi.org/10.1038/d41586-018-01074-6.
MATLAB, 2021. Student's t Inverse Cumulative Distribution Function. Retrieved on July 7, 2021. https://www.mathworks.com/help/stats/tinv.html.
McCracken, K.G., Beer, J., Steinhilber, F., Abreu, J., 2013. A phenomenological study of the cosmic ray variations over the past 9400 years, and their implications regarding solar activity and the solar dynamo. Sol. Phys. 286, 609–627. https://doi.org/10.1007/s11207-013-0265-0.
McDowall, R.M., 2004. What biogeography is: a place for process. J. Biogeogr. 31, 345–351. https://doi.org/10.1046/j.0305-0270.2003.01020.x.
Metropolis, N., Rosenbluth, A.W., Rosenbluth, M.N., Teller, A.H., 1953. Equation of State Calculations by Fast Computing Machines. J. Chem. Phys. 21, 1087–1092. https://doi.org/10.1063/1.1699114.
Meyers, S.R., Peters, S.E., 2011. A 56 million year rhythm in north American sedimentation during the Phanerozoic. Earth Planet. Sci. Lett. 303 (2011), 174–180. https://doi.org/10.1016/j.epsl.2010.12.044.
Microsoft Excel T.INV, 2021. T.INV Function. Retrieved on July 7, 2021. https://support.microsoft.com/en-us/office/t-inv-function-2908272b-4e61-4942-9df9-a25fec9b0e2e.
Milankovitch, M., 1941. Kanon der Erdbestrahlungen und seine Anwendung auf das Eiszeiten Problem. Roy. Serb. Acad. Spec. Public. 133.
Mitchell, R.N., Spencer, C.J., Kirscher, U., He, X.F., Murphy, J.B., Li, Z.X., Collins, W.J., 2019. Harmonic hierarchy of mantle and lithospheric convective cycles: time series analysis of hafnium isotopes of zircon. Gondwana Res. 75, 239–248. https://doi.org/10.1016/j.gr.2019.06.003.
Mudelsee, M., 2003. Estimating Pearson's Correlation Coefficient with Bootstrap Confidence Interval from Serially Dependent Time Series. Math. Geol. 35, 651–665. https://doi.org/10.1023/b:matg.0000002982.52104.02.
Müller, R.D., Dutkiewicz, A., 2018. Oceanic crustal carbon cycle drives 26-million-year atmospheric carbon dioxide periodicities. Science. Advances 4, eaaq0500. https://doi.org/10.1126/sciadv.aaq0500.
Nance, R.D., 2021. The Supercontinent Cycle and Earth's Long-Term Climate. Geophysical Monograph Series. AGU Books.
Neeman, B.U., 1993. Orbital tuning of paleoclimatic records: a reassessment. Technical Report No. 39572. Lawrence Livermore National Laboratory.
Negi, J.G., Tiwari, R.K., 1983. Matching long term periodicities of geomagnetic reversals and galactic motions of the solar system. Geophys. Res. Lett. 10, 713–716. https://doi.org/10.1029/GL010i008p00713.
Nordstrom, B., Mayor, M., Andersen, J., Holmberg, J., Pont, F., Jorgensen, B.R., et al., 2004. The Geneva-Copenhagen survey of the Solar neighbourhood. Astron. Astrophys. 418, 989–1019. https://doi.org/10.1051/0004-6361:20035959.
Ogawa, M., 2007. Superplumes, plates, and mantle magmatism in two-dimensional numerical models. J. Geophys. Res. 112 https://doi.org/10.1029/2006JB004533 article B06404.
Parman, S.W., 2015. Time-lapse zirconography: Imaging punctuated continental evolution. Geochem. Perspect. Lett. 1, 43–52. https://doi.org/10.7185/geochemlet.1505.
Percival, D.B., Walden, A.T., 1993. Spectral Analysis for Physical Applications. Cambridge University Press, New York, NY.
Popper, K., 1963. Conjectures and Refutations: The Growth of Scientific Knowledge. Routledge & Kegan Paul, London.
Priestley, M.B., 1988. Non-linear and Non-stationary Time Series Analysis. Academic Press, London.
Prokoph, A., Puetz, S.J., 2015. Period-tripling and fractal features in multi-billion-year geological records. Math. Geosci. 47, 501–520. https://doi.org/10.1007/s11004-015-9593-y.
Prokoph, A., El Bilali, H., Ernst, R., 2013. Periodicities in the emplacement of large igneous provinces through the Phanerozoic: relations to ocean chemistry and marine biodiversity evolution. Geosci. Front. 4, 263–276. https://doi.org/10.1016/j.gsf.2012.08.001.
Puetz, S.J., Condie, K.C., 2019. Time series analysis of mantle cycles part I: periodicities and correlations among seven global isotopic databases. Geosci. Front. 10, 1305–1326. https://doi.org/10.1016/j.gsf.2019.04.002.
Puetz, S.J., Condie, K.C., 2021. Applying Popperian falsifiability to geodynamic hypotheses: Empirical testing of the episodic crustal/zircon production hypothesis and selective preservation hypothesis. Int. Geol. Rev. 63, 1920–1950. https://doi.org/10.1080/00206814.2020.1818143.
Puetz, S.J., Prokoph, A., Borchardt, G., Mason, E., 2014. Evidence of synchronous, decadal to billion-year cycles in geological, genetic, and astronomical events. Chaos, Solitons Fractals 62–63, 55–75. https://doi.org/10.1016/j.chaos.2014.04.001.
Puetz, S.J., Prokoph, A., Borchardt, G., 2016. Evaluating alternatives to the Milankovitch theory. J. Statist. Plann. Infer. 170, 158–165. https://doi.org/10.1016/j.jspi.2015.10.006.
Puetz, S.J., Condie, K.C., Pisarevsky, S., Davaille, A., Schwarz, C.J., Ganade, C.E., 2017. Quantifying the evolution of the continental and oceanic crust. Earth Sci. Rev. 164, 63–83. https://doi.org/10.1016/j.earscirev.2016.10.011.
Puetz, S.J., Ganade, C.E., Zimmermann, U., Borchardt, G., 2018. Statistical analyses of global U-Pb database 2017. Geosci. Front. 9, 121–145. https://doi.org/10.1016/j.gsf.2017.06.001.
Rampino, M.R., 2015. Disc dark matter in the Galaxy and potential cycles of extraterrestrial impacts, mass extinctions and geological events. Mon. Not. R. Astron. Soc. 448, 1816–1820. https://doi.org/10.1093/mnras/stu2708.
Rampino, M.R., 2018. Dark matter's shadowy effect on Earth. Astronomy. April 2018 issue. https://astronomy.com/magazine/2019/07/dark-matters–shadowy-effect–on-earth.
Rampino, M.R., Caldeira, K., 2015. Periodic impact cratering and extinction events over the last 260 million years. Mon. Not. R. Astron. Soc. 454, 3480–3484. https://doi.org/10.1093/mnras/stv2088.
Rampino, M.R., Caldeira, K., 2020. A 32-million year cycle detected in sea-level fluctuations over the last 545 Myr. Geosci. Front. 11, 2061–2065. https://doi.org/10.1016/j.gsf.2020.06.005.
Rampino, M.R., Caldeira, K., Zhu, Y., 2021. A pulse of the Earth: a 27.5-Myr underlying cycle in coordinated geological events over the last 260 Myr. Geosci. Front. 12, 101245 https://doi.org/10.1016/j.gsf.2021.101245.
Randall, L., Reece, M., 2014. Dark matter as a trigger for periodic comet impacts. Phys. Rev. Lett. 112, 161301 https://doi.org/10.1103/PhysRevLett.112.161301.
Richards, M.A., Alvarez, W., Self, S., Karlstrom, L., Renne, P.R., Manga, M., et al., 2015. Triggering of the largest Deccan eruptions by the Chicxulub impact. GSA Bull. 127, 1507–1520. https://doi.org/10.1130/B31167.1.

Roberts, N.M.W., Spencer, C.J., 2014. The zircon archive of continent formation through time. In: Roberts, N.M.W., van Kranendonk, M., Parman, S., Shirey, S., Clift, P.D. (Eds.), Continent Formation through Time. London, Special Publications, Geological Society.
Rolf, T., Coltice, N., Tackley, P.J., 2014. Statistical cyclicity of the supercontinent cycle. Geophys. Res. Lett. 41, 2351–2358. https://doi.org/10.1002/2014GL059595.
Rollinson, H., 2017. There were no large volumes of felsic continental crust in the early Earth. Geosphere 13, 235–246. https://doi.org/10.1130/GES01437.1.
Sanders, J.L., Das, P., 2018. Isochrone ages for ~3 million stars with the second Gaia data release. Mon. Not. R. Astron. Soc. 481, 4093–4110. https://doi.org/10.1093/mnras/sty2490.
Scargle, J.D., 1982. Studies in astronomical time series analysis. II-Statistical aspects of spectral analysis of unevenly spaced data. Astrophys. J. 263, 835–853. https://doi.org/10.1086/160554.
Scheel, H., Scholtes, S., 2000. Mathematical programs with complementarity constraints: stationarity, optimality, and sensitivity. Math. Oper. Res. 25, 1e22. https://doi.org/10.1287/moor.25.1.1.15213.
Schoene, B., Condon, D.J., Morgan, L., McLean, N., 2013. Precision and Accuracy in Geochronology. Elements 9, 19–24. https://doi.org/10.2113/gselements.9.1.19.
Schulz, M., Mudelsee, M., 2002. REDFIT: estimating red-noise spectra directly from unevenly spaced paleoclimatic time-series. Comput. Geosci. 28, 421e426. https://doi.org/10.1016/S0098-3004(01)00044-9.
Shackleton, N.J., King, H.T., Crowhurst, S.J., 1995. Evaluating the success of astronomical tuning: pitfalls of using coherence as a criterion for assessing pre-Pleistocene timescales. Paleoceanography 10, 693–697. https://doi.org/10.1029/95PA01454.
Shannon, C.E., 1949. Communication in the presence of noise. Proceed. Inst. Radio Eng. 37, 10–21. https://doi.org/10.1109/JRPROC.1949.232969.
Smye, A.J., Lavier, L.L., Zack, T., Stockli, D.F., 2019. Episodic heating of continental lower crust during extension: a thermal modeling investigation of the Ivrea-Verbano Zone. Earth Planet. Sci. Lett. 521, 158–168.
Stehman, S.V., Selkowitz, D.J., 2010. A spatially stratified, multi-stage cluster sampling design for assessing accuracy of the Alaska (USA) National Land Cover Database (NLCD). Int. J. Remote Sens. 31, 1877–1896. https://doi.org/10.1080/01431160902927945.
Stein, M., Hofmann, A.W., 1994. Mantle plumes and episodic crustal growth. Nature 372, 63–68. https://doi.org/10.1038/372063a0.
Steinhilber, F., Abreu, J.A., Beer, J., Brunner, I., Christl, M., Fischer, H., et al., 2012. 9,400 years of cosmic radiation and solar activity from ice cores and tree rings. Proc. Natl. Acad. Sci. 109, 5967–5971. https://doi.org/10.1073/pnas.1118965109.
Sternai, P., Caricchi, L., Pasquero, C., Garzanti, E., van Hinsbergen, D.J.J., Castelltort, S., 2020. Magmatic forcing of Cenozoic climate? J. Geophys. Res. Solid Earth 125. https://doi.org/10.1029/2018JB016460 e2018JB016460.
Stoica, P., Moses, R., 2005. Spectral Analysis of Signals. Prentice-Hall, Upper Saddle River, NJ.
Stothers, R.B., 1989. Volcanic eruptions and solar activity. J. Geophys. Res. 94, 17371–17381. https://doi.org/10.1029/JB094iB12p17371.
Strestik, J., 2003. Possible Correlation between Solar and Volcanic Activity in a Long-Term Scale. International Solar Cycle Studies (ISCS) Symposium, 23–28 June 2003. Tatranská Lomnica, Slovak Republic.
Tera, F., Papanastassiou, D.A., Wasserburg, G.J., 1973. A Lunar Cataclysm at ~3.95 AE and the Structure of the Lunar Crust. Abst. Fourth Lunar Sci. Conf. 4, 723–725.
Thompson, P.A., Burnett, A., 2012. Reproducible Research. CORE Issues in Professional and Research Ethics 1, paper 6. http://nationalethicscenter.org/content/article/175.
Tiwari, R.K., Rao, K.N.N., 1998. Correlated variations and periodicity of global CO2, biological mass extinctions and extra-terrestrial bolide impacts over the past 250 million years and possible geodynamical implications. Geofizika 15, 103–117. https://hrcak.srce.hr/ojs/index.php/geofizika/article/view/16060.
Turner, G., Cadogan, P.H., Yonge, C.J., 1973. Argon selenochronology. Proceed. Fourth Lunar Sci. Confer. 2, 1889–1914.
Vermeesch, P., 2018. IsoplotR: a free and open toolbox for geochronology. Geosci. Front. 9, 1479–1493. https://doi.org/10.1016/j.gsf.2018.04.001.
Vermeesch, P., 2020. On the treatment of discordant detrital zircon U–Pb data. Geochronology. https://doi.org/10.5194/gchron-2020-38 in-review.
Vieira, L.E.A., Solanki, S.K., Krivova, N., Usoskin, I., 2011. Evolution of the solar irradiance during the Holocene. Astron. Astrophys. 531, A6. https://doi.org/10.1051/0004-6361/201015843.
Voice, P.J., Kowalewski, M., Eriksson, K.A., 2011. Quantifying the timing and rate of crustal evolution: global compilation of radiometrically Dated Detrital Zircon grains. J. Geol. 119, 109–126. https://doi.org/10.1086/658295.
Walzer, U., Hendel, R., 2008. Mantle convection and evolution with growing continents. J. Geophys. Res. 113 https://doi.org/10.1029/2007jb005459 article B09405.
Walzer, U., Hendel, R., 2017. Continental crust formation: numerical modelling of chemical evolution and geological implications. Lithos 278-281, 215–228. https://doi.org/10.1016/j.lithos.2016.12.014.
Waters, J.M., Craw, D., 2006. Goodbye Gondwana? New Zealand biogeography, geology, and the problem of circularity. Syst. Biol. 55, 351–356. https://doi.org/10.1080/10635150600681659.
Wetherill, G.W., 1975. Late heavy bombardment of the moon and terrestrial planets. Proceed. Sixth Lunar Sci. Conf. 6, 1539–1561.
Wiemer, D., Schrank, C.E., Murphy, D.T., Wenham, L., Allen, C.M., 2018. Earth's oldest stable crust in the Pilbara Craton formed by cyclic gravitational overturns. Nat. Geosci. 11, 357–361. https://doi.org/10.1038/s41561-018-0105-9.
Young, G.M., 2018. Chapter 2 - Precambrian Glacial deposits: their Origin, Tectonic setting, and Key Role in Earth Evolution. In: Menzies, J., van der Meer, J.J.M. (Eds.), Past Glacial Environments, 2nd edition. Elsevier, pp. 17–45. https://doi.org/10.1016/B978-0-08-100524-8.00001-4.
Zachos, J., Pagani, M., Sloan, L., Thomas, E., Billups, K., 2001. Trends, rhythms, and aberrations in global climate 65 Ma to present. Science 292, 686–693. https://doi.org/10.1126/science.1059412.
Zimmermann, S., Mark, C., Chew, D., Voice, P.J., 2018. Maximising data and precision from detrital zircon U-Pb analysis by LA-ICPMS: the use of core-rim ages and the single analysis concordia age. Sediment. Geol. 375, 5–13. https://doi.org/10.1016/j.sedgeo.2017.12.020.